The Effects of Catalysts in Dolomite Growth at Low Temperature and the Structures of Nano-precipitates in Sedimentary Dolomite

By

Zhizhang Shen

A dissertation submitted in partial fulfillment of

the requirements for the degree of

Doctor of Philosophy

(Geoscience)

at the

UNIVERSITY OF WISCONSIN – MADISON

2015

Date of final oral examination: 4/24/2015

The dissertation is approved by the following members of the Final Oral Committee:
Huifang Xu, Professor, Geoscience
Izabela Szlufarska, Professor, Materials Science and Engineering
Philip E. Brown, Professor, Geoscience
Qiang Cui, Professor, Chemistry
Stephen R. Meyers, Associate Professor, Geoscience
John A. Luczaj, Associate Professor, Geoscience, University of Wisconsin-Green Bay

Abstract

Laboratory syntheses of dolomite at low temperatures cannot be successful without catalysts. The rate-limiting step in the dolomite growth is most likely to be the dehydration of water from surface Mg^{2+}. We have applied the methods of molecular dynamics simulations (MD) and density functional theory (DFT) simulations to study the effects of catalysts in the sedimentary dolomite formation.

There are two hypotheses regarding the role of catalysts in the dehydration of surface magnesium. One hypothesis is that catalysts can be strongly adsorbed onto crystal surfaces replacing surface water and forming a hydrophobic layer. To test this hypothesis *ab initio* simulations based on density functional theory (DFT) were carried out to study the thermodynamics of competitive adsorption of hydrogen sulfide and water on dolomite (104) surfaces from solution. We find that water is thermodynamically more stable on the surface than hydrogen sulfide with the difference in adsorption energy of -13.6 kJ/mol (in vacuum) and -12.8 kJ/mol (in aqueous solution). However, aqueous hydrogen sulfide adsorbed on the surface increases the Mg^{2+}-H_2O distances on surrounding surface sites. One possibility for H_2S facilitating the carbonation is that there is room for direct interaction between Mg^{2+} and CO_3^{2-} due to the geometry and the large size of H_2S and larger space between H_2O/H_2S and dolomite surface.

Another hypothesis for the role of catalysts is that catalysts can lower the dehydration barrier of surface Mg^{2+} so that carbonate anions can approach and be adsorbed onto the surface. Free energy (potential of mean force, PMF) calculations have been performed for water molecules leaving the first two hydration layers above the dolomite (104) surface in the following three conditions: without catalyst, with

monosaccharide (mannose) and with oligosaccharide (three units of mannose). We fitted the force field for the interactions between –OH groups of sugar and surface cations of dolomite. The simulations have shown that there is no obvious effect of monosaccharide in lowering the dehydration barrier for surface Mg. However, a bridge shaped configuration of oligosaccharide lying relatively flat on the surface is able to decrease the dehydration barrier about 0.7~1.1 kcal/mol. This decrease is caused by the hydrophobic – CH groups of polysaccharides and is the possible major effect of polysaccharide on the dolomite growth at low temperatures.

The fine-scale cation ordering and metastable Ca-Mg carbonates indicate the diagenetic processes of sedimentary dolomites from disordered metastable sediments to more stable hard rocks. Therefore, in order to determine the real structures of the nano-precipitates in natural sedimentary dolomite, we also studied "*c*" and "*d*" superstructures by using (scanning) transmission electron microscopy (STEM). STEM images of Wisconsin Ordovician dolomite show that the "*c*"-reflections could be the result of multiple diffractions between the host dolomite and twinned Mg-calcite nano-lamellae under TEM imaging and diffraction modes. Z-contrast images of Proterozoic dolomite demonstrated that the "*d*" superstructure has a cation ordering sequence of Ca-Ca-Mg-Ca-Ca-Mg along the ***c*** direction resulting in a chemical composition of $Ca_{0.67}Mg_{0.33}CO_3$.

Acknowledgment

First of all, I would like to express my deepest gratitude to my two advisors, Professor Huifang Xu and Professor Izabela A. Szlufarska, for their support, patience and guidance throughout my Ph.D. work. Professor Xu's enthusiasm in science and proactive ideas inspired and lead me for the past nearly six years. And without Professor Szlufarska's expertise and encouragement, I would not be able to finish my dissertation.

I would also like to thank my other committee members: Professor Philip E. Brown, from Geoscience department, who has been serving in my committee from the beginning and helped me numerous times with the scientific writings; Professor Qiang Cui, from Chemistry department, who gave me precious and insightful suggestions about the simulation work; Professor John Luczaj, from Geoscience department at University of Wisconsin-Green Bay, who carefully reviewed my dissertation and gave me helpful comments about the dolomite problem; and Professor Steven Meyers, from Geoscience department, who kindly serve as my committee.

In addition, I would like to thank Professor Hiromi Konishi, now at Niigata University in Japan, for his help with the TEM work. I also would like to thank Professor Dane Morgan, from Department of Materials Science and Engineering, for his discussion and suggestions about thermodynamics and simulations part of my thesis.

Many thanks to my friends in nanogeoscience group and the computational materials group at University of Wisconsin-Madison. Finally, I would like to offer my gratitude from the bottom of my heart to my parents for their enduring love and support.

Table of contents

Chapter 1. Introduction and motivation

1.1 Dolomite structure, and sedimentary dolomite

The term dolomite can be referred to as a mineral and a rock. The dolomite mineral is a carbonate with a chemical composition of $CaMg(CO_3)_2$ and a structure of $R\bar{3}$. The dolomite rock or dolostone is a carbonate rock whose composition is dominated by dolomite minerals. The studies presented in this thesis are focused on a number of topics related to the dolomite mineral, so the dolomite term used in this dissertation only refers to the dolomite mineral. However, the dolomite rock is an economically important rock: the dolomite rock accounts for 50% of the world's carbonate reservoirs and ~80% of oil and gas reservoirs in North America (Zengler et al. 1980), and serves as the host rock for Mississippi Valley Type (MVT) ore deposits of lead, zinc, copper and other base metals.

The structure of an ordered dolomite crystal ($R\bar{3}$) is similar to that of a calcite ($R\bar{3}c$) but with Ca and Mg layers alternating along the *c*-axis (Figure 1.1.1). The large difference in size between the Ca^{2+} and Mg^{2+} ions (33%) results in the cation ordering along the *c*-axis. With the nonequivalence of Ca and Mg layers, the symmetry is reduced from $R\bar{3}c$ to $R\bar{3}$. Since the internal symmetry and chemistry of dolomite and calcite are quite similar, the overall crystal shape and physical properties are also very similar. The following features in hand specimen can be used to distinguish the two minerals: dolomite is slightly denser (D 2.86); calcite will get a pale blue stain when boiled with copper nitrate; dolomite does not effervesce as strongly as calcite when reacting with cold dilute acid. The disordered dolomite has the same symmetry as calcite. Thus the super-lattice reflections such as (015), (101), and (021) are absent in disordered dolomite but they are present in ordered dolomites. In practice, the ratio I_{015}/I_{006} in x-ray diffraction

(XRD) pattern has been used as a rough indicator of ordering state (Antao et al. 2004; Luth 2004).

Many natural dolomites have an excess of Ca^{2+}, with composition up to ~ $Ca_{1.2}Mg_{0.8}(CO_3)_2$ which is quite different from the stoichiometric dolomite $CaMg(CO_3)_2$ (Reeder 1983, 1992; Warren 2000). The additional Ca in the dolomite structure causes an increase in the unit cell parameter and hence in *d*-spacings, since the radius of Ca^{2+} is larger than that of Mg^{2+} (the ionic radii for Ca^{2+} and Mg^{2+} in 6-fold coordinated are 1.00Å and 0.72Å, respectively (Shannon et al. 1976)). Therefore, the d_{104} values measured in XRD are often used to determine the composition of dolomite. There are two curves of d_{104} values versus $MgCO_3$ content in dolomite; one is for the disordered dolomite, the other one for the ordered dolomite (Goldsmith and Graf 1958; Goldsmith et al. 1961; Zhang et al. 2010). In Ca-rich dolomite, heterogeneous microstructures such as modulations and ordered superstructures have been reported (Reeder 1992). The common morphology of saddle dolomite (Figure 1.1.2) is also related to the excess calcium in the dolomite, which is present in the form of thin, coherent laths of calcite (Barber et al. 1985). Because the lattice spacing in calcite is larger than that in dolomite, these calcite laths cause local distortion of host dolomite. In addition, other metal ions (with Fe and Mn being the most common ones) can occupy the cation sites that are often Mg^{2+} sites. This substitution usually gives dolomite a yellow or brown color (Deer et al. 1992).

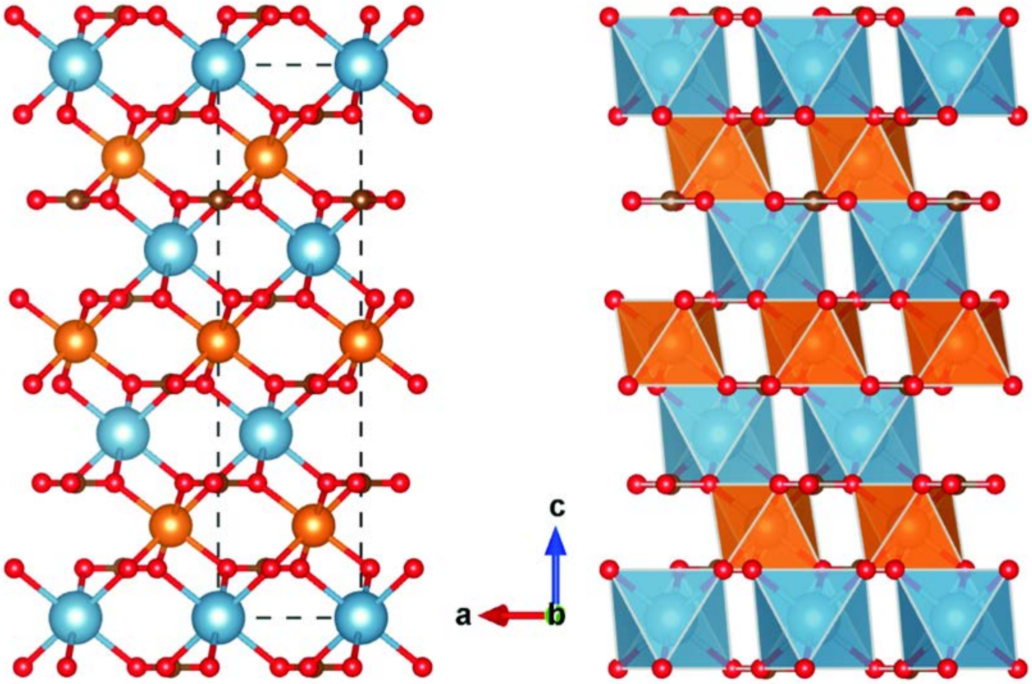

Figure 1.1.1 The ball-stick (left) and polyhedral (right) models of dolomite. Blue: Ca, Orange: Mg, Brown: C, Red: O.

Figure 1.1.2 Saddle dolomite with curved crystal faces is very common in natural dolomite. This sample is from the mineralogy lab collection at UW-Madison (#6229, location: near Baxter Springs, Kansas)

1.2 “Dolomite Problem”

Dolomite, used to be ubiquitous in the geological past, is yet rarely found in Holocene sediments (Warren 2000). Its rare occurrence in the modern sediments defies the geological notion that the present is the key to the past. This contradiction is at the heart of the famous “dolomite problem”, which has been bewildering geologists for many decades. To solve the dolomite problem, it is essential to understand the mechanism of dolomite formation.

Although in general dolomite can have replacement or primary origin, most of the sedimentary dolomites in the geological record are believed to be replacement product of calcite, high magnesian calcite or aragonite precursors through a dissolution-precipitation reaction of the following form:

$2CaCO_3 + Mg^{2+} \rightarrow CaMg(CO_3)_2 + Ca^{2+}$.

It has been shown that the high Mg/Ca ratio achieved through the evaporation of seawater in sediments makes seawater capable of dolomitizing limestone (Hsu 1967). However, this is not happening in the modern seafloor. The chemical reaction for this dissolution-precipitation process has also been proposed in literature (Lippmann and Lippmann 1973):

$CaCO_3 + Mg^{2+} + CO_3^{2-} \rightarrow CaMg(CO_3)_2$.

Different models attempting to explain the source of Mg^{2+} ions (or high Mg/Ca ratio) and hydrological settings for dolomitization have been proposed and reviewed (Adams and Rhodes 1960; Hanshaw et al. 1971; Hsü and Schneider 1973; Zengler et al. 1980; Machel and Mountjoy 1986; Gawthorpe 1987; Hardie 1987; Warren 2000; Tucker and Wright 2009; Li et al., 2013). A brine reflux model is one of the most plausible mechanisms. This model was first proposed by Adams and Rhodes (1960) to explain the extensive dolomitization of the Permian reef complex of west Texas. The dense and hot, highly alkaline Mg^{2+}-rich hypersaline brines descend, replacing marine pore water, and "seep slowly downward through the slightly permeable carbonates at the lagoon floor" (Adams and Rhodes 1960). A model of groundwater and seawater mixing was also proposed for dolomitization based on studies of Wisconsin dolomite to lower dissolved salts concentrations (Badiozamnai 1973). Although the models point out some important conditions for dolomitization, they cannot completely decipher the dolomite problem (Hardie, 1987; Luczaj, 2006).

In contrast to the massive ancient platform dolomite, Holocene dolomite can only form thin layers of precipitates (usually less than 2m) in evaporitic tidal flats (sabkhas), dry coastal plain (Coorong dolomite), or hypersaline continental lacustrine environment. These dolomites are believed to be syndepositional and primary precipitates (Miser et al. 1987; Last 1990; Warren 2000). Previous thermodynamic calculations have shown that the modern seawater is supersaturated with respect to dolomite by one to two orders of magnitude (Hardie 1987). However, the massive formation of dolomite is not happening and the occurrence of dolomite is limited to some specific environments mentioned above. In laboratory, the attempts to synthesize dolomite abiotically under conditions close to those observed in modern dolomite environments have been unsuccessful (Land 1998). It is now realized that the dolomite problem lies in the kinetic barriers at low temperature that hinder the growth of dolomite. Lippmann (1973, 1982) proposed that the strong hydration bond between Mg^{2+} ions and water makes carbonate ions difficult to bond with hydrated Mg^{2+} ions.

Based on the fact that modern dolomite formations are usually associated with sediments where anaerobic microorganisms such as sulfate reducing bacteria (SRB) and methanogens are active (Hardie 1987; Vasconcelos and McKenzie 1997; Warren 2000; Roberts et al. 2004; Wright and Wacey 2005; Kenward et al. 2009), microorganisms were proposed to help overcome the kinetic barriers, although the detailed mechanism is unclear. Successful syntheses of Ca-rich dolomite at low temperatures with anaerobic bacteria have been reported (Vasconcelos and McKenzie 1997; Roberts et al. 2004; Kenward et al. 2009). Some recent works have also shown that aerobic bacteria can mediate the formation of dolomite (Sánchez-Román et al. 2008, 2009, 2011; Deng et al., 2010). However, the reported dolomite precipitates at low temperature are questionable (Zhang et al. 2012; Gregg et al. 2015). Aragonite, hydromagnesite, and Ca-Mg-phosphates were identified as “ordered dolomite” in the previous publications. Some abiotic materials that are similar to microbial metabolites, exudates or other cellular components (such as H_2S, methane, polysaccharides and ethanol) have also been shown to promote the precipitation of low temperature dolomite (Zhang et al. 2012a; Zhang et al. 2012b; Zhang et al. 2012c). The amount of $MgCO_3$ in the precipitating Ca-Mg carbonate also increases as concentration of the catalysts increases (Zhang et al. 2012a; Zhang et al. 2012b). Further work to uncover the mysteries of the roles of catalysts can help us predict the species of catalysts and hence dolomite forming environments, and better understand the dolomite formation processes.

Although all the progress is made in the understanding of the formation of the modern or primary dolomite, Burns et al. (2000) proposed the active role of microbes in massive dolomitization by examining the dolomite historical distribution and the chemical and biogeochemical variations in seawater. The authors found that there is a rough correlation between high dolomite abundance in total carbonate rock and decreased oxygen levels in the atmosphere and oceans, and the low oxygen level favors a more active community of anaerobic microbes. Therefore, our theoretical study of the catalysis of primary dolomite or synthesized dolomite can serve as the first step to the exploration of catalyzed massive dolomitization and shed light on deciphering the dolomite problem.

1.3 Diagenesis and superstructures in sedimentary dolomite

As mentioned in section 1.1, the natural sedimentary dolomite is usually calcium-rich. Due to the low temperatures and sluggish kinetics, the extra Ca atoms, initially incorporated into the crystal, form metastable phases at microscopic level during diagenetic processes. Wenk et al. (1990) summarized all the proposed superstructures (Figure 1.3.1) in Ca-Mg carbonate and named them in greek letters: α (calcite), β (dolomite), γ, ν, μ, and δ. They also predicted that α, γ and δ could exist as small domains in the matrix of dolomite (β) and ν and μ as domains in calcite (α). This prediction is supported by the common occurrence of “c” super-reflections and much less common “d” super-reflections in natural dolomites as shown in extensive TEM work on the dolomite microstructures (Reeder and Wenk 1979; Reeder 1981; Wenk and Zenger 1983; Van Tendeloo et al. 1985; Wenk and Zhang 1985; Reksten 1990; Wenk et al. 1991). In these previous works, the superstructures γ and δ are used to interpret the “c” and “d” reflections.

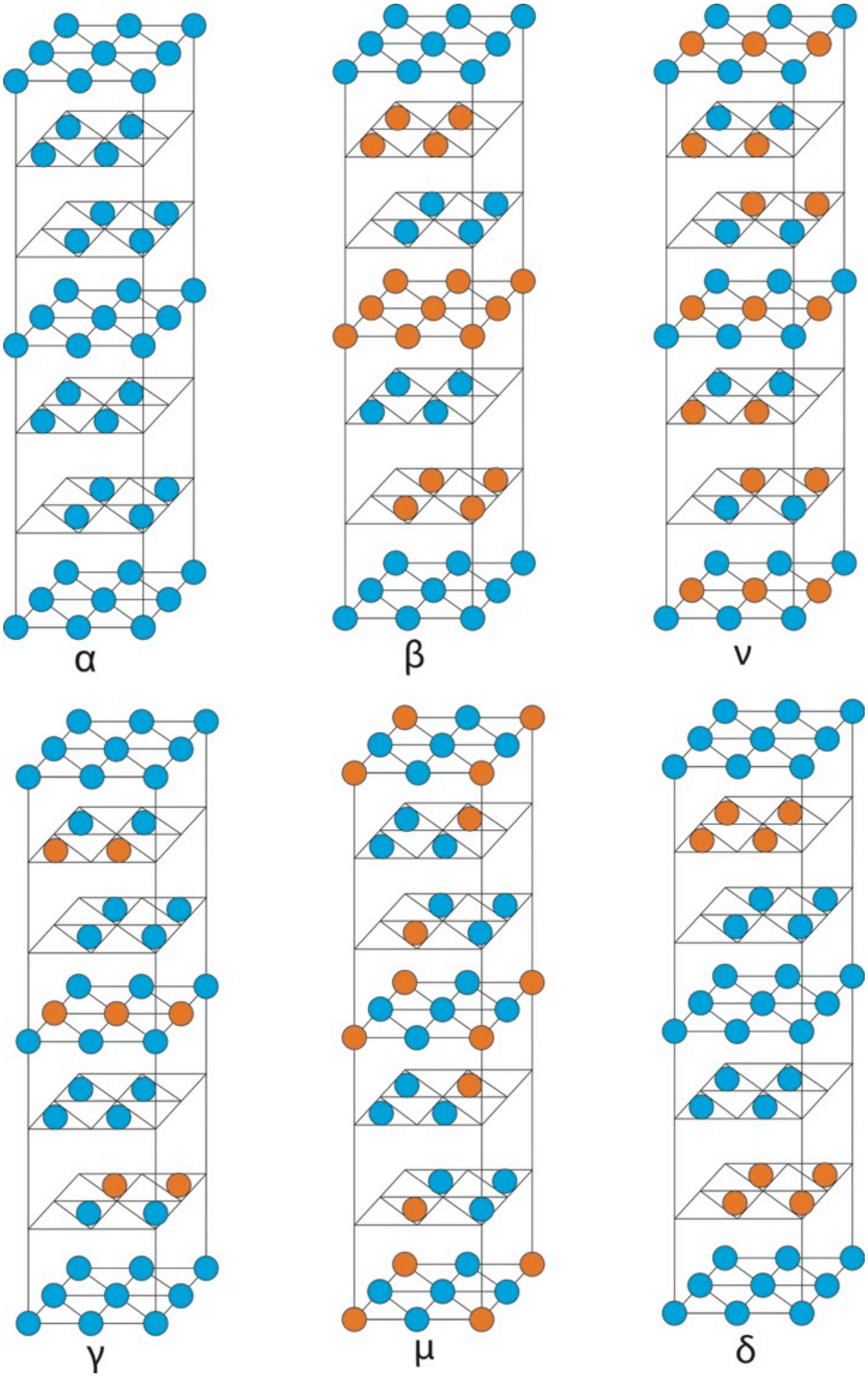

Figure 1.3.1 Proposed models for cation ordering in Ca-Mg carbonates. The ***a*** dimension of the hexagonal cells have been doubled compared to the conventional calcite or dolomite unit cell. The blue circles represent Ca atoms and the orange Mg. Reproduced from Wenk et al., 1991.

1.4 Overview of the thesis

Transformation from the dolomite-forming fluids to the hard rock of dolomite includes two major steps: growth and digenesis. We studied the effects of catalysts in the dolomite growth by employing methods of atomic simulations. The superstructures in natural sedimentary dolomite formed during digenesis were examined by the transmission electron microscope with an atomic resolution.

The scanning transmission electron microscopy (STEM) with a spherical aberration corrector is key to our clear interpretation of dolomite microstructures and nano-precipitates. The theory of STEM imaging is covered in chapter 2. The “c” reflection has shown to be an overlap of twinned between dolomite and high-magnesian calcite and is reported in chapter 3. The “d” reflections are corresponding to a superstructure with Ca-Ca-Mg-Ca-Ca-Mg ordering sequence, and is different from the previous models. This result of “d” reflections is detailed in chapter 4.

Two mechanisms were proposed for the catalyst effects on the dehydration of Mg-H_2O complex, which is considered to be the key kinetic barrier in the dolomite formation: 1) the catalysts can be strongly adsorbed on the surface forming a hydrophobic layer, and thus repel the water from the surface Mg^{2+}; 2) the catalysts adsorbed on the dolomite surface can lower the dehydration energy barrier. In order to test the second hypothesis, *ab initio* simulations based on the density functional theory (DFT) were carried out to study the thermodynamics of competitive adsorption of hydrogen sulfide and water on dolomite (104) surfaces from solution. The theories of DFT are introduced in chapter 5. The results from these calculations are presented in chapter 6. Our work indicates that adsorbed hydrogen sulfide can increase the bond distance between water molecule and surface Mg that are neighboring to the hydrogen sulfide.

In chapter 7, we report the calculations of the free energy (potential of mean force, PMF) of dehydration of surface Mg^{2+} for systems with and without carbohydrates (mannose and tri-mannose), which is another eligible catalyst. Since DFT calculations of pontential of mean force are computationally expensive, we use MD simulations with classical force fields in this study. The basics of MD simulations and the PMF calculations are also explained in chapter 6. The results show that a bridge shaped configuration of oligosaccharide (tri-mannose) lying relatively flat on the surface is able to decrease the dehydration barrier for surface Mg^{2+}.

All specimens referenced in this thesis are in the collections of the Department of Geoscience, University of Wisconsin-Madison, under file number UW2025.

References

Adams, J.E., and Rhodes, M.L. (1960) Dolomitization by Seepage Refluxion. American Association of Petroleum Geology Bulletin, 44, 1912–1920.

Antao, S.M., Mulder, W.H., Hassan, I., Crichton, W.A., and Parise, J.B. (2004) Cation disorder in dolomite, CaMg(CO3)2, and its influence on the aragonite + magnesite <--> dolomite reaction boundary. American Mineralogist, 89, 1142–1147.

Badiozamnai, K. (1973) The dorag dolomitization model - application to the middle Ordovician of Wisconsin. Journal of Sedimentary Research, 43, 965–984.

Barber, D.., Reeder, R.., and Smith, D.. (1985) A tem microstructural study of dolomite with curved faces (saddle dolomite). Contributions to Mineralogy and Petrology, 91, 82–92.

Burns, S.J., Mckenzie, J. a., and Vasconcelos, C. (2000) Dolomite formation and biogeochemical cycles in the Phanerozoic. Sedimentology, 47, 49–61.

Deer, W.A., Howie, R.A., and Zussman, J. (1992) An introduction to the rock-forming minerals Vol. 2. Longman Scientific & Technical Hong Kong.

Gawthorpe, R.L. (1987) Burial dolomitization and porosity development in a mixed carbonate-clastic sequence: an example from the Bowland Basin, northern England. Sedimentology, 34, 533–558.

Goldsmith, J.R., and Graf, D.L. (1958) Relation between lattice constants and composition of the Ca-Mg carbonates. American Mineralogist, 43, 84–101.

Goldsmith, J.R., Graf, D.L., and Heard, H.C. (1961) Lattice constants of the calcium-magnesium carbonates. American Mineralogist, 46, 453–457.

Gregg, J.M., Bish, D.L., Kaczmarek, S.E., and Machel, H.G. (2015) Mineralogy, nucleation and growth of dolomite in the laboratory and sedimentary environment: A review. Sedimentology.

Hanshaw, B.B., Back, W., and Deike, R.G. (1971) A geochemical hypothesis for dolomitization by ground water. Economic Geology, 66, 710–724.

Hardie, L.A. (1987) Dolomitization; a critical view of some current views. Journal of Sedimentary Research, 57, 166–183.

Hsu, K.J. (1967) Chemistry of Dolomite Formation. Developments in Sedimentology, 9, 169–191.

Hsü, K.J., and Schneider, J. (1973) Progress report on dolomitization—hydrology of Abu Dhabi sabkhas, Arabian Gulf. In The Persian Gulf pp. 409–422. Springer.

Kenward, P. a, Goldstein, R.H., González, L. a, and Roberts, J. a (2009) Precipitation of low-temperature dolomite from an anaerobic microbial consortium: the role of methanogenic Archaea. Geobiology, 7, 556–65.

Land, L.S. (1998) Failure to Precipitate Dolomite at 25° C from Dilute Solution Despite 1000-Fold Oversaturation after32 Years. Aquatic Geochemistry, 4, 361–368.

Last, W.M. (1990) Lacustrine dolomite—an overview of modern, Holocene, and Pleistocene occurrences. Earth-Science Reviews, 27, 221–263.

Li, Z., Goldstein, R. H., and Franseen, E. K. (2013) Ascending freshwater-mesohaline mixing: A new scenario for dolomization. Journal of sedimentary research, 83, 277-283.

Lippmann, F., and Lippmann, F. (1973) Sedimentary carbonate minerals Vol. 228. Springer.

Luczaj, J.A. (2006) Evidence against the Dorag (mixing-zone) model for dolomitization along the Wisconsin arch - A case for hydrothemal diagnesis. AAPG bulletin, 90, 1719-1738

Luth, R.W. (2004) Experimental determination of the reaction aragonite + magnesite = dolomite at 5 to 9 GPa. Contributions to Mineralogy and Petrology, 141, 222–232.

Machel, H.-G., and Mountjoy, E.W. (1986) Chemistry and Environments of Dolomitization —A Reappraisal. Earth-Science Reviews, 23, 175–222.

Miser, D.., Swinnea, J.., and Steinfink, H. (1987) Tem observations and x-ray structure refinement of a twinned dolomite microstructure. American Mineralogist, 72, 188–193.

Reeder, R.J. (1981) Contributions to Mineralogy and Electron Optical Investigation of Sedimentary Dolomites, 148–157.

——— (1983) Crystal chemistry of the rhombohedral carbonates. Reviews in Mineralogy and Geochemistry, 11, 1–47.

——— (1992) Carbonates; growth and alteration microstructures. Reviews in Mineralogy and Geochemistry, 27, 380–424.

Reeder, R.J., and Wenk, H.R. (1979) Microstructures in low temperature dolomites. Geophysical Research Letters, 6, 77–80.

Reksten, K. (1990) Modulated microstructures in calcian ankerite. American Mineralogist, 75, 495–500.

Roberts, J. a., Bennett, P.C., González, L. a., Macpherson, G.L., and Milliken, K.L. (2004) Microbial precipitation of dolomite in methanogenic groundwater. Geology, 32, 277–280.

Sánchez-Román, M., Vasconcelos, C., Schmid, T., Dittrich, M., McKenzie, J.A., Zenobi, R., and Rivadeneyra, M.A. (2008) Aerobic microbial dolomite at the nanometer scale: Implications for the geologic record. Geology, 36, 879–882.

Sánchez-Román, M., McKenzie, J.A., de Luca Rebello Wagener, A., Rivadeneyra, M.A., and Vasconcelos, C. (2009) Presence of sulfate does not inhibit low-temperature dolomite precipitation. Earth and Planetary Science Letters, 285, 131–139.

Sánchez-Román, M., Romanek, C.S., Fernández-Remolar, D.C., Sánchez-Navas, A., McKenzie, J.A., Pibernat, R.A., and Vasconcelos, C. (2011) Aerobic biomineralization of Mg-rich carbonates: Implications for natural environments. Chemical Geology, 281, 143–150.

Shannon, B.Y.R.D., H, M., Baur, N.H., Gibbs, O.H., Eu, M., and Cu, V. (1976) Revised Effective Ionic Radii and Systematic Studies of Interatomie Distances in Halides and Chaleogenides Central Research and Development Department , Experimental

Station , E . L Du Pont de Nemours The effective ionic radii of Shannon & Prewitt [Acta .

Tucker, M.E., and Wright, V.P. (2009) Carbonate sedimentology. John Wiley & Sons.

Van Tendeloo, G., Wenk, H.R., and Gronsky, R. (1985) Modulated structures in calcian dolomite: A study by electron microscopy. Physics and Chemistry of Minerals, 12, 333–341.

Vasconcelos, C., and McKenzie, J. (1997) Microbial mediation of modern dolomite precipitation and diagenesis under anoxic conditions (Lagoa Vermelha, Rio de Janeiro, Brazil). Journal of Sedimentary Research, 67, 378–390.

Warren, J. (2000) Dolomite: occurrence, evolution and economically important associations. Earth-Science Reviews, 52, 1–81.

Wenk, H.-R., and Zhang, F. (1985) Coherent transformations in calcian dolomites. Geology, 13, 457–460.

Wenk, H.-R., Meisheng, H., Lindsey, T., and Morris Jr, J.W. (1991) Superstructures in ankerite and calcite. Physics and Chemistry of Minerals, 17, 527–539.

Wenk, H.R., and Zenger, D.H. (1983) Sequential basal faults in Devonian dolomite, Nopah Range, Death Valley area, California. Science, 222, 502–504.

Wright, D.T., and Wacey, D. (2005) Precipitation of dolomite using sulphate-reducing bacteria from the Coorong Region, South Australia: significance and implications. Sedimentology, 52, 987–1008.

Zengler, D.H., Dunham, J.D., and Ethington, R.L. (1980) Concepts and models of dolomitization.

Zhang, F., Xu, H., Konishi, H., and Roden, E.E. (2010) A relationship between d104 value and composition in the calcite-disordered dolomite solid-solution series. American Mineralogist, 95, 1650–1656.

Zhang, F., Xu, H., Konishi, H., Kemp, J.M., Roden, E.E., and Shen, Z. (2012) Dissolved sulfide-catalyzed precipitation of disordered dolomite: Implications for the formation mechanism of sedimentary dolomite. Geochimica et Cosmochimica Acta, 97, 148–165.

Zhang, F., Yan, C., and Teng, H.H. (2012) In situ AFM observations of Ca–Mg carbonate crystallization catalyzed by dissolved sulfide: Implications for sedimentary dolomite formation. Geochimica et Cosmochimica Acta, 105, 44–55.

Zhang, F., Xu, H., Konishi, H., Shelobolina, E.S., and Roden, E.E. (2012) Polysaccharide-catalyzed nucleation and growth of disordered dolomite: A potential precursor of sedimentary dolomite. American Mineralogist, 97, 556–567.

Chapter 2. Z-contrast Imaging

In most textbooks of transmission electron microscopy (TEM), the main part of contents covers the image forming theory, contrasts, and data interpretation of the conventional transmission electron microscopy (CTEM), while the theory of scanning transmission electron microscopy (STEM) is usually not elaborated. The understanding of the STEM has been developed gradually over the past decade or two (Pennycook, 2002; Nellist, 2007; and Pennycook and Nellist, 2011). And because most of our results were obtained from STEM, this chapter will be focused on the components and coherent imaging theory of STEM. The similarities and differences between STEM and CTEM will be pointed out when it is necessary.

2.1 High-Resolution Transmission Electron Microscopy

The main components of a conventional transmission electron microscope are: the electron gun, the illumination system, the image forming system, the image magnification and projection system, and the detector system. A diffraction pattern forms at the back focal plane of the objective lens that is just below the thin specimen (Figure 2.1.1). High-resolution transmission electron imaging uses multi-beams (i.e., the contrast comes from the interference between diffracted beams and the direct beam) (Williams, D.B. and Carter, C.B., 1996; Leng, 2008). The change of experimental conditions, such as defocus, specimen thickness, spherical aberrations of the object lens, etc., can affect and even reverse the contrast in HRTEM images, and make the HRTEM images not directly interpretable. Thus, the TEM image simulations are usually needed to aid the correct interpretation of microstructures. Dynamical diffraction is another complexity in HRTEM imaging (Pennycook, 2002) and can cause incorrect structure interpretation as shown in chapter 3.

2.2 Scanning Transmission Electron Microscopy

2.2.1 Components of STEM

Geometrically, the STEM can be regarded as an inverted conventional TEM (Figure 2.1.1). Accelerated electrons from field emission gun are focused to form an atomic-scale probe at the thin sample by condenser lenses and an objective lens. An objective aperture is used to restrict the angle of the beams that contribute to form the images. Scan foils are used to scan the probe over the sample in a raster. In the end, different detectors sample different parts of the scattering space. The bright field (BF) detector usually collects over a small disc of low-angle coherently scattered electrons centered on the optic axis of the microscope, whereas the high-angle annular dark field (HAADF) detector collects over an annulus of high-angle incoherently scattered electrons (Kirkland, 1998; and Nellist, 2007). The BF STEM images are similar to the HRTEM images because of the principle of reciprocity. An atomic resolution HADDF image is also called a Z-contrast image, which provides direct chemical information for the material. The Z-contrast imaging technique can avoid multiple diffractions that commonly occur in HRTEM and electron diffraction modes. The BF image is expected to contain diffraction and strain contrast that is less evident in the HAADF image. The transmitted electrons that are in-elastically scattered are used for electron energy loss spectroscopy (EELS).

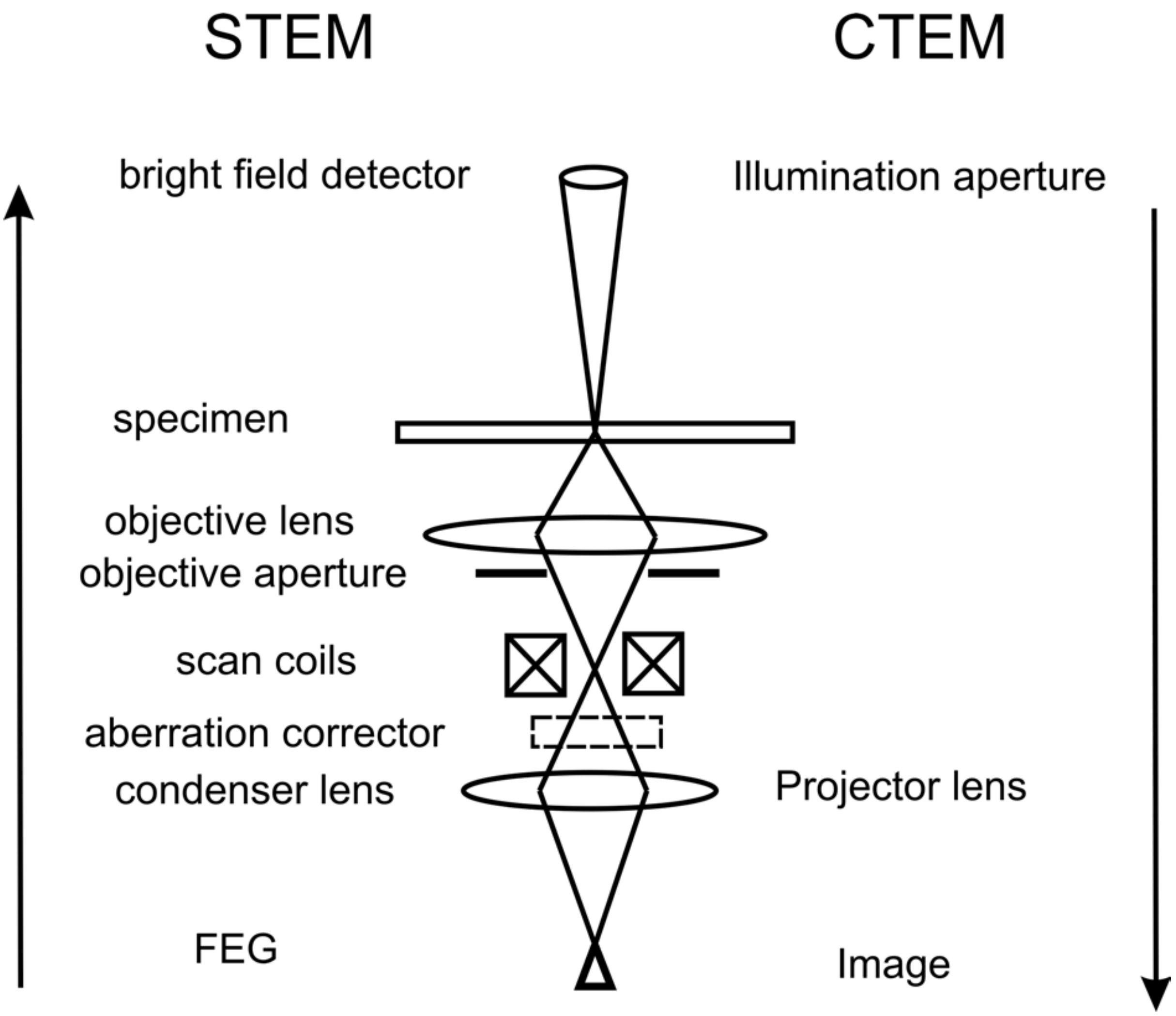

Figure 2.1.1 A schematic diagram showing the conventional transmission electron microscope (CTEM) and scanning transmission electron microscope (STEM) (modified after Nellist, 2011). Geometrically, the STEM is CTEM upside-down.

2.2.2 High-angle Annular Dark-field Imaging

The intensity of incoherent imaging can be expressed as the convolution of a real-positive intensity of the point-spread function and an object function.

$$I_{incoh}(\mathbf{R}) = |P(\mathbf{R})|^2 * O(\mathbf{R}) \qquad (2.2.1)$$

But why is DF STEM imaging incoherent? Here, we just consider a simple case of a thin sample to demonstrate the STEM imaging, more details about the influence of the dynamical diffraction, sample thickness and thermal diffusion scattering are shown in Nellist (2011). In STEM, the point-spread function can be written as

$$P(\mathbf{R}-\mathbf{R_0}) = \int T(\mathbf{K}) \exp(i2\pi\mathbf{K}\cdot\mathbf{R})\exp(-i2\pi\mathbf{K}\cdot\mathbf{R_0})d\mathbf{K} \qquad (2.2.2)$$

where **K** is the transverse component of a partial plane wave that is focused by objective lens to form the coherent probe (Figure 2.2.1), $\mathbf{R_0}$ is the probe position, and $T(\mathbf{K})$ is the lens transmission function. The lens transmission function is given by

$$T(\mathbf{K}) = A(\mathbf{K}) \exp[-i\chi(\mathbf{K})], \qquad (2.2.3)$$

where $A(\mathbf{K})$ is a top-hat aperture function (1 inside objective aperture and 0 outside) and $\chi(\mathbf{K})$ is a phase shift caused by the lens aberrations (the two major contributors are defocus and spherical aberration).

The initial partial wave **K** is diffracted by a thin sample with a transmission function ϕ to form a final plane wave $\mathbf{K_f}$ (Figure 2.2.1). The intensity measured in the detector plane can be expressed as the modulus square of the exiting wave function. The wave exiting the sample at the detector plane can expressed as

$$\Psi(\mathbf{K_f},\mathbf{R_0}) = \int T(\mathbf{K}) \exp(i2\pi\boldsymbol{K}\cdot\boldsymbol{R_0})\, \phi(\mathbf{K_f}-\mathbf{K})\, d\mathbf{K} \qquad (2.2.4)$$

The intensity integrated over the high-angle annular dark-field detector can be written as

$$I(\mathbf{Q}) = \iint D_{ADF}(\mathbf{K_f})T(\mathbf{K})T^*(\mathbf{K}+\mathbf{Q})\, \phi(\mathbf{K_f}-\mathbf{K})\, \phi^*(\mathbf{K_f}-\mathbf{K}-\mathbf{Q})\, d\mathbf{K_f}d\mathbf{K}, \qquad (2.2.5)$$

where **Q** is the image spatial frequency, separation between pairs of incident partial plane waves and D_{ADF} is the detector function.

Because the size (“fatness”) of the HAADF detector is much larger than the objective aperture, the two integrals of $\mathbf{K_f}$ and **K** can be separated. Then, the equation 2.2.5 becomes

$$I(\mathbf{Q}) = \int T(\mathbf{K})T^*(\mathbf{K}+\mathbf{Q})d\mathbf{K} \ \times \int D_{ADF}(\mathbf{K_f})\phi(\mathbf{K_f}-\mathbf{K})\ \phi^*(\mathbf{K_f}-\mathbf{K}-\mathbf{Q})d\mathbf{K_f} \qquad (2.2.6)$$

The Fourier transform of equation 2.2.6 is equivalent to the equation 2.2.1. At high angle scattering events, the intensity is strongly related to atomic number (Z) through the ~Z^n dependence of the Rutherford scattering cross-section. The object function can also be written as

$$O(\mathbf{R}) = \sum_{i=1}^{N} Z^n \delta(\mathbf{R}-\mathbf{R_0}) \qquad (2.2.7)$$

where n is dependent on experimental condition (e.g., for Camera length =160 mm that was used in our experiments, n= 2.27 according to Shi (2013)).

As mentioned above, thanks to the large geometry of ADF detector, the dark-field STEM imaging is of incoherent nature. In order to acquire good contrast, a high angle annular detector or a detector with a large inner radius is needed. In order to form a small and localized probe and then to get a sub-Å resolution in images, the minimization of the spherical aberrations caused by the objective lens is an essential issue. Z-contrast images can reveal vacancies and occupancies of metals in complicated minerals very well (Xu et al. 2014a, 2014b).

2.2.3 Sample Preparation and Experimental Conditions

Specimens for STEM measurements were prepared by ion milling. Ion milling was performed with a Fischione 1010 ion mill operated at an acceleration voltage of 4 kV and an incident ion-beam angle of 10°, followed by gentler milling at an acceleration voltage of 2.6 kV and an incident angle of 10° in order to get rid of surface amorphous material. The ion-milled samples were lightly carbon coated. The microstructures in the dolomite crystals were examined by using a spherical aberration-corrected FEG- STEM

(Titan 80-200) operating at 200 kV at the University of Wisconsin-Madison. This instrument can image single atoms with ~ 0.08 nm spatial resolution in STEM mode. Probe current was set at 24.5 pA. Collection angle of HAADF detector for acquiring all the Z-contrast images ranges from 54 to 270 mrad (Corresponding to 7.5 (1/Å) to 38.2 (1/Å) in reciprocal space).

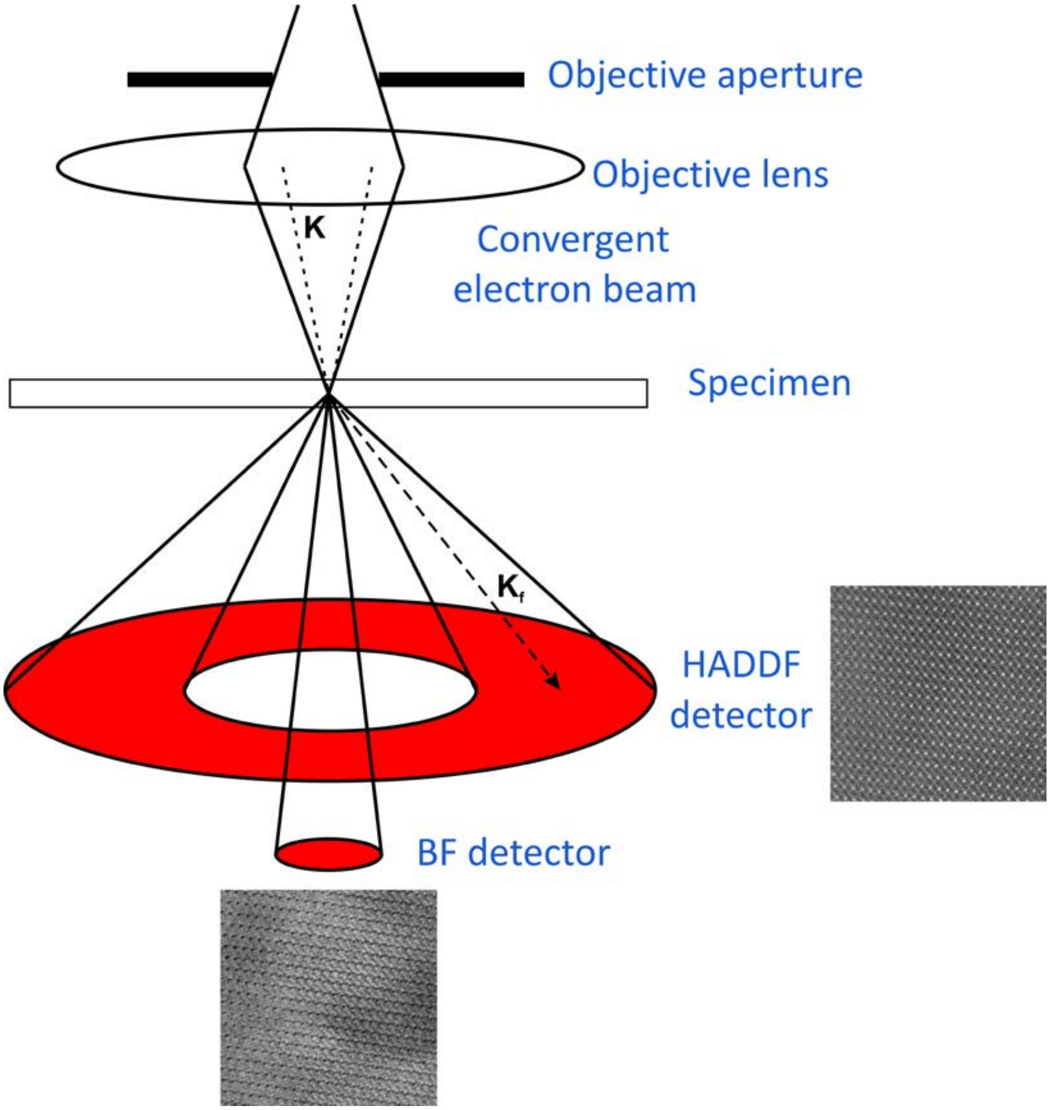

Figure 2.2.1 In STEM, the initial partial wave **K** in the probe are scattered by a thin sample to form a final plane wave $\mathbf{K}_\mathbf{f}$. Both BF and HADDF images of dolomite along [010]-zone axes has been shown close to the respective detector. The bright dots in HADDF image showing the Ca atoms (Ca is the heaviest atom in dolomite) aligned in (001) planes.

References

Kirkland, E.J. (1998) Advanced computing in electron microscopy. Plenum Press, New York, 250 pp.

Leng, Y. (2013) Materials characterization: introduction to microscopic and spectroscopic methods. John Wiley & Sons

Nellist, D.P. (2007) Scanning transmission electron microscopy. Science of Microscopy, I, 65-132.

Nellist, P.D. (2011) The Principles of STEM Imaging. In S.J. Pennycook and P.D. Nellist, Eds., Scanning Transmission Electron Microscopy pp. 91–116. Springer Science & Business Media, New York.

Pennycook, S. (2002) Structure determination through Z-contrast microscopy. Advances in imaging and electron physics, 173-206.

Pennycook, S. and Nellist, D. P. (2011) Scanning transmission electron microscopy: imaging and analysis. Springer

Shi, F. (2013) Advanced electron microscopy of novel ferromagnetic materials and ferromagnet/oxide interfaces in magnetic tunnel junctions. Ph.D. Dissertation, University of Wisconsin-Madison

Williams, D.B. and Carter, C.B. (1996) Transmission electron microscopy. Plenum Press, New York

Xu, H., Shen, Z., Konishi, H., and Luo, G. (2014a) Crystal structure of Guinier-Preston zones in orthopyroxene: Z-contrast imaging and ab inito study. American Mineralogist, 99, 2043–2048.

Xu, H., Shen, Z., and Konishi, H. (2014b) Si-magnetite nano-precipitates in silician magnetite from banded iron formation: Z-contrast imaging and ab initio study. American Mineralogist, 99, 2196–2202.

Chapter 3. “c” Reflections in Ca-rich Dolomite - caused by Dynamical Diffraction

3.1 Introduction

Four types of reflections have been found in the diffraction patterns of dolomite. “*a*” reflections refer to reflections that existed in the diffraction pattern of calcite (R-3c). The lack of *c* glides in the dolomite structure ($R\bar{3}$) due to the cation ordering causes the occurrence of extra reflections (*b* reflections, $h\bar{h}0l$, *l*= odd) in dolomite diffraction patterns compared to that of calcite (*a* reflections only) (Reeder, 1992). Two additional reflections (*c* and *d* reflections) have been observed in natural sedimentary dolomite. “*c*” reflections are very weak and usually streaked spots halfway between the principle reflections along any of the three directions of (110)*, (104)* and (012)* in the diffraction patterns of some dolomites (Reeder, 1981). The “*d*” reflections are satellites around “*a*” and “*b*” reflections, which were found in a few dolomite samples (Wenk and Zenger, 1983). The “*c*” type reflections are usually associated with the modulated microstructures in Ca-rich dolomite (Reeder and Wenk, 1979; Reeder, 1981; Van Tendeloo et al., 1985; Wenk and Zhang, 1985; Reksten, 1990a; Wenk et al., 1991; and Fouke and Reeder, 1992; Schubel et al., 2000).

The finely modulated microstructure in ancient calcian dolomite was first noticed by Reeder et al. in 1978, and is very common in calcian dolomite, some calcite and calcian ankerite (Reeder and Wenk, 1979; Reeder, 1981; Gunderson and Wenk, 1981; Van Tendeloo et al., 1985; Reeder and Prosky, 1986; Miser et al., 1987; Reksten, 1990a; Wenk et al., 1991; and Fouke and Reeder, 1992). Modulation can either be pervasive throughout a crystal, or intergrown with areas devoid of modulation. This modulation was ascribed to be compositional fluctuation associated with excess Ca in dolomite by Reeder (1981), who initially interpreted it to have arisen by reorganization in the solid state. However, some modulations were believed to have formed during growth, based on the fact that the orientations of modulations are different in different growth sectors of a dolomite crystal (Reeder and Prosky, 1986; Miser et al., 1987; Fouke and Reeder, 1992).

Although microstructures in dolomite have been studied for the past few decades, there are still debates over the causes of modulated microstructures and "*c*" reflections. With the development of the technology of the electron microscope, a spherical aberration-corrected scanning transmission electron microscope (STEM) can image single atoms directly with sub-Å (less than 0.1nm) spatial resolution and gather chemical and structural information using high-angle scattered non-coherent electrons (Kirkland, 1998). The purpose of this study is to investigate the microstructures in Ca-rich dolomite from the Ordovician Platteville Formation in western Wisconsin using this technique.

3.2 Samples

The rock sample collected from a partially dolomitized limestone outcrop in Prairie du Chien, Wisconsin, belongs to the Platteville Formation of the middle Ordovician Sinnipee Group. Euhedral dolomite crystals are found to grow in the micritic calcite matrix. The bulk rock sample was characterized by X-ray diffraction. Phase quantification using the Rietveld method is implemented in the Jade 9.0 Whole Pattern Fitting (WPF) program. The Rietveld refinement (Figure 3.3.1) shows that the dolomitized limestone contains 46% calcite, 42% dolomite, 5% quartz and 7% alkali feldspar by weight. In backscattered electron (BSE) images (Figure 3.3.2), euhedral dolomite crystals were composed of several compositionally distinct domains: BSE-bright unreplaced residual calcite, gray Fe-bearing dolomite grains and the dark host dolomite crystal. The average chemical compositions of the host dolomite and Fe-bearing dolomite determined by EMPA are $Ca_{1.14}Mg_{0.86}(CO_3)_2$ and $Ca_{1.06}Mg_{0.80}Fe_{0.14}(CO_3)_2$ respectively. Ca, Mg, Fe and Mn were measured with a CAMECA SX51 instrument at University of Wisconsin-Madison using wavelength-dispersive spectrometers at an accelerating voltage of 15 kV, a 10 nA beam current, and a ~1 μm beam diameter. Calcite, dolomite, siderite and rhodochrosite were used as standards for Ca, Mg, Fe and Mn respectively.

Specimens for STEM measurements were selected from areas containing large euhedral Ca-rich dolomite crystals (tens of microns in diameter) extracted from double-side polished thin sections and then ion milled. The thin sections were mounted in crystal bond that is soluble in acetone and then were removed from the glass slide after being immersed for 4-5 hours in acetone. The microstructures and interface structure between the inclusions and the host dolomite crystal were examined by using a spherical aberration-corrected FEG- STEM (Titan 80-200) operating at 200 kV at the University of Wisconsin-Madison.

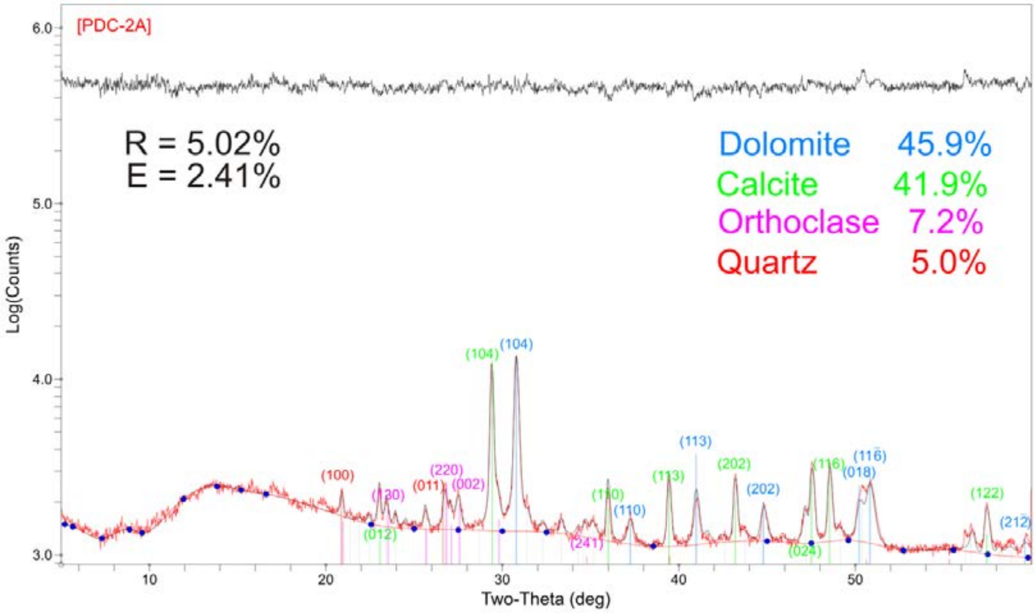

Figure 3.2.1 Result from Rietveld analysis of partially dolomitized limestone (PDC-2A). The top curve represents the residuals between the measured and calculated patterns. The agreement factors: weighted (R) and expected (E) values are 5.02% and 2.41% respectively.

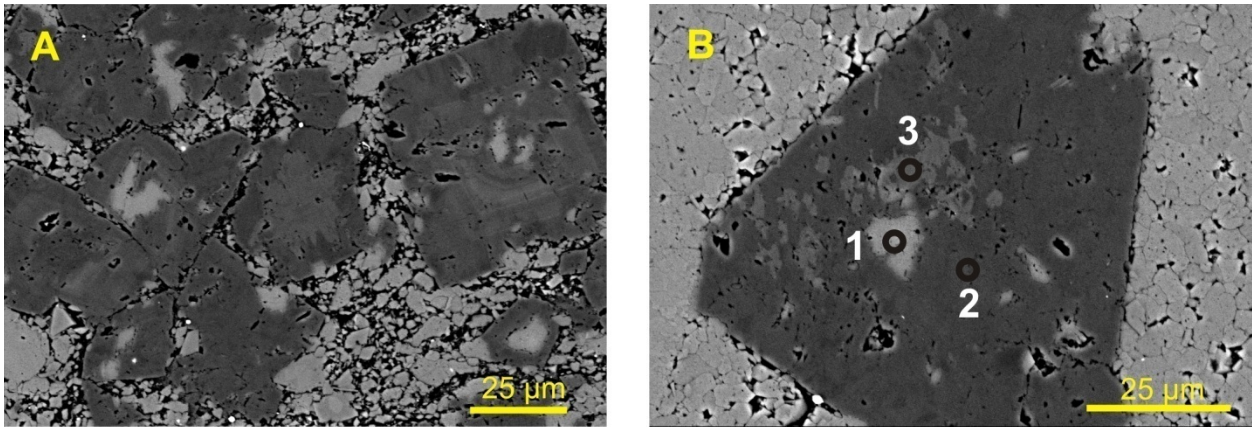

Figure 3.2.2 Backscattered electron (BSE) micrograph of single dolomite crystal in sample PDC-2. 3 phases are inside one dolomite crystal: (1) calcite, (2) Ca-rich dolomite and (3) Fe-bearing dolomite.

3.3 Results

3.3.1 Chemical Lamellae and “*c*” Reflections

Lamellae of bright contrast parallel to ~ (110) with wavelength ranging from 8 nm to 20 nm are evident in STEM images of the Ca-rich dolomite samples (Figure 3.3.1). The observed features are similar to the lamellae in a Ca-rich dolomite first noted by Reeder et al. (1978). The lamellae are shown to arise from fluctuations in calcium content, since they are visible in both BF and HAADF images (Figure 3.3.1). In the diffraction pattern (Figure 3.3.2), extra reflections occur midway between the 000 and the $(1\bar{1}2)$* spot and between 000 and (110)*. Note that extra reflections are streaked and parallel to (110)*. According to the Fast Fourier Transform (FFT) patterns of the bright field image (Figure 3.3.3A), these extra reflections correspond to areas with lamellae rather than areas free of lamellae. However, these “*c*” reflections do not exist in the FFT patterns of either area in the HAADF image (or Z-contrast image) that uses high-angle scattered incoherent electrons (Figure 3.3.3B).

Chemical lamellae were also observed in a high-resolution TEM image (Figure 3.3.4A) of the dolomite crystal viewed along the [010] zone axis (Figure 3.4.4B). The orientations of these lamellae vary from (001) to ~ $(\bar{1}01)$. Again, extra “*c*” reflections were found associated with some (but not all) of these lamellae that were not observed in lamellae-free regions (Figure 3.4.4C). The additional reflections were observed at ½$(1\bar{1}02)$* and ½(104)*. These extra reflections are those reported as “*c*” reflections in previous TEM works of rhombohedral carbonates (Reeder and Wenk, 1979; Reeder, 1981; Van Tendeloo et al., 1985; Reksten, 1990a; Wenk et al., 1991; Fouke and Reeder, 1992; Schubel et al., 2000). The fact that “*c*” reflections were not always observed for lamellae implies that the additional Ca was not always ordered.

It was proposed by Larsson and Christy (2008) that the “*c*” reflections in the diffraction pattern can be generated by superposition of diffraction from the host dolomite crystal and that from inclusions of material with similar cell parameters but the disordered calcite structure, in an orientation related to the host by (104) twinning (Figure 3.3.5A). Similarly, we can produce the "*c*" reflections along the (104)* and ($\bar{1}$02)* directions in the diffraction pattern by superimposing the diffraction from the host dolomite and that from calcite lamellae that have ($\bar{1}$02) twin-like relationship with the host dolomite (Figure 3.3.5B). The unit cell parameters of lamellae are same as those of the host dolomite.

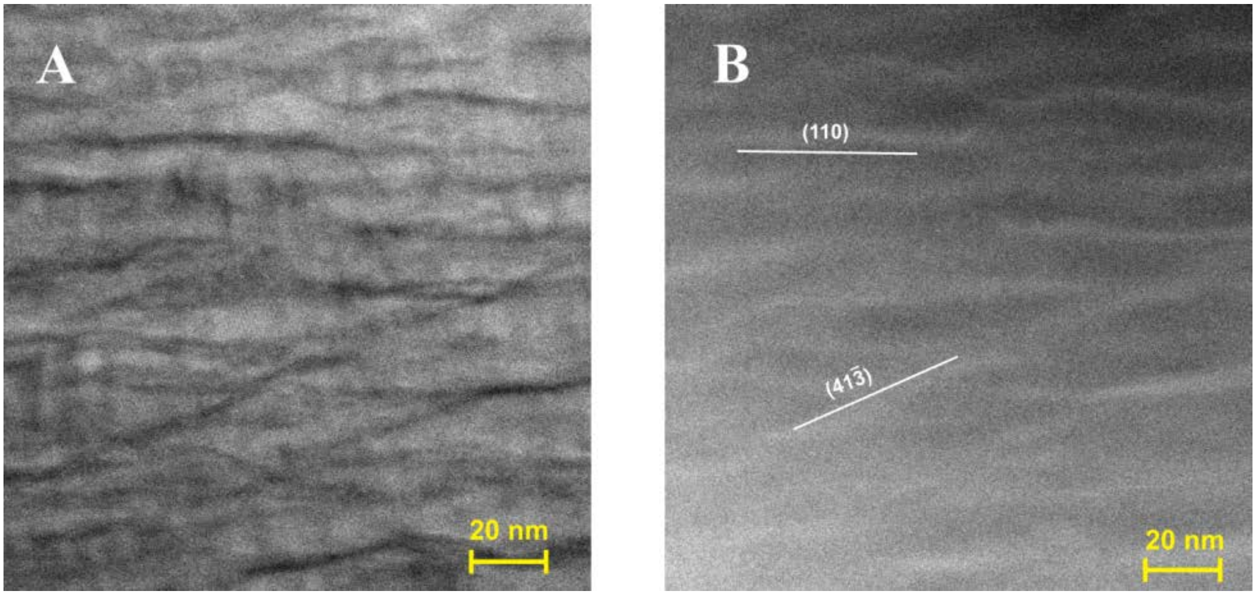

Figure 3.3.1 Bright field (A) and dark field (B) STEM images of the calcite lamellae in the same area of the Ca-rich dolomite. Strain contrast is evident in the BF image, but not in the DF image (B) due to collecting coherent electrons and incoherent electrons using different detectors.

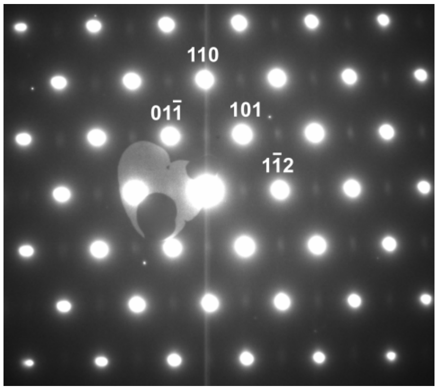

Figure 3.3.2 Diffraction pattern of [$\bar{1}$11] zone axis shows the c reflections along the (1$\bar{1}$2)* and (110)* directions in the Ca-rich dolomite.

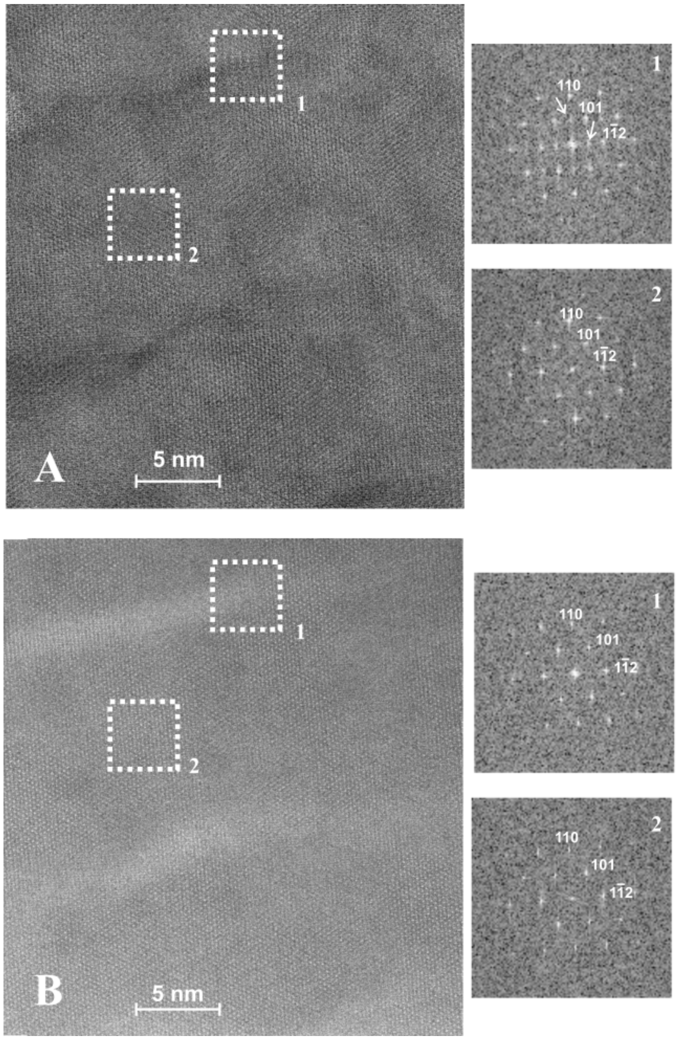

Figure 3.3.3 A (Top): The extra “*c*” reflections along (1$\bar{1}$2)* and (110)* directions exist in the FFT pattern (1) from the lamellar domains in the bright field image, but not in FFT pattern (2) of the host dolomite. B (Bottom): No “*c*” reflections in the FFT pattern (1) from the lamellar domains in Z-contrast image.

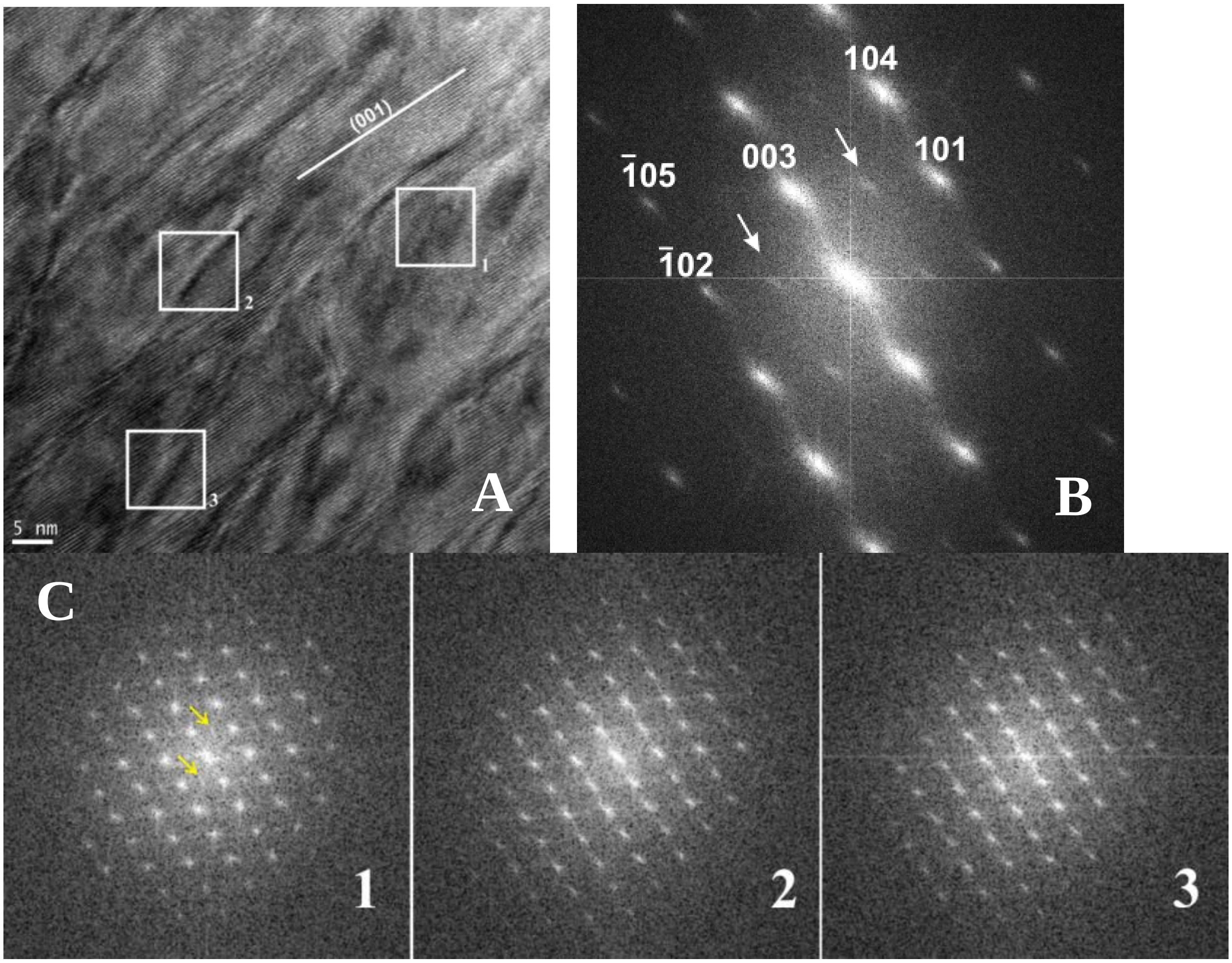

Figure 3.3.4 A: A [010]-zone axis HRTEM image of the Ca-rich dolomite shows the calcite exsolution lamellae. B. FFT pattern of the image showing "*c*" reflections along (104)* and (102)* (indicated by arrows). C: Extra "*c*" reflections exist in the FFT patterns from areas with overlapping features (e.g. region 1). The FFT patterns from lamellae with sharp boundaries do not show "*c*" reflections (region 2 and 3).

3.3.2 Qualitative Chemical Characterization of Ca-rich Lamellae

In Z-contrast image of the Ca-rich dolomite crystal from the same sample as shown in the HRTEM image, similar yet more regular bright linear features or modulations have been observed (Figure 3.3.6A). The orientations of the lamellae (or chemical modulations) are parallel to (101) ~ (104), mostly in the range between (205) and (104), with a few exceptions, such as parallel to ($\bar{1}$08). The distance between successive lamellae was 7-30 nm. No extra spots such as "*c*" reflections were observed in FFT patterns from Z-contrast

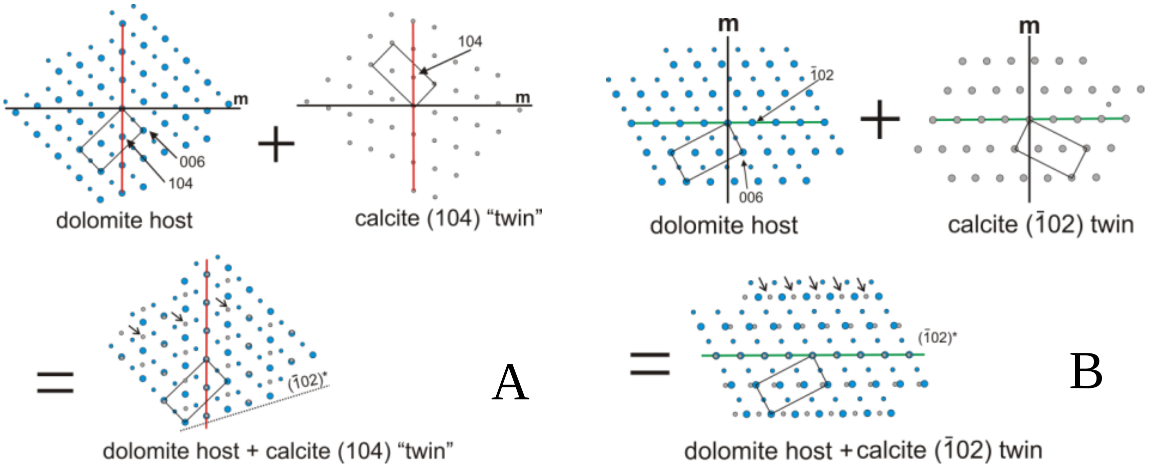

Figure 3.3.5 A: A "twin" model producing the "*c*" reflections along $(\bar{1}02)^*$ and $(104)^*$directions in the diffraction pattern by superposition of the diffraction of the dolomite host and that of the calcite (104) "twin" (modified from Larsson and Christy, 2008). The calcite "twin" has the same unit cell parameters as the dolomite host. The "m" plane represents the (104) twin plane. B: The overlap of the diffraction pattern of the dolomite host and that of the calcite $(\bar{1}02)$ twin may also result in the "*c*" reflections along $(\bar{1}02)^*$ and $(104)^*$directions.

images of the lamellar regions, which suggests that the additional Ca^{2+} ions do not form a superstructure when projected down the viewing direction. Intensity line profiles were taken parallel to the traces of $(\bar{1}02)$ planes in order to estimate the variation in Ca:Mg ratio across the bright lamellae, making use of the $Z^{1.7}$ dependence of intensity in the Z-contrast image. Viewing along [010] direction, Ca and Mg cation layers alternate along the $(\bar{1}02)$ traces in ideal dolomite. According to Figure 3.3.6B, the intensity associated with the Mg layers increases inside the linear features, which indicates the replacement of Mg^{2+} by Ca^{2+}. Assuming that the dolomite outside the lamellae is nearly stoichiometric, we estimated the composition of the lamellae qualitatively. The host dolomite has 0~3% excess of $CaCO_3$, and the lamellae have compositions ranging from $Ca_{0.85}Mg_{0.15}CO_3$ to $Ca_{0.70}Mg_{0.30}CO_3$. FFT patterns from the lamellae in some areas show weak *b* reflections such as (003). These weak spots are not from disordered calcite with $R\bar{3}m$ symmetry, but from areas overlapped with the host dolomite. The lamellae overlapped with were not used for line profile analysis of the Mg-calcite lamellae. All the compositions of the Mg-calcite compositions are based on the line profiles from the lamellae with $R\bar{3}c$ symmetry only.

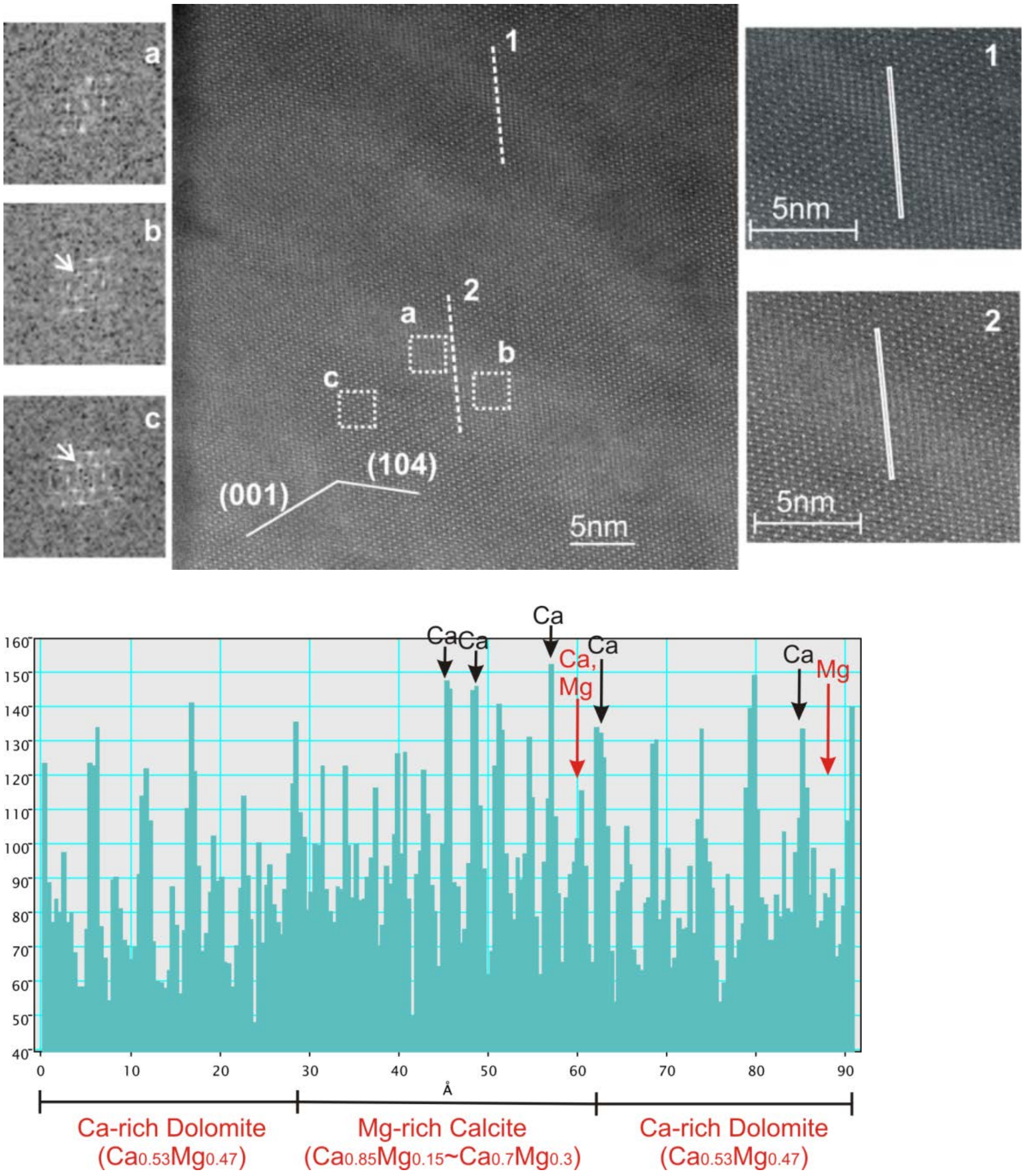

Figure 3.3.6 A (Top): Two line traverses ‘1’ and ‘2’ have been taken parallel to $(\bar{1}02)$ trace in order to examine composition variation at atomic resolution. Compare FFT patterns from a lamella (a), lamella overlapped with dolomite host (b), and the dolomite host (c). (003) reflection (arrowed) in FFT pattern (b) is from the dolomite host. B: (bottom): An intensity profile of line ‘1’ as shown in (A).

3.4 Discussion

The “*c*” type reflections usually accompanying the modulated microstructures are very common in Ca-rich dolomite. In this study, we found two of the three different kinds of “*c*” reflections, and as in previous work (Fig. 7c of Reeder 1981), we found that “*c*” reflections along the (104)* and ($\bar{1}$02)* directions or along (110)* and (1$\bar{1}$2)* directions exist in the same diffraction pattern. It has been reported that the “*c*” reflections can be either commensurate or incommensurate with the host structure (Schubel et al., 2000). It has been further proposed that “*c*” reflections form in domains with an ideal composition of $Ca_{0.75}Mg_{0.25}CO_3$ due to ordering of Mg and excess Ca in (001) planes, which doubles the periodicity in ***a*** direction (Van Tendeloo et al., 1985). In the alternative model of Larsson and Christy (2008), “*c*” reflections arise not from additional cation ordering, but due to superposition of diffraction patterns from a dolomite host and nanoscale calcite inclusions that are oriented in a (104) twin relationship to the host. We have shown that a similar model with ($\bar{1}$02) as the twin plane can produce some of the “*c*” reflections seen in this study. In the model of Larsson and Christy (2008), multiple scattering by matrix and twinned nanodomains completes the extra weak “*c*” reflections. Although “*c*” reflections appear in SAED patterns and FFT patterns of the HRTEM image and bright-field STEM images, they do not appear in FFT patterns of HAADF images (Z-contrast images). Note that Z-contrast imaging uses high-angle scattered and incoherent electrons and therefore avoids multiple diffraction problems from the overlapped twinned crystals. Conversely, electron diffraction and bright-field imaging (HRTEM and STEM BF imaging) uses low-angle scattered and coherent electrons that will result in multiple diffraction from any overlapped twin lamellae that are present. We deduce from the difference in FFT patterns for the different image types that observed "*c*" reflections arise from nanodomains of magnesian calcite in a twinned orientation relative to a dolomite host, and that have anomalous cell parameters similar to those of the dolomite host, as in Larsson and Christy (2008). If unit cell parameters of the magnesian calcite lamellae (especially coarse lamellae) are larger than those of the dolomite host, positions of the "*c*" reflections will be off the center, which were observed in a Ca-rich dolomite from the Latemar buildup (Schubel, et al., 2000).

Modulation in some dolomites has been interpreted as due to strain associated with high-Ca domains that formed by exsolution or during growth (Fouke and Reeder, 1992; Reeder, 1992). However, our STEM study shows that contrast results purely from the composition difference between Ca-rich lamellae and dolomite matrix. We did not find any evidence of growth zoning, and interpret the modulation to have arisen from exsolution during diagenesis. Initially, extra Ca ions substitute for Mg on the Mg layers of the dolomite structure at low temperature (Fig. 3.4.1A). These Ca ions then migrate to form lamellae that are oriented parallel to planes such as (110) or (104), probably to minimize interfacial strain with the host dolomite (Figure 3.4.1B, 3.4.1C). Carbonate ions may also re-orient so as to put these lamellae in a twinned orientation and adjust the local cell parameters to fit the host dolomite lattice. The lamellae are metastable, however, and given time or exposure to higher temperature, further cation migration and carbonate re-orientation will occur so that coarse exsolution lamellae of calcite are formed parallel to (001) of dolomite (Fig. 3.4.1D). Initial compositional difference in different sectors (Reeder and Prosky, 1986; Fouke and Reeder, 1992) may also affect orientation difference of the exsolution lamellae.

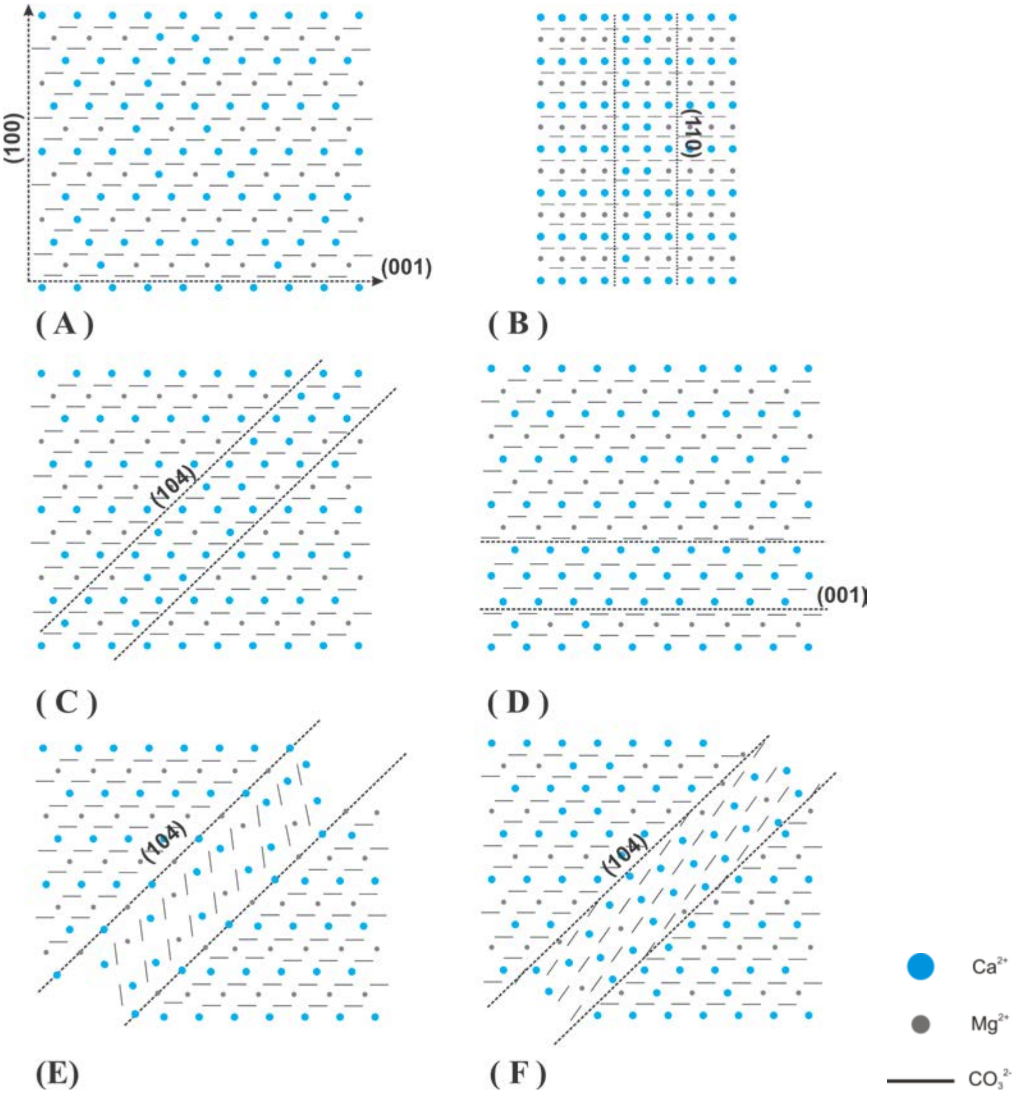

Figure 3.4.1 Proposed models for the formation of Ca-rich exsolution lamellae. (A) Initially, extra Ca^{2+} are incorporated into the Mg^{2+}-layers in dolomite structure. (B) These extra Ca^{2+} migrate within the Mg^{2+}-layers and concentrate in linear regions forming exsolution lamellae parallel to (110). (C) Exsolution lamellae parallel to (104). (D) Exsolution lamellae parallel to basal plane (001). Exsolution lamellae in (104) and $(\bar{1}02)$ twined relationship with the dolomite host are also proposed in E and F respectively.

References

Fouke, B.W. and Reeder, R.J. (1992) Surface structural controls on dolomite composition: evidence from sectoral zoning. Geochimica et Cosmochimica, 56, 4015-4024.

Gunderson, S.H. and Wenk, H.R. (1981) Heterogeneous microstructures in oolitic carbonates. American Mineralogist, 66, 789-800.

Kirkland, E.J. (1998) Advanced computing in electron microscopy. Plenum Press, New York

Larsson, A. and Christy, A.G. (2008) On twinning and microstructures in calcite and dolomite. American Mineralogist, 93, 103-113.

Miser, D.E., Swinnea, J.S., and Steinfink, H. (1987) TEM observations and X-ray crystal-structure refinement of a twinned dolomite with a modulated microstructure. American Mineralogist, 70, 1253-1261.

Nellist, D.P. (2007) Scanning transmission electron microscopy. Science of Microscopy, I, 65-132

Reeder, R.J. (1992) Carbonates: growth and alternation microstructures. In P.B. Buseck, Eds., Minerals and Reactions at the Atomic Scale: Transmission Electron Microscopy, 27, p. 381-424. Reviews in Mineralogy, Mineralogy Society of America, Washington, D.C.

Reeder, R.J. (1983) Crystal chemistry of the rhombohedral carbonates. In R.J. Reeder, Eds., Carbonates: Mineralogy and Chemistry, 11, p. 1-47. Reviews in Mineralogy, Mineralogical Society of America, Washington, D.C.

Reeder, R.J. (1981) Electron optical investigation of sedimentary dolomites. Contributions to Mineralogy and Petrology, 76, 148-157.

Reeder, R.J. and Wenk, H.R. (1979) Microstructures in low temperature dolomite. Geophysics Research Letters, 6, 77-80.

Reeder, R.J. and Prosky, J.L. Compositional sector zoning in dolomite. Journal of Sedimentary Research, 56, 237-247.

Reksten, K. (1990) Modulated microstructures in calcian ankerite. American Mineralogist, 75, 495-500.

Schubel, K.A., Elbert, D.C., and Veblen, D.R. (2000) Incommensurate c-domain superstructures in calcian dolomite from the Latemar buildup, Dolomites, Northern Italy. American Mineralogist, 85, 858-862.

Shannon, R.D. (1976) Revised effective ionic radii and systematic studies of interatomic distances in halides and chalcogenides. Acta Crystallographica, A32, 751-767.

Van Tendeloo, G., Wenk, H.R., and Gronsky, R. (1985) Modulated structures in calcian dolomite: a study by electron microscopy. Physics and Chemistry of Minerals, 12, 333-341.

Warren, J. (2000) Dolomite: occurrence, evolution and economically important associations. Earth-Science Reviews, 52, 1-81.

Wenk, H.R. and Zenger, D.H. (1983) Sequential Basal Faults in Devonian Dolomite, Nopah Range, Death Valley Area, California. Science, 222, 502-504.

Wenk, H.R., Meisheng, H., Lindsey, T., and Morris, J.W. (1991) Superstructures in ankerite and calcite. Physics and Chemistry of Minerals, 17, 527-539.

Wenk, H.R., and Zhang, F. (1985) Coherent transformations in calcian dolomites. Geology 13, 457-460.

This Chapter was previously published (*American Mineralogist*, 98 (2013), 760-766)

with the following coauthors:

Zhizhang Shen, Hiromi Konishi, Philip E. Brown, and Huifang Xu

NASA Astrobiology Institute, Department of Geoscience,

University of Wisconsin - Madison

Madison, Wisconsin 53706

Chapter 4. "*d*" Superstructure in Sedimentary Dolomite

4.1. Introduction

In section 3.1, the following basic crystallography about calcium-magnesium carbonate has been covered: the structure difference between calcite and dolomite and the reason for the difference, the four types of reflections in calcium-magnesium carbonate, the microstructures (chemical lamellae) in Ca-rich dolomite. In this chapter, the topic is the *d* reflection, which is far less common than *c* reflection in natural sedimentary dolomite samples. The *d* reflection was first observed in Devonian dolomite samples by Wenk and Zenger (1983) and has been also found in ankerite samples (Rekesten, 1990). The *d* reflections occur as satellites around *a* and *b* reflections with diffraction vector ~1/3 (000l)* and are usually streaking along *c** direction (Wenk and Zenger, 1983; Wenk and Zhang, 1985; Van Tendeloo et al., 1985).

In addition to experimental studies in mineralogy, the application of *ab initio* calculations of crystal structure, phase stability, and physical properties of minerals at given pressure and temperature has increased in the past few years (Ogonov et al., 2006; Barnard and Xu, 2008; Chatterjee and Saha-Dasgupta, 2010; Stackhouse et al., 2010). Density functional theory (DFT) uses the functional of electron density to solve the Schrödinger equation for a many electron system to acquire the minimum energy of the system (Scholl and Steckel, 2009). This method can calculate the enthalpy of a system at 0 K and the corresponding structure. Since STEM work only provides topological information for the crystal structure, the use of the DFT method is needed in this study to calculate the detailed crystal structure of the *d* phase and confirm our model for the *d* superstructure by comparing the energetic stability of our model to another model proposed in literature.

The “molar tooth” structure refers to vertical and horizontal ribbons and blobs of fine-grained calcite in a dolomite host (Bauerman, 1885). This structure has only been recognized in Mesoproterozoic and Neoproterozoic marine carbonate rocks with a few exceptions (Frank and Lyons, 1998). The origin and the temporally limited occurrence of molar tooth carbonate have bewildered geologists for over a century (James et al., 1998; Pratt, 1998; Meng and Ge, 2002; Marshall and Anglin, 2004; Pollock et al., 2006; Long, 2007; Kuang et al., 2012). However, no previous work on the nano-scale mineralogy of carbonates with the “molar tooth structure” has been conducted. In this present study, STEM imaging and DFT calculations were combined to provide a complete crystallographic description of the *d* superstructure.

4.2 Samples

The “molar tooth” carbonate samples were collected near Hungry Horse Dam, Montana, from outcrops of the Helena Formation of the Mesoproterozoic Belt Group (Frank and Lyons, 1998). The sample HHL-00H was chosen for STEM analysis. The TEM sample preparation procedure and STEM experimental conditions are described in chapter 2 and chapter 3. In the hand specimen of HHL-00H (Figure 4.2.1), the thin sinuous vertical and horizontal ribbons with width of ~0.2-1.5cm intersect each other. The “molar tooth” is composed of clean and fine-grained calcite crystals with similar size (~10 μm). The “molar tooth” host has three major phases: dolomite, calcite, and quartz (Figure 4.2.2). K-feldspar, illite, chlorite, rutile, and apatite are also present in the “molar tooth” host rock. The XRD powder analysis of the “molar tooth” host rock shows that the dolomite is cation-ordered with the presence of sharp (105) and (009) peaks. The dolomite has a composition of ~$Ca_{1.02}Mg_{0.98}(CO_3)_2$ based on the d_{104} value (2.890Å) and the relationship between d_{104} values and $MgCO_3$ content in ordered dolomite (Goldsmith and Graf, 1958; Zhang et al., 2010).

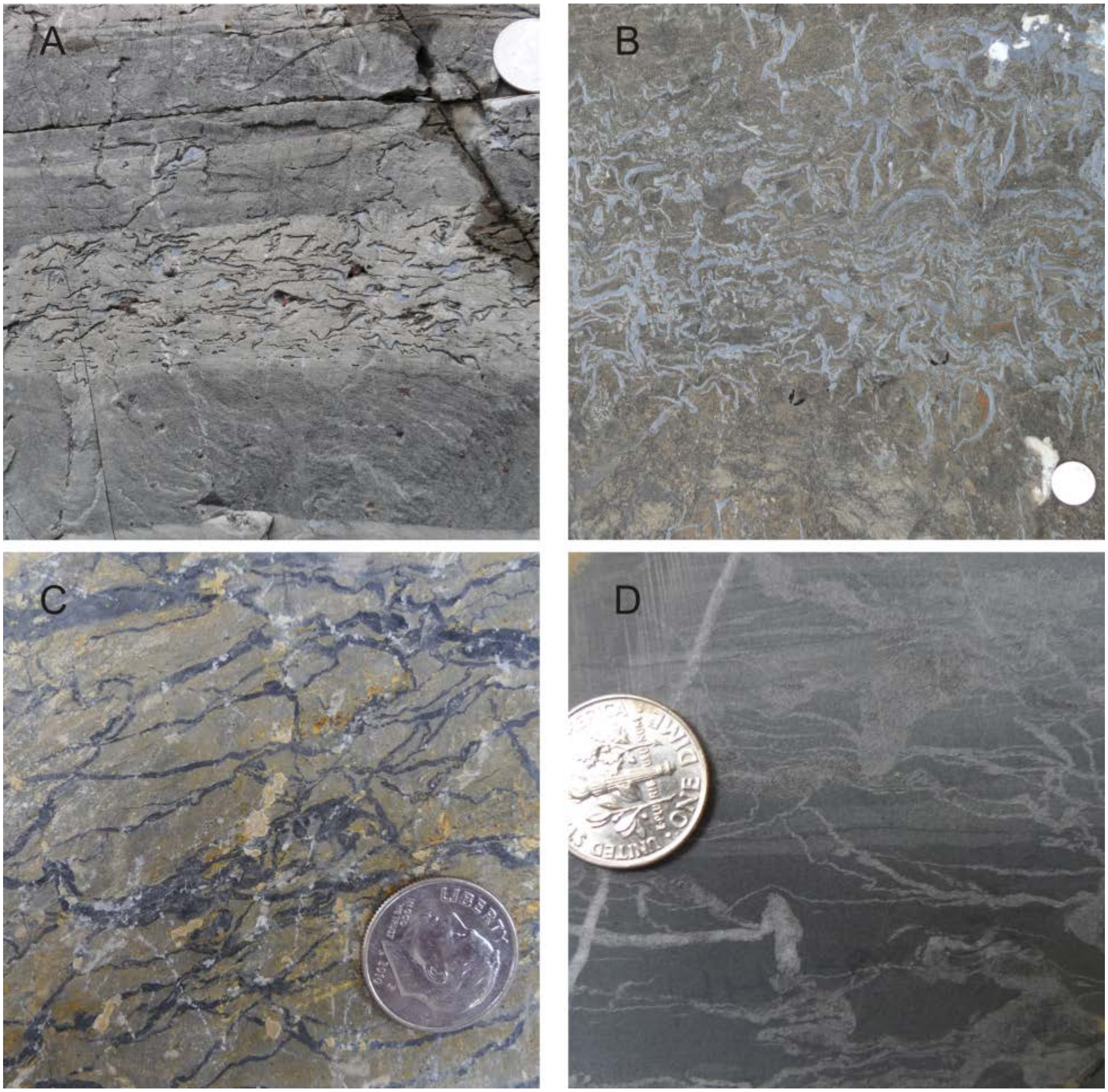

Figure 4.2.1 (A)The outcrop shows the elastic deformation inside the carbonate layers with "molar tooth" structure. (B) Sinuous dark blue riboons of fine crystallined calcite ("molar tooth") exist in the dolomite host that is weathered into buff color. (C) Weathered surface of HHL-00H specimen . (D) "Molar tooth" becomes light color in fresh cut surface of HHL-00H specimen.

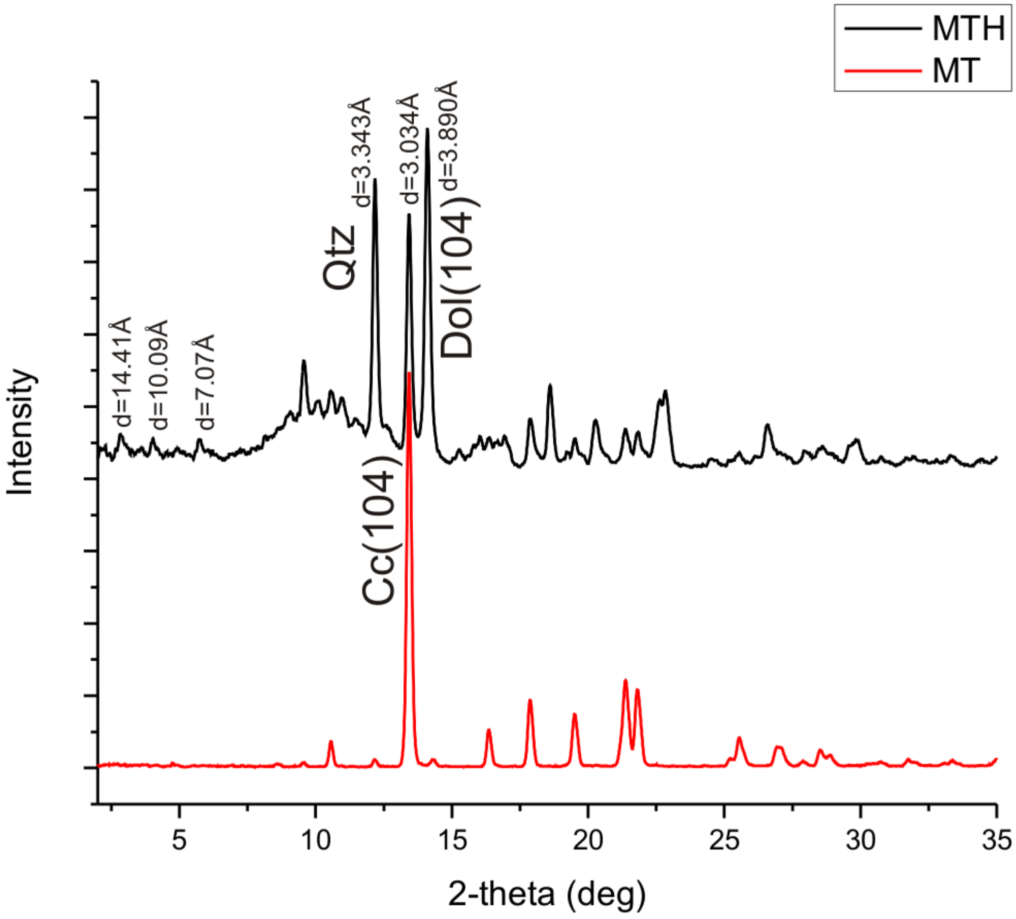

Figure 4.2.2. Powder XRD pattern of “molar tooth” host and “molar tooth” in sample HHL-00H.

4.3 Calculation details

The DFT calculations were performed by using the Vienna *ab initio* simulation package (VASP) (Kresse et al., 1996). The general gradient approximation (GGA) with the Perdew, Burke, and Ernzerhof (PBE) parameters was employed (Perdew et al., 1996). The projector-augmented wave (PAW) method with an energy cutoff of 600 eV was used. A conventional hexagonal supercell of calcite derived structures including 30 atoms or 6 chemical formula units was used. We tested k-point convergence and a mesh of 3×3×1 was found to be sufficient for the system. Two starting structures for the *d* phase: one with calcite's unit cell parameters from experiments (Graf, 1969) and another with dolomite's (Beran and Zemann, 1977). All the initial structures were optimized using the static energy minimization scheme, where both the shape and volume of the cell were allowed to relax. The structure with minimum energy calculated from the previous step was further calculated by *ab initio* molecular dynamics simulations at 10K to better explore the local minimum. The powder and electronic diffraction patterns of calculated structures were generated by CrystalDiffract® and SingleCrystal™ respectively.

4.4 High-Resolution (S)TEM Observations

In HRTEM images, the modulated microstructures with strong strain contrast are prevalent through the "molar tooth" host dolomite. Calcite inclusions that are a common phenomenon in sedimentary dolomites can be easily recognized because of being free of modulations (Figure 4.4.1). Diffuse streaks along $\boldsymbol{c^*}$ occur in the electron diffraction pattern of the host dolomite (Figure 4.4.2). Some maxima of the streaks are about one third of d_{006}^{*} (Fig. 4.4.2, and also see diffraction patterns of Wenk and Zenger, 1983; Wenk and Zhang, 1985). According to the Fast Fourier Transform (FFT) patterns of different areas in the dolomite images, the streaks in the diffraction pattern come from the precipitates with linear features that are parallel to (001) (Figure 4.4.3). However, the precipitates themselves are arranged in such a way that they are roughly parallel to $(1\bar{1}4)$. The observations above match the features of *d* reflections that were first described by Wenk and Zenger (1983). It was proposed that the streaks parallel to $\boldsymbol{c^*}$ could be from stacking disorder (Van Tendeloo et al., 1985).

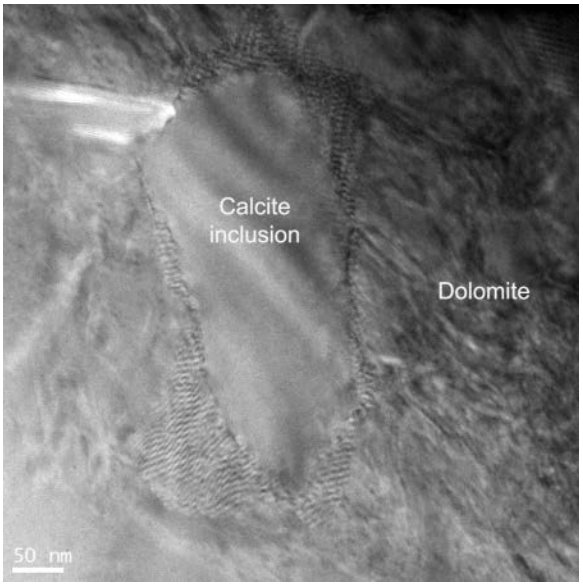

Figure 4.4.1 TEM image shows a calcite inclusion that is free of modulations or strain contrast exists in Ca-rich dolomite host that is with a lot of modulations.

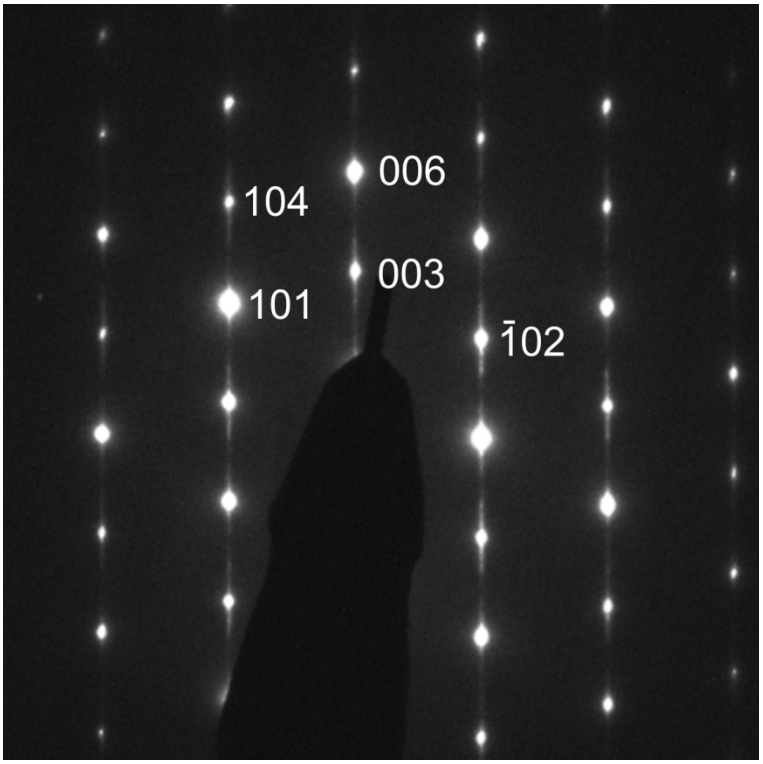

Figure 4.4.2 The diffuse streaks along c* occur in the diffraction pattern of Ca-rich dolomite from Helena Formation, Montana. The vector length is roughly around 1/3 of d^*_{006}.

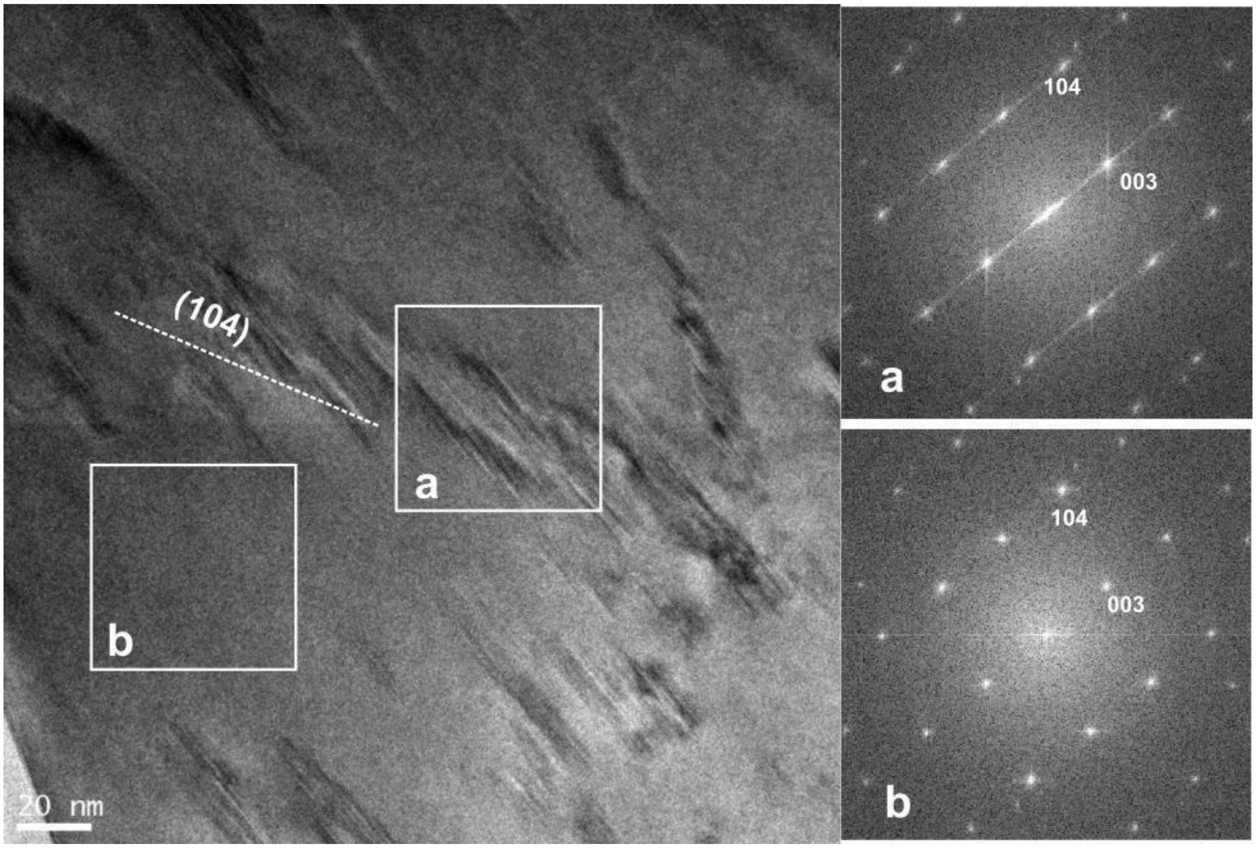

Figure 4.4.3 FFT patterns from TEM images show that the "d" reflections are corresponding to domains with //(001) linear feature (compare the FFTs from zone a and zone b). The //(001) modulations are arranged parallel to (104).

The dark areas of the precipitates in the bright field (BF) image under STEM mode become bright areas in the HAADF image (Figure 4.4.4), which suggests higher Ca contents in the precipitates than the host dolomite. The occurrence of *d* reflections in the FFT pattern of the HAADF image excludes the possibility that they are caused by multiple diffraction. In the HAADF of high magnification or Z-contrast image (Figure 4.4.5), the alternating bright and dark layers along ***c*** axis represent the alternating Ca and Mg layers in the normal dolomite structure. However, the *d* dolomite precipitate has the cation sequence of Ca-Ca-Mg-Ca-Ca-Mg- (Figure 4.4.5). The FFT pattern of this domain shows that the *d* reflections are attributed to this superstructure. This observation is different from the previous model for the *d* superstructure in which every third Mg layer is replaced by a Ca layer producing a sequence of Ca-Mg-Ca-Ca-Ca-Mg- (Wenk and Zhang, 1985). But both sequences produce the same chemical stoichiometry of $Ca_{0.67}Mg_{0.33}CO_3$. However, the repetition along the ***c***-axis is doubled in the previous model with respect to the observed Ca-Mg ordering in the Z-contrast image (Figure 4.4.5).

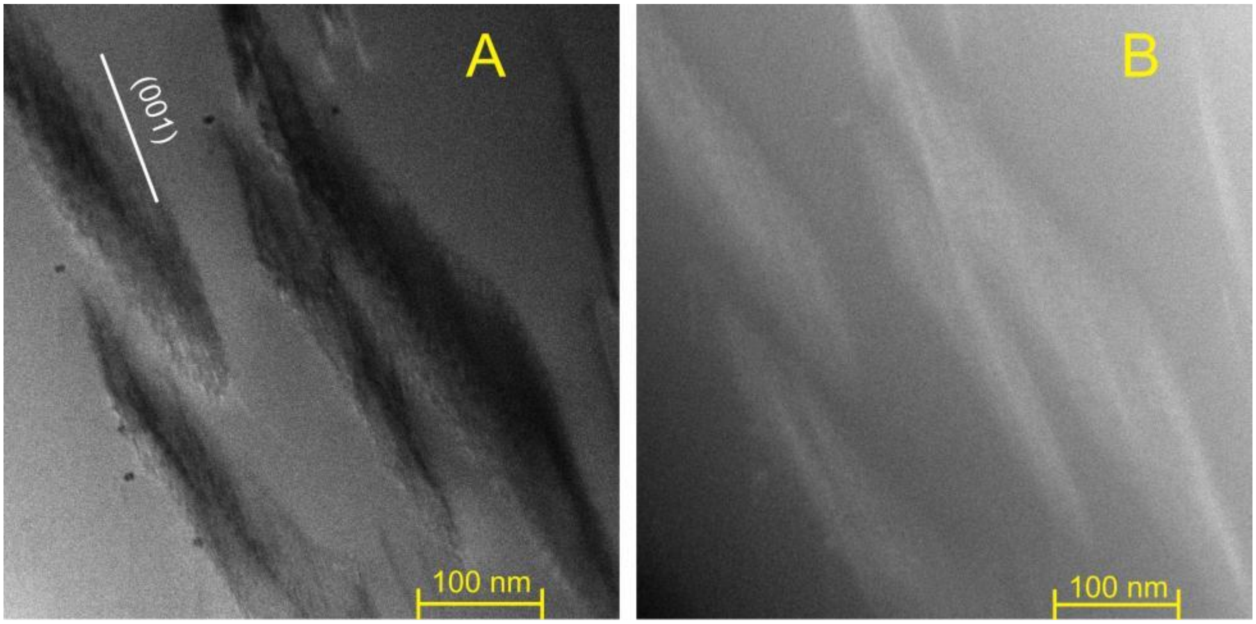

Figure 4.4.4. The dark domains of *d* superstructure in the bright-filed image (left) under STEM mode become bright in HAADF image (right), which means higher Ca content in the domains of *d* superstructure than the host dolomite.

Mg-bearing calcite precipitates are also observed in the dolomite (Figure 4.4.6). Along the ($\bar{1}02$) trace, the calcite exsolution region has six consecutive Ca layers as opposed to the dolomite host that has alternating Ca and Mg layers. In the line profile of the calcite region, some Ca columns have slightly lower intensities than the pure Ca columns in the dolomite host, which suggests the existence of a small amount of Mg in this calcite precipitate (Figure 4.4.6). This calcite exsolution is similar to Mg-calcite precipitates in Ca-rich dolomite (Shen et al., 2013).

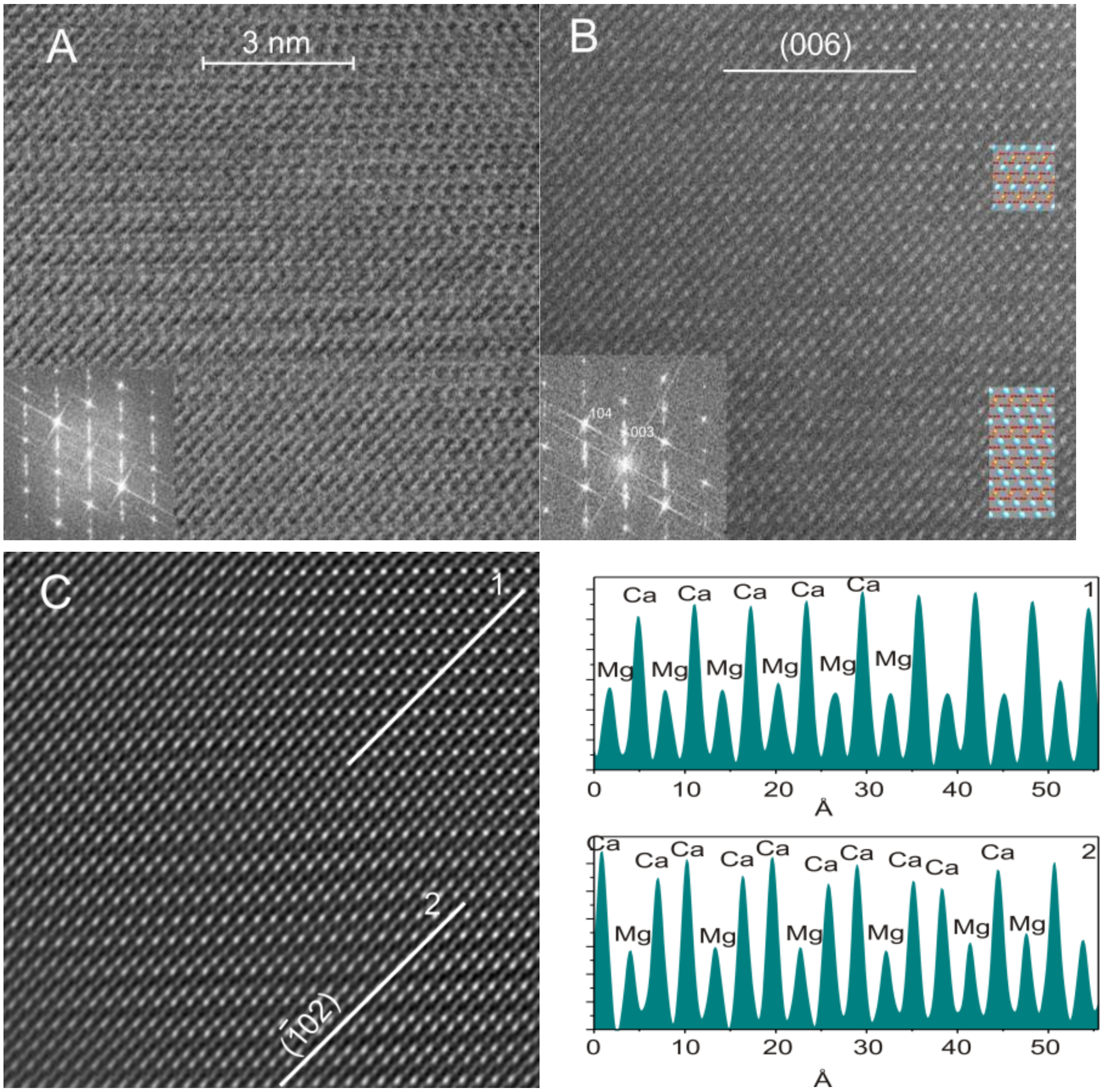

Figure 4.4.5 High magnification bright field (A) and dark filed (B) STEM images of *d* domains. Z-contrast (dark filed) images show that *d* domains have a cation sequence (bottom-right) of Ca-Ca-Mg-Ca-Ca-Mg-Ca along *c* axis as opposed to dolomite cation sequence as shown in the middle-right corner. The occurrence of streaking or splitting along *c** or *d* reflections (see the two separate reflections satellite the (003) reflection) in the FFT pattern (bottom-left corner) of the HAADF image excludes the possibility that it is caused by multiple diffraction in TEM mode. In inverse FFT image (C) from FFT pattern of Z-contrast image (B), cation sequence feature is enhanced and double-confirmed in the line profile.

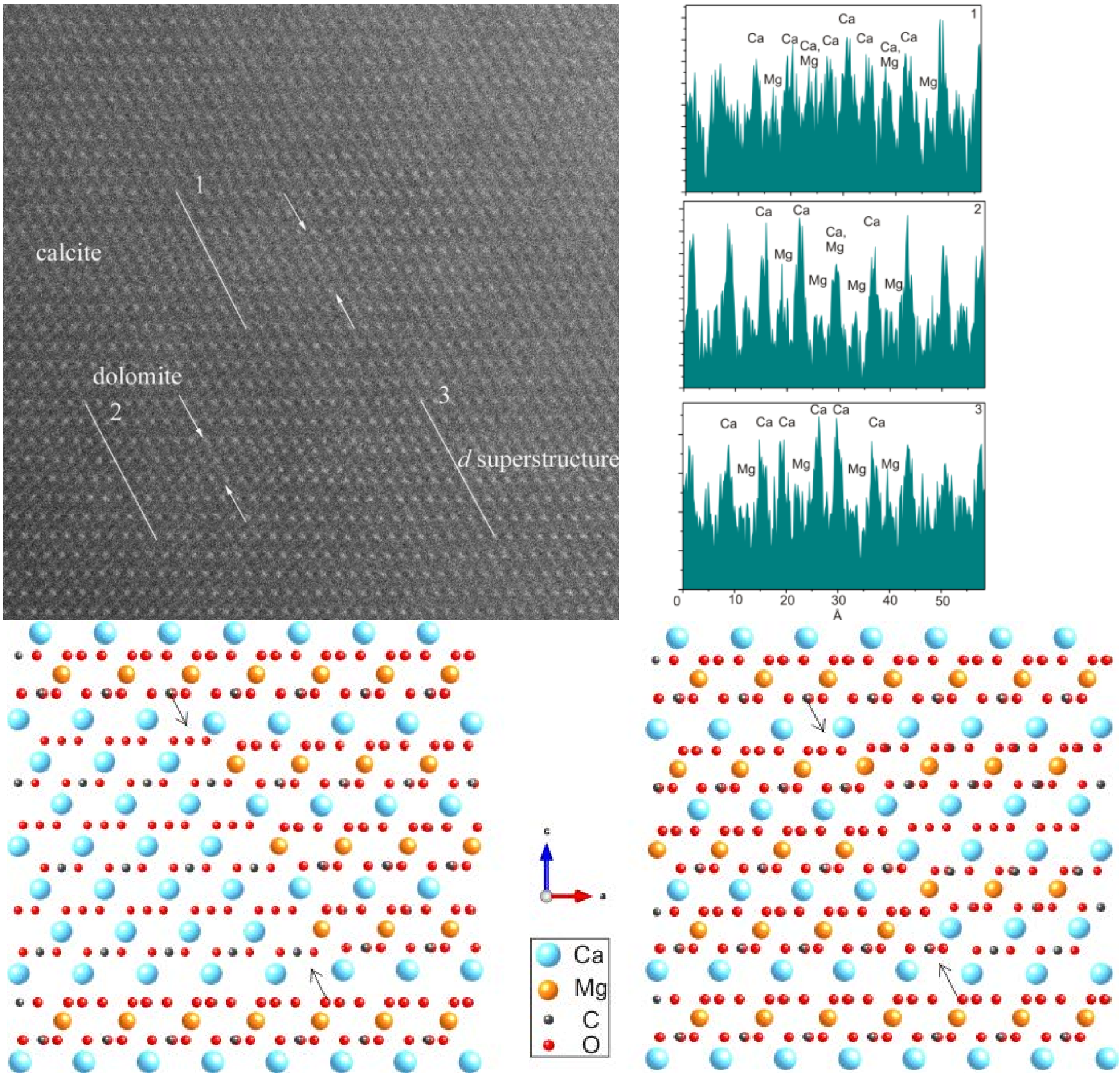

Figure 4.4.6 Calcite exsolution lamellae // (001) exist in dolomite host. The line profile 1 has six consecutive Ca columns along $(\bar{1}02)$ trace. The line profile 2 of the dolomite region shows the normal dolomite cation sequence of alternating Ca and Mg columns. The line profile 3 shows one repeat of *d* superstructure. The lines with arrows show the boundaries between calcite and dolomite and between dolomite and *d* superstructure. The atomic models for dolomite/calcite and dolomite/*d* phase interfaces are shown at the bottom. Carbonate group are not shown proportionally in order to highlight the cation sequences.

4.5 DFT Calculations

The structural parameters for the optimized *d* superstructure from DFT calculations are listed in Table 4.5.1. Tables 4.5.2 and 4.5.3 compare the calculated lattice parameters of dolomite and calcite structures with the reported experimental data. The calculated equilibrium volumes for both dolomite and calcite are slightly smaller than the reported data, the underestimation of the ***c*** parameter being the major contribution, but are still within the range of previous theoretical calculation data (see Table 4.5.2 and 4.5.3). The calculated values are for the structures at 0K. The reported experimental values were measured at ambient environment. Temperature could be a factor for the small discrepancy between calculated and measured the unit cell volumes. A small discrepancy between calculated and experimental values of lattice parameters is not uncommon for DFT calculations and may result from the use of an approximate exchange-correlation potential (Hossain et al., 2011). In spite of this discrepancy, the trend found in experimental data is maintained in our DFT calculations. The calculated *d* superstructure has an ***a*** parameter close to that of dolomite but has a ***c*** parameter closer to stoichiometric calcite. This finding is consistent with the observation from the diffraction patterns of the *d* superstructure that the difference between ***a*** parameters of dolomite and the *d* superstructure is smaller than that between ***c*** parameters, even though the DFT calculations are unconstrained bulk structure calculations. This trend is reasonable because superstructure precipitates share the (001) interface with the host dolomite. Smaller differences in the ***a*** dimensions between the host dolomite and d superstructure would cause less strain at the interface.

Lattice parameters	**a (Å)**	**c (Å)**	**V (Å^3)**	**C-O bond (Å)**	**Ca-O bond (Å)**	**Mg-O bond (Å)**	
This study	4.879	16.260	335.226	1.294, 1.297	2.355, 2.374	2.085	
Atom	**x**	**y**	**z**	**Atom**	**x**	**y**	**z**
Ca1	0.00000	0.00000	0.00000	Ca2	0.33333	0.66667	0.18457
Mg	0.66667	0.33333	0.34229	C1	0.66667	0.33333	0.09229
C2	0.00000	0.00000	0.26849	C3	0.33333	0.66667	0.41608
O1	0.66667	0.06803	0.09229	O2	0.28361	0.04018	0.26739
O3	0.04972	0.62648	0.41719				

Table 4.5.1. Lattice parameters for “*d*” superstructure and fractional coordinates of atoms in “*d*” superstructure (space group: *P31c* (no. 159)) calculated from DFT calculations.

Lattice parameters	**This work**	**Experimental**	**Theoretical**
a (Å)	4.810	4.808[a], 4.812[b]	4.787[c], 4.877[d], 4.858[e]
c (Å)	15.704	16.010[a],16.020[b]	15.55[c], 16.285[d], 16.109[e]
V (Å^3)	314.611	320.504[a],321.251[b]	308.623[c],335.409[d],329.248[e]
C-O bond (Å)	1.294	1.233[a], 1.286[b]	1.286[c], 1.299[d]
Ca-O bond (Å)	2.358	2.405[a], 2.382[b]	2.328[c], 2.401[d]
Mg-O bond (Å)	2.069	2.114[a], 2.087[b]	2.071[c], 2.314[d]
O-Mg-O bond angles (˚)	89.03, 90.97, 180	89.17, 90.83, 180[a]	89.335, 90.645, 180[c] 88.546,91.454,180[d]

[a] Graf ; [b] Beran and Zemann; [c] Hossain et al., LDA functional was used; [d] Hossian et al., GGA functional was used; [e] Bakri and Zaoui, fitted to Birch-Murnaghan equation of state.

Table 4.5.2. Calculated structural parameters of dolomite as compared to the previous experimental and theoretical data.

Lattice parameters	**This work**	**Experimental**	**Theoretical**
a (Å)	4.995	4.990[a]	5.061[b], 4.981[c]
c (Å)	16.6685	17.062[a]	17.097[b],15.902[c]
V (Å^3)	360.453	367.916[a]	379.279[b], 341.676[c]
C-O bond (Å)	1.295	1.286[a]	
Ca-O bond (Å)	2.336	2.357[a]	

[a] Graf; [b] Ayoub, Zaoui, and Berghout; [c] Aydinol et al.

Table 4.5.3. Calculated structural parameters of calcite as compared to the previous experimental and theoretical data.

The C-O bonds in CO_3^{2-} groups are rigid and the C-O distances in both experimental and calculation data are constant no matter what the actual composition of the carbonate mineral is. It is interesting to note that the C-O distances in the *d* superstructure are divided into two categories (Table 4.5.1): 1.294Å when a CO_3^{2-} layer is between Ca^{2+} and Mg^{2+} layers along the c axis; and 1.297Å when a CO_3^{2-} layer is in between two Ca^{2+} layers. DFT calculations predict slightly shorter Ca-O and Mg-O bonds in dolomite and calcite than experimental data (Table 4.5.2 and 4.5.3). The Mg-O distance in the *d* superstructure increases from 2.069Å in calculated dolomite to 2.085 Å. The Ca-O distance in the *d* superstructure differs depending on the oxygen positions; the Ca-O distances (2.374 Å) are larger when the oxygen ions are from CO_3^{2-} group sitting in between Ca^{2+} and Mg^{2+} layers than those (2.355 Å) from CO_3^{2-} group between two Ca^{2+} layers. This is because that the CO_3^{2-} layers are closer to Mg^{2+} layers than Ca^{2+} layers due to the smaller Mg^{2+} radius. The inversion center is missing in the *d* superstructure while the c glide is retained. The existence of (100) and (200) reflections in the diffraction pattern proves that it is not a rhombohedral unit cell, but a primitive hexagonal (Figure 4.5.1.C). Therefore, the space group is determined to be *P31c* (No. 159). The atom coordinates and symmetry equivalent positions of the *d* superstructure are reported in Table 4.6.1.

The superstructure with cation sequence of Ca-Mg-Ca-Ca-Ca-Mg-Ca that was proposed to explain the *d* reflections was referred to as δ structure (Wenk and Zhang, 1985; and Wenk et al., 1991) (see Figure 4.6.1A for details). The calculated δ structure has slightly larger unit cell parameters (a = 4.883Å and c = 16.281Å) than the *d* superstructure indicated here. The enthalpy of a unit cell of δ structure is slightly higher than that of the *d* superstructure by 0.54 kJ/mol per MCO_3 unit. The previously proposed δ structure is unstable with respect to the current *d* superstructure. The proposed δ structure model was based on the assumption that overlapped diffraction patterns from host dolomite and *d* superstructure were from the precipitates only (Wenk and Zhang, 1985). Careful examination of their diffraction pattern (Fig. 1A of Wenk and Zhang, 1985) and our FFT pattern (Figure 4.5.1D), show that the position of 003 is not half way between 002 and 004 of the *d* superstructure, and the position of 009 is not midway between 008 and 0010 of the *d* superstructure. The *d* superstructure does not have reflections with odd *l* due to its *c*-glide. A powder X-ray diffraction pattern with d_{104} value of 2.930Å for the *d* superstructure is also calculated (Fig. 4.5.2).

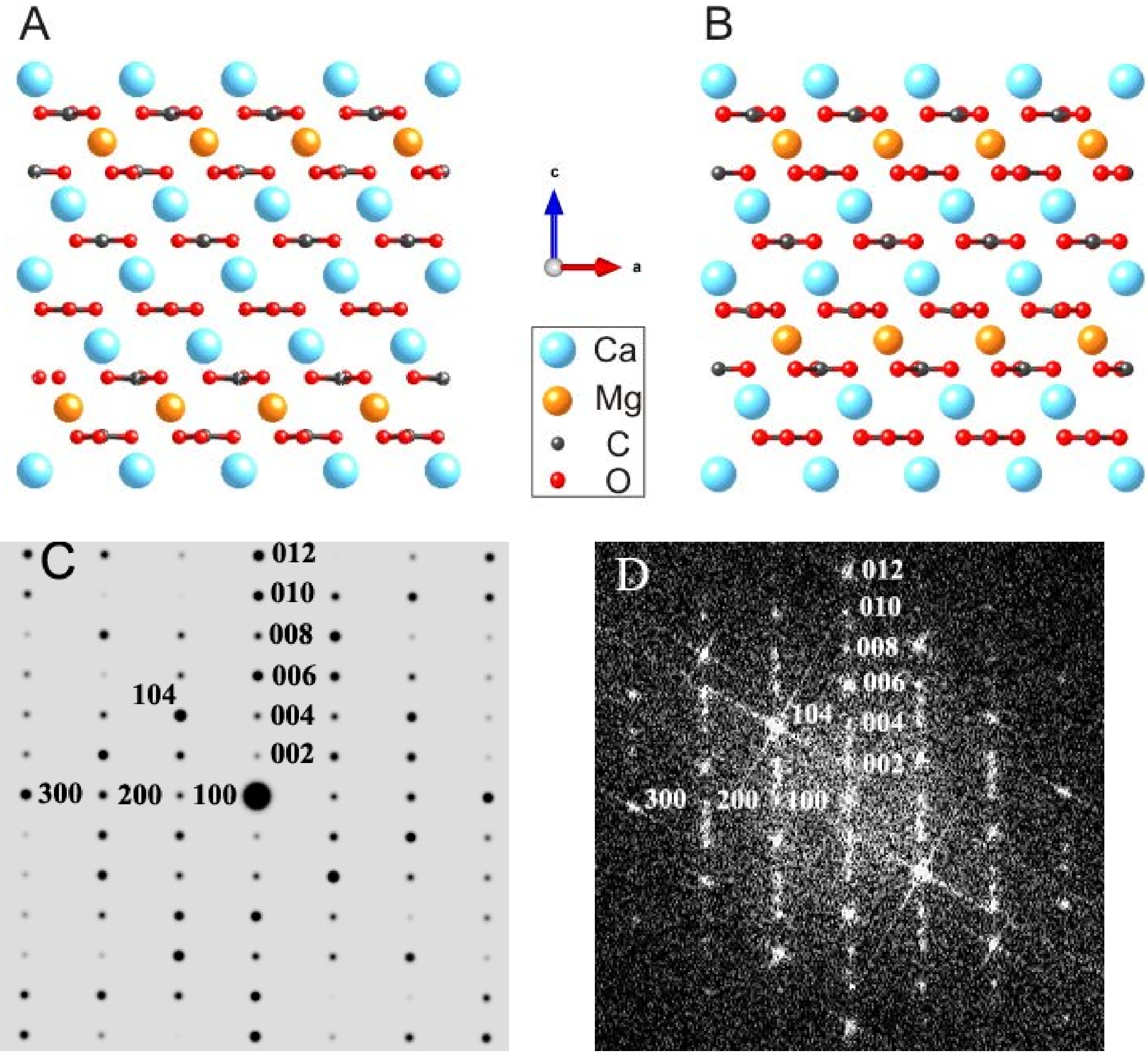

Figure 4.5.1 previously proposed structure model (A), and calculated model for *d* superstructure (B), and corresponding calculated electron diffraction pattern (C), compared to the FFT pattern (D) from the *d* superstructure. Very weak 003 and 009 reflections also occur in FFT pattern due to contributions from the dolomite. However, the position of 003 is not at the center of 002 and 004

of the d superstructure, and the position of 009 is not at the center of 008 and 0010 of the d superstructure. The d superstructure does not have reflections with odd *l* due to its *c*-glide.

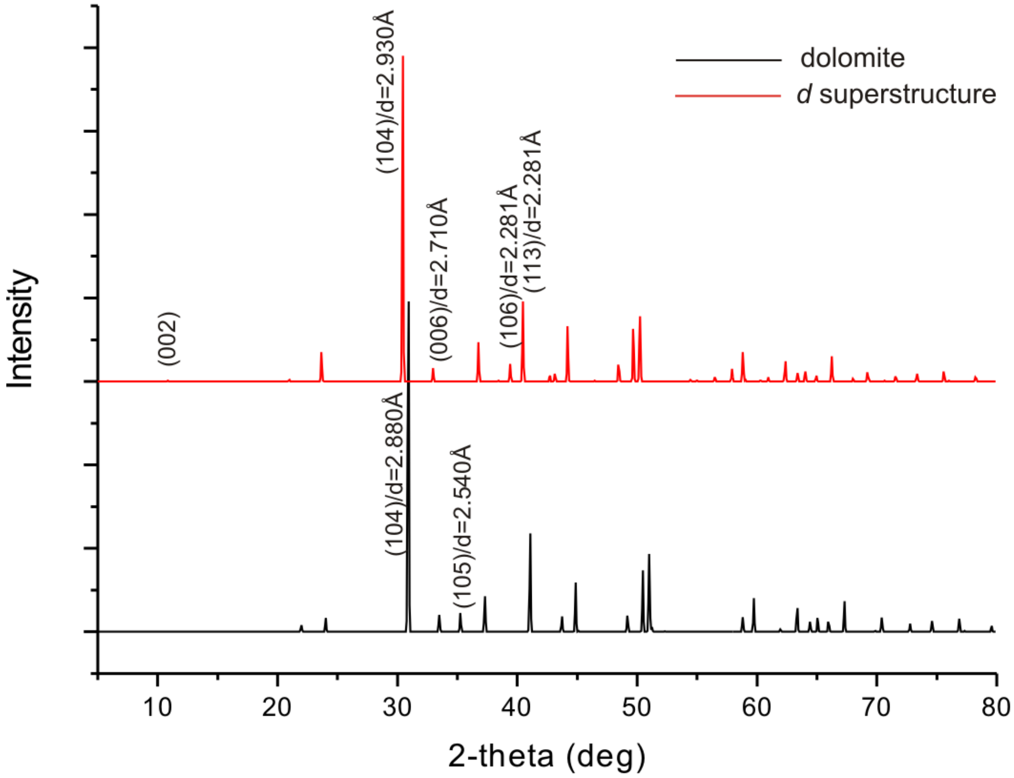

Figure 4.5.2 Calculated powder diffraction patterns of the d superstructure and stoichiometric dolomite (copper K-alpha radiation).

4.6 Implications

The calculated energies of calcite (Ca(CO3)), dolomite ($CaMg(CO_3)_2$), and d superstructure ($Ca_2Mg(CO_3)_3$) are -3620.64, -7132.37 and -10740.22 kJ/mol, respectively. The energy for the *d* superstructure ($Ca_2Mg(CO_3)_3$) is higher (~4.2 kJ/mol per MCO_3 unit) than the sum of the calculated energies from dolomite ($CaMg(CO_3)_2$) and calcite ($CaCO_3$) end members. The *d* superstructures serve as a metastable phase with respect to the stoichiometric dolomite and calcite. The *d* superstructures have a maximum of 4 repeats of Ca-Ca-Mg- along the c axis (< 35Å) in our sample and are only stable within dolomite host in the form of nano-precipitates. It is very difficult for extra Ca ions in the dolomite structure to diffuse through carbonate layers and to congregate to form lamellae parallel to the basal plane at low temperature (Wenk et al., 1991; Shen et al., 2013). This explains all the reported occurrences of nano-precipitates of *d*-reflections in natural samples. Wenk et al. (1991) summarized the various proposed superstructures of Ca-Mg carbonates. By using Z-contrast imaging, we can image the cation ordering directly and propose a more accurate structure model. By using the DFT method, we can calculate the detailed structures and explore the energetics of these metastable nano-phases. The methods may be applied to understand many other nano-phases, where there are challenges or artifacts by using other methods.

It was proposed that precursor for the molar tooth dolomite is gelatin-like carbonate mud that is rich in microbial extracellular polymeric substance (EPS) (James et al., 1998; Pollock et al., 2006; Long, 2007). Polysaccharides are the dominant components in the EPS. Z-contrast images of the Ca-rich dolomite show two types of Ca-rich precipitates in the host dolomite. Polysaccharides in the carbonate muds can preferentially promote formation of Ca-rich protodolomite (Zhang et al., 2012). Late stage aging during diagenesis and low-grade metamorphism resulted in the observed nano-precipitates of Mg-calcite and the *d* superstructure. Low-temperature non-stoichiometric dolomite with the observed nano-precipitates may be used as a biosignature.

The observed intermediate phases are analogous to those locally ordered domains in mixed-layer clay minerals, such as interstratified chlorite/serpentine, chlorite/biotite, and chlorite/pyrophyllite minerals (Banfield and Bailey, 1996; Xu and Veblen, 1996; Xu et al., 1996; Wang and Xu, 2006). The observed intermediate phase between calcite and dolomite may be described as interstratified calcite/dolomite, instead of δ–dolomite or *d*-dolomite.

References

Aydinol, M., Mantese, J. and Alpay, S. (2007) A comparative *ab initio* study of the ferroelectric behaviour in KNO_3 and $CaCO_3$. Journal of Physics: Condensed Matter, 49, 496210

Ayoub, A., Zaoui, A. and Berghout, A. (2011) High-pressure structural phase transitions and mechanical properties of calcite rock. Computational Materials Science, 3, 852-857

Bakri, Z. and Zaoui, A. (2011) Structural and mechanical properties of dolomite rock under high pressure conditions: A first principles study. physica status solidi (b), 8, 1894-1900.

Banfield, J.F., and Bailey, S.W. (1996) Formation of regularly interstratified serpentine – chlorite minerals by tetrahedral inversion in long-period serpentine polytypes. American Mineralogist, 81, 79-81.

Barnard, A. S. and Xu, H. (2008) An environmentally sensitive phase map of titania nanocrystals. ACS NANO, 2 (11), pp 2237–2242

Beran, A. and Zemann, J. (1977) Refinement and comparison of the crystal structures of a dolomite and of an Fe-rich ankerite. Tschermaks mineralogische und petrographische Mitteilungen, 4, 279-286

Chatterjee, S. and Saha-Dasgupta, T. (2010) First-principles simulations of structural, electronic, and magnetic properties of vacancy-bearing Fe silicates. Physical Review B, 15, 155105

Frank, T.D. and Lyons, T.W. (1998) “Molar-tooth” structures: A geochemical perspective on a Proterozoic enigma. Geology, 8, 683-686

Goldsmith, J.R., and Graf, D.L. (1958) Relation between lattice constants and composition of the Ca-Mg carbonate: American Mineralogist, 43, 84-101

Graf, D. (1969) Crystallographic tables for the rhombohedral carbonates. A correction. American Mineralogist, 325

Kuang, H., Liu, Y., Peng, N., Luo, S., Li, J., Cen, C., and Chen, M. (2012) Molar□ Tooth Structure from the Mesoproterozoic Wumishan Formation in Lingyuan, Yanshan Region, North China, and Geological Implications. Acta Geologica Sinica□ English Edition, 1, 85-95

Hossain, F., Dlugogorski, B., Kennedy, E., Belova, I. and Murch, G. (2011) First-principles study of the electronic, optical and bonding properties in dolomite. Computational Materials Science, 3, 1037-1042

James, N.P., Narbonne, G.M. and Sherman, A.G. (1998) Molar-tooth carbonates: shallow subtidal facies of the Mid- to Late Proterozoic. Journal of Sedimentary Research, 68, 716-722.

Kirkland, E.J. (1998) Advanced computing in electron microscopy. Plenum Press, New York, 250 pp.

Kresse, G. and Furthmüller, J. (1996) Efficiency of ab-initio total energy calculations for metals and semiconductors using a plane-wave basis set. Computational Materials Science, 1, 15-50

Long, D.G. (2007) Tomographic study of Paleoproterozoic carbonates as key to understanding the formation of molar-tooth structure. Gondwana Research, 4, 566-570

Marshall, D. and Anglin, C. (2004) CO_2-clathrate destabilization: a new model of formation for molar tooth structures. Precambrian Research, 3, 325-341.

Meng, X. and Ge, M. (2002) The sedimentary features of Proterozoic microspar (Molar-tooth) carbonates in China and their significance. Episodes-Newsmagazine of the International Union of Geological Sciences, 3, 185-195.

Oganov, A.R., Glass, C.W. and Ono, S. (2006) High-pressure phases of $CaCO_3$: Crystal structure prediction and experiment. Earth and Planetary Science Letters, 1, 95-103

Pennycook, S. (2002) Structure determination through Z-contrast microscopy. Advances in imaging and electron physics, 123, 173-206

Pennycook, S., Rafferty, B. and Nellist, P. (2000) Z-contrast imaging in an aberration-corrected scanning transmission electron microscope. Microscopy and Microanalysis, 04, 343-352.

Perdew, J.P., Burke, K. and Ernzerhof, M. (1996) Generalized gradient approximation made simple. Physical Review Letters, 18, 3865-3868.

Pollock, M.D., Kah, L.C. and Bartley, J.K. (2006) Morphology of molar-tooth structures in Precambrian carbonates: influence of substrate rheology and implications for genesis. Journal of Sedimentary Research, 2, 310-323.

Pratt, B.R. (1998) Molar-tooth structure in Proterozoic carbonate rocks: Origin from synsedimentary earthquakes, and implications for the nature and evolution of basins and marine sediment. Geological Society of America Bulletin, 8, 1028-1045.

Reeder, R.J. (1992) Carbonates: growth and alternation microstructures. In P.B. Buseck, Eds., Minerals and Reactions at the Atomic Scale: Transmission Electron Microscopy, 27, p. 381-424. Reviews in Mineralogy, Mineralogy Society of America, Washington, D.C.

Reksten, K. (1990) Superstructures in calcian ankerite. Physical Chemistry of Minerals, 17, 266-270.

Shen, Z., Konishi, H., Brown, P.E. and Xu, H. (2013) STEM investigation of exsolution lamellae and "*c*" reflections in Ca-rich dolomite from the Platteville Formation, western Wisconsin. American Mineralogist, 4, 760-766.

Sholl, D. and Steckel, J.A. (2011) Density functional theory: a practical introduction Wiley-Interscience.

Stumm, W. and Morgan, J.J. (1995) Aquatic chemistry: chemical equilibria and rates in natural waters. JOHN WILEY & SONS, NEW YORK, NY 10158(USA). 1995.

Van Tendeloo, G., Wenk, H. and Gronsky, R. (1985) Modulated structures in calcian dolomite: A study by electron microscopy. Physics and Chemistry of Minerals, 6, 333-341.

Wang, Y., and Xu, H. (2006) Geochemical chaos: periodic and nonperiodic growth of mixed-layer phyllosilicates. Geochimica et Cosmochimica Acta, 70, 1995-2005.

Wenk, H. and Zhang, F. (1985) Coherent transformations in calcian dolomites. Geology, 7, 457-460.

Wenk, H. and Zenger, D. (1983) Sequential basal faults in Devonian dolomite, Nopah Range, Death Valley area, California. Science, 4623, 502-504.

Wenk, H., Hu, M., Lindsey, T. and Morris Jr, J. (1991) Superstructures in ankerite and calcite. Physics and Chemistry of Minerals, 6, 527-539.

Xu, H., and Veblen, D.R. (1996) Interstratification and other reaction microstructures in the chlorite-berthierine series. Contribution to Mineralogy and Petrology, 124, 291-301.

Xu, H., Zhang, Y., and Veblen, D. R. (1996) Periodic and nonperiodic interstratification in the chlorite-biotite series. American Mineralogist, 81, 1396-1404.

Zhang, F., Xu, H., Konishi, H., and Roden, E.E. (2010) A relationship between d_{104} value and composition in the calcite - disordered dolomite solid solution series. American Mineralogist, 95(11-12), 1650-1656.

Zhang, F., Xu, H., Konishi, H., Shelobolina, E. S., and Roden, E. E. (2012a) Polysaccharide-catalyzed nucleation and growth of disordered dolomite: A potential precursor of sedimentary dolomite. American Mineralogist, 97, 556-567.

Chapter Appendix

The samples used in Chapter 3 and 4 are listed below:

UW Number	Field Number	Sample Type	Description	Location	Figured In
UW 2025/1	PDC-2A	Hand sample	Dolomitized limestone	Prairie du Chien, Wisconsin	Fig. 3.2.1, Fig. 3.2.2
UW 2025/2	HHL-00H	Hand sample	“Molar tooth” dolomite	Hungry Horse, Montana	Fig. 4.2.1, Fig. 4.2.2

This Chapter was previously published (*American Mineralogist*, 99 (2014), 1413-1419) with the following coauthors:

Zhizhang Shen[1], Hiromi Konishi[1], Izabela Szlufarska[2], Philip E. Brown[1], and Huifang Xu[1*]

[1]NASA Astrobiology Institute, Department of Geoscience,

University of Wisconsin - Madison

Madison, Wisconsin 53706

[2]Department of Materials Science and Engineering,

University of Wisconsin-Madison,

Madison, Wisconsin 53706

Chapter 5. Simulation methods

5.1 Density Functional Theory

According to Born-Oppenheimer approximation[1,2], the electrons can be considered as moving in the field of frozen nuclei since the nuclei are much heavier and move much slower than electrons. When calculating the total energy of a system, only the movement and energies of electrons needs to be determined quantum mechanically. The time-independent, non-relativistic electronic Schrödinger equation can be expressed as:

$$H_{elec}\psi = E\psi, \tag{5.1.1}$$

where $$H_{elec} = -\frac{1}{2}\sum_{i=1}^{N}\nabla_i^2 + \sum_{i=1}^{N}V(r_i) + \sum_{i=1}^{N}\sum_{j<i}U(r_i, r_j). \tag{5.1.2}$$

From the above equations, we can see that the electronic Hamiltonian is composed of three parts: the kinetic energy of electrons, the interaction energy between electrons and the collection of nuclei, and the potential between electrons.

The density functional theory (DFT) is based on two fundamental theorems of Hohenberg-Kohn[3]:

1) The ground-state energy from Schrödinger's equation is a unique functional of the electron density.
2) The electron density that minimizes the energy of the overall functional is the true electron density corresponding to the full solution of the Schrödinger equation.

The electron density at a position **r** is related to the individual electron wave functions:

$$n(\boldsymbol{r}) = 2\sum_i \psi_i^*(\boldsymbol{r})\,\psi_i(\boldsymbol{r}). \tag{5.1.3}$$

The energy functional now can be written as

$$E[n(\boldsymbol{r})] = T[n(\boldsymbol{r})] + \int V(\boldsymbol{r})n(\boldsymbol{r})\,d^3r + \frac{e^2}{2}\iint \frac{n(r)n(r')}{|r-r'|}\,d^3r d^3r' + E_{xc}[n(\boldsymbol{r})]. \tag{5.1.4}$$

The four terms on the right-hand side of Eq. (5.1.4) represent the kinetic energies of electrons, the interactions between electrons and nuclei and between electrons, and the exchange-correlation functional.

In DFT, Kohn-Sham equations[4], which is a set of single-electron equations, are utilized to solve for electron density:

$$\left[-\frac{h^2}{2m}\nabla^2 + V(\boldsymbol{r}) + V_H(\boldsymbol{r}) + V_{xc}(\boldsymbol{r})\right]\psi_i(\boldsymbol{r}) = \varepsilon_i\psi_i(\boldsymbol{r}), \tag{5.1.5}$$

where $V_H(\boldsymbol{r})$ is called the Hartree potential, describing the interaction between one electron and the total electron density. Since each electron contributes to the electron density, the Hartree potential includes a self-interaction. The correction for this is taken into account in the exchange and correlation term. In practice, the iteration method is used to solve Kohn-Sham equations[5], which is done as follows. First, using an initial guess for electron density, calculate the wave function $\psi_i(\boldsymbol{r})$ according to Kohn-sham equations. Next, update the electron density using equation 5.1.3. If the updated electron density is the same as the electron density from the initial trial, then it is the ground-state electron density; otherwise, go back to step 1 and follow the same procedures until the two electron densities are within some prescribed uncertainty.

The exchange-correlation functional (the fourth term in Eq. 5.1.5) accounts for two parts of non-classical interactions: exchange interaction and correlation interaction. The exchange interaction is a direct consequence of Pauli exclusion principle; and the Coulomb correlation interaction prevents the electrons from coming too close to each other[4]. One method to approximate the exchange-correlation functional is called local density approximation (LDA). In this method, the functional is derived from homogeneous electron gas:

$$E_{xc}^{LDA} = \int n\varepsilon^{HEG}(n)d\boldsymbol{r}. \tag{5.1.6}$$

The functional form of exchange-correlation energy density for uniform electron gas $\varepsilon^{HEG}(n)$ can be very accurately determined by quantum Monte Carlo calculations. Another approximation to the exchange-correlation term is known as non-empirical generalized gradient approximation (GGA)[6,7], which takes into account the local gradient in the electron density:

$$E_{xc}^{GGA} = \int n\varepsilon(n, \nabla n) d\boldsymbol{r}. \tag{5.1.7}$$

In this study, we used GGA approximation with the Perdew, Burke and Ernzerhof (PBE) paramters[6]. And we employed the Vienna ab initio simulation package (VASP)[8] to perform the DFT calculations.

5.2 Molecular Dynamics

5.2.1 Basics of Molecular Dynamics Simulations

In molecular dynamics (MD) simulations, the movements of atoms are determined by Newton's law of motion where the force (F_i) applied on an atom i is equal to the mass of this atom (m_i) multiplied by the acceleration ($\frac{\partial^2 r_i}{\partial t^2}$, r_i is the position of this atom at time t):

$$m_i \frac{\partial^2 r_i}{\partial t^2} = F_i. \tag{5.2.1}$$

The force between two atoms can be calculated from potential energy (U_{ij}) between them, $F_{ij} = \nabla_i U_{ij}(r_{ij})$ (5.2.2), which in turn can be calculated using quantum mechanics or classical methods. In classical MD simulations, $U_{ij}(r_{ij})$ represents a force field with parameters fitted to empirical data and to more accurate ab initio calculations.

In this study, equations of motion are integrated using the Verlet algorithm[9]. In this algorithm, the position of an atom can be approximated by Taylor expansion:

$$r\ (t+\Delta t) = r(t) + v(t)\Delta t + \frac{f}{2m}\Delta t^2 + O(3). \qquad (5.2.3)$$

$$r\ (t-\Delta t) = r(t) - v(t)\Delta t + \frac{f}{2m}\Delta t^2 - O(3). \qquad (5.2.4)$$

where $r\ (t+\Delta t)$ and $r\ (t-\Delta t)$ are positions of this atom at the next step and previous timesteps, respectively.

By combining the two equations, we obtain:

$$r(t\ +\ \Delta t\ ) = 2r(t) - r(t-\Delta t) + \frac{f}{m}\ \Delta t^2. \qquad (5.2.5)$$

Similarly, by subtracting equation 5.2.3 from equation 5.2.4, we find:

$$v(t) = \frac{r\ (t+\Delta t) - r\ (t-\Delta t)}{2\Delta t}. \qquad (5.2.6)$$

As shown above, velocities and positions of atoms can be calculated from MD simulations. Thermodynamic properties of the simulated system, such as temperature, pressure, internal energy, diffusion coefficient, etc., can also be calculated since they can be described as a function of velocities and positions.

5.2.2 Force Fields

A force field (U_{ij} in Eq. 5.2.2.) refers to a set of parameters of mathematical functions used to describe the potential energy of a system of particles. The potential energy of a system includes the interactions between all atoms. Usually force field functions consist of bonded terms describing the covalent bonds between atoms and non-bonded terms. Bonded terms (referred as intra-molecular interactions in DL_POLY code) include potential functions representing chemical bonds, valence angles and dihedral angels:

$$U_{bonded} = U_{bond} + U_{angle} + U_{dihed}. \qquad (5.2.7)$$

Morse potential[10] is used to describe the carbon-oxygen bond in the CO_3^{2-} group of dolomite.

$$U(r) = E_0\left[\left\{1 - \exp\left(-k(r - r_0)\right)\right\}^2 - 1\right], \tag{5.2.8}$$

where E_0 is the depth of the potential well, r_0 is the equilibrium bond length, and k determines the width of the well. In Pavese's carbonate model[11], which we use for describing dolomite, Coulomb interactions between bonded atoms are also evaluated. A simple harmonic form is used for covalent bonds in monosaccharide models:

$$U(r) = \frac{1}{2}\,k(r_{ij} - r_0)^2. \tag{5.2.9}$$

The valence angle potentials in the CO_3^{2-} group of dolomite and sugar used the same harmonic form:

$$U(\theta) = \frac{1}{2}\,k(\theta - \theta_0)^2. \tag{5.2.10}$$

where $(\theta - \theta_0)$ is the deviation from the equilibrium angle (in CO_3^{2-} group, θ_0 is 120° for ∠ O-C-O).

The unbounded or inter-molecular interactions describe the long-range electrostatic and van der Waals forces. Buckingham potentials[12] (equation 5.2.11) and Lennard-Jones potentials[13] (equation 5.2.12) are used for van der Waals forces in our study:

$$U(r) = A\exp\left(-\frac{r}{\rho}\right) - \frac{C}{r^6}. \tag{5.2.11}$$

The first term in Eq. 5.2.11 describes the repulsive interactions, while the second term describes the attractive van der Waals forces.

$$U(r) = 4\varepsilon\,[\left(\frac{\sigma}{r}\right)^{12} - (\frac{\sigma}{r})^6], \tag{5.2.12}$$

where ε is the depth of the potential well and σ is the finite distance where the potential between two atoms is zero.

Force fields for $CaCO_3$, which include a core-shell model to account for the electronic polarizability of oxygen atoms in CO_3^{2-} group, were developed by Pavese et al. (1996)[11]. Force fields for $MgCO_3$ were developed by de Leeuw and Parker, 2000[14]. However, a recent work has shown that a rigid-ion model of calcite can provide a better description of the interfacial (calcite-water) water structure than the polarizable model[15]. In this rigid-ion version of the calcite, the shells are removed and the oxygen charge is the sum of the core and shell, while all other parameters remain the same as the Pavese model[11]. We followed the same method to construct a rigid-ion force field for dolomite. Details of the force field parameters can be found in the chapter appendix.

Glycam_06h[16] and TIP3P[17] potential models are used for monosaccharides and water. The parameters of monosaccharides, water and the interactions between them were obtained form DL_FIELD_3.1[18]. For dolomite-water interactions, we used the following parameters: the calcium-water oxygen/magnesium-water oxygen potential from de Leeuw and Parker (2000)[14], and the carbon-water oxygen potential from Kerisit et al. (2003)[19].

Because of the large charge disparity between dolomite and carbohydrates, it is crucial to refit existing potentials for interactions between dolomite and sugar atoms[20]. More specifically, there are strong Coulomb interactions between calcium and sugar oxygen, and between magnesium and sugar oxygen, it is important to refit these two potentials. We used a fitting procedure described by Schröder[21]. The main idea of this method is to force the repulsive term of the potential to be consistent with the reduced Coulomb interactions between Ca/Mg and Osugar (compared to the interactions between

Ca/Mg and Ocarbonate). The fitting procedure consists of two steps. First, obtain new charges for atoms A and B in a new system (here, a new dolomite structure) but maintain the Coulomb interaction between $A_{mineral}$ and B_{sugar} according to the following equations:

$$\alpha_A q_{Bnew}^2 = q_{Amineral} q_{Bsugar} \tag{5.2.13}$$

$$q_{Anew} = \alpha_A q_{Bnew} \tag{5.2.14}$$

$$\alpha_A = \frac{q_{Amineral}}{q_{Bmineral}} \tag{5.2.15}$$

The second step is to refit the repulsive term of the potentials (Buckingham potentials in the case of dolomite) by using the new charges to maintain the crystal structure of the new system. We fitted the A parameters in Buckingham potentials for Ca-O_{sugar} and Mg-O_{sugar} interactions together to the dolomite lattice parameters. The Buckingham potential can be expressed as: $U(r) = Aexp\left(-\frac{r}{\rho}\right) - \frac{C}{r^6}$, where A and ρ are related to the number of electrons and the electron density, respectively. The first term describes the short-range repulsive interactions, while the second term describes the attractions by van der Waals forces. The optimal combination of 1000 eV and 650 eV for respective A parameters was obtained. The Coulomb interactions between other non-bonded atoms are usually very weak compared to the interactions between Ca^{2+}/Mg^{2+} and O_{sugar} and the parameters for these cross-terms from previous work[20] were used in our study. In order to validate the fitting parameters, the most stable configuration of mannose on dolomite (104) surface from MD simulations at 10K was relaxed in ab initio calculations using the density functional theory (DFT) as implemented in VASP[8]. Details of VASP calculations can be found in the chapter appendix. The center of mass of mannose in classical MD simulations was found to be closer to the surface by 0.3Å as compared to the DFT results, which provides a reasonable agreement. The bond lengths of Ca-O and Mg-O in MD simulations were found to be 2.41Å and 2.04Å while the corresponding values from VASP are 2.48 Å and 2.28 Å. Although there are some quantitative differences between the values obtained with classical force fields and DFT, these differences are relatively small and the qualitative trends in bonding are in agreement between the two approaches. In addition, the overall structure and orientation of mannose are similar in both MD and DFT simulations.

5.2.3 Potential of Mean Force (PMF)

Potential of mean force (PMF) is a method used to study how the free energy of system changes as a function of a specific reaction coordinate[22]. The PMF is related to the probability distribution P(x):

$$A(x) = -k_B T \ln P(x), \tag{5.2.16}$$

where $A(x)$ is the PMF along coordinate x, k_B is the Boltzmann constant, and T is temperature. The probability distribution function along the coordinate x can be expressed as:

$$P(x) = \int e^{-U(\mathbf{R})/k_B T} \delta\left(x'(\boldsymbol{R}) - x\right) d\boldsymbol{R}, \tag{5.2.17}$$

where $U(\mathbf{R})$ is the total internal energy of the system as a function of the coordinate $\boldsymbol{R}$, and $x'(\boldsymbol{R})$ is a function of the Cartesian coordinates of the system, such as a distance that we used in our study. In order to effectively sample the configurational space where there are large energy barriers along reaction coordinate within finite computer time, a technique called umbrella sampling[23,24] is widely used. In this approach, sampling around a chosen reaction coordinate value (window i) were simulated with a harmonic spring potential:

$$U_i'(x) = \frac{1}{2}K(x - x_i), \tag{5.2.18}$$

where K is the spring constant.

The unbiased PMF at window i can be written as:

$$A_i(x) = -k_B T \ln P_i'(x) - U_i'(x) + F_i, \tag{5.2.19}$$

where $P_i'(x)$ is the biased probability and F_i is a constant to be determined. A method to solve for the optimal values of F_i is known as weighted histogram analysis method[25] (WHAM). The F_i value can be determined by iteration to self-consistency from the following two equations:

$$P(x) = \frac{\sum_{i=1}^{N} n_i(x)}{\sum_{i=1}^{N} \exp([F_i - U_{bias,i}(x)]/k_B T)} \tag{5.2.20}$$

$$F_i = -k_B T ln\{\sum_{Xbins} P(x) \exp[-U_{bias,i}(x)]/k_B T\}, \tag{5.2.21}$$

where N is number of simulations, n_i is number of counts in the i^th histogram bin, and $U_{bias,i}(x)$ is biasing potential.

References

(1) Born, M.; Oppenheimer, R. Zur Quantentheorie Der Molekeln. *Ann. Phys.* **1927**, *20*, 457–484.

(2) Wolfram, K.; Holthausen, M. C. *A Chemist's Guide to Density Functional Theory*; second edi.; Wiley-VCH Verlag: Weinheim, Germany, 2001; pp. 1–92.

(3) Hohenberg, P.; Kohn, W. Inhomogeneous Electron Gas. *Phys. Rev.* **1964**, *136*, B864–B871.

(4) Kohn, W.; Sham, L. J. Self-Consistent Equations Including Exchange and Correlation Effects. *Phys. Rev.* **1965**, *140*, A1133–A1138.

(5) Sholl, D. S.; Steckel, J. A. *Density Functional Theory: A Practical Introduction*; John Wiley & Sons, Inc.: Hoboken, New Jersey, 2009; pp. 1–33.

(6) Perdew, J.; Burke, K.; Ernzerhof, M. Generalized Gradient Approximation Made Simple. *Phys. Rev. Lett.* **1996**, *77*, 3865–3868.

(7) Perdew, J. P.; Burke, K.; Wang, Y. Generalized Gradient Approximation for the Exchange-Correlation Hole of a Many-Electron System. *Phys. Rev. B* **1996**, *54*, 533–539.

(8) Kresse, G.; Furthmüller, J. Efficient Iterative Schemes for Ab Initio Total-Energy Calculations Using a Plane-Wave Basis Set. *Phys. Rev. B. Condens. Matter* **1996**, *54*, 11169–11186.

(9) Verlet, L. Computer “Experiments” on Classical Fluids. I. Thermodynamical Properties of Lennard-Jones Molecules. *Phys. Rev.* **1967**, *159*, 98–103.

(10) Morse, P. M. Diatomic Molecules according to the Wave Mechanics. II. Vibrational Levels. *Phys. Rev.* **1929**, *34*, 57–64.

(11) Pavese, A.; Catti, M.; Parker, S. C.; Wall, A. Modelling of the Thermal Dependence of Structural and Elastic Properties of Calcite , CaCO 3. *Phys. Chem. Miner.* **1996**, *23*, 89–93.

(12) Buckingham, R. A. The Classical Equation of State of Gaseous Helium , Neon and Argon. *Proc. R. Soc. Lond. A. Math. Phys. Sci.* **1938**, *168*, 264–283.

(13) Jones, J. E. On the Determination of Molecular Fields. II . From the Equation of State of a Gas. *Proc. R. Soc. Lond. A. Math. Phys. Sci.* **1924**, *106*, 463–477.

(14) De Leeuw, N. H.; Parker, S. C. Modeling Absorption and Segregation of Magnesium and Cadmium Ions to Calcite Surfaces: Introducing MgCO[sub 3] and CdCO[sub 3] Potential Models. *J. Chem. Phys.* **2000**, *112*, 4326.

(15) Fenter, P.; Kerisit, S.; Raiteri, P.; Gale, J. D. Is the Calcite − Water Interface Understood ? Direct Comparisons of Molecular Dynamics Simulations with Specular X - Ray Reflectivity Data. *J. Phys. Chem. c* **2013**, *117*, 5028–5042.

(16) Kirschner, K. N.; Yongye, A. B.; Tschampel, S. M.; Gonza, J.; Daniels, C. R.; Foley, B. L.; Woods, R. J. GLYCAM06 : A Generalizable Biomolecular Force Field. Carbohydrates. *J. Comput. Chem.* **2007**, *29*, 622–655.

(17) Jorgensen, W. L.; Chandrasekhar, J.; Madura, J. D.; Impey, R. W.; Klein, M. L. Comparison of Simple Potential Functions for Simulating Liquid Water. *J. Chem. Phys.* **1983**, *79*, 926.

(18) Yong, C. W. A Force Field and Model Development Tool for DL_POLY. In *CSE frontier, STFC Computational Science and Engineering*; Blake, R., Ed.; Darebury Laboratory, 2010; pp. 38–40.

(19) Kerisit, S.; Parker, S. C.; Harding, J. H. Atomistic Simulation of the Dissociative Adsorption of Water on Calcite Surfaces. *J. Phys. Chem. B* **2003**, *107*, 7676–7682.

(20) Freeman, C. L.; Harding, J. H.; Cooke, D. J.; Elliott, J. a.; Lardge, J. S.; Duffy, D. M. New Forcefields for Modeling Biomineralization Processes. *J. Phys. Chem. C* **2007**, *111*, 11943–11951.

(21) Schröder, K.; Sauer, J.; Leslie, M.; Catlow, C. R. A.; Thomas, J. M. Bridging Hydroxyl Groups in Zeolitic Catalysts : A Computer Simulation of Their Structure , Vibrational Properties and Acidity in Protonated Faujasites (H-Y Zeolites). *Chem. Phys. Lett.* **1992**, *188*, 320–325.

(22) Kirkwood, J. G. Statistical Mechanics of Fluid Mixtures. *J. Chem. Phys.* **1935**, *3*, 300.

(23) Torrie, G. M.; Valleau, J. P. Monte Carlo Free Energy Estimates Using Non-Boltzmann Sampling: Application to the Sub-Critical Lennard-Jones Fluid. *Chem. Phys. Lett.* **1974**, *28*, 578–581.

(24) Valleau, J. P.; Torrie, G. M. A Guide for Monte Carlo for Statistical Mechanics. In *Statistical Mechanics, Part A*; Berne, B. J., Ed.; Plenum Press: New York, 1977; pp. 169–194.

(25) Kumar, S.; Bouzida, D.; Swedsen, R. H.; Kollman, P. A.; Rosenbergl, J. M. The Weighted Histogram Analysis Method for Free-Energy Calculations on Biomolecules. I. The Method. *J. Comput. Chem.* **1992**, *13*, 1011–1021.

Chapter appendix

1. Potential parameters used for Dolomite

Ion	Symbol	Charge/au
Calcium	Ca	2.0
Magnesium	Mg	2.0
Carbon	C	1.135
Oxygen	O	-1.045

Morse Potential $E_0\left[\left\{1-\exp\left(-k(r-r_0)\right)\right\}^2-1\right]$			
Ion Pair	E_0/eV	r_0/Å	k/ Å $^{-1}$
C---O	4.71	1.18	3.8

Three Body Potential $\frac{k}{2}(\theta-\theta_0)^2$		
Atoms	k/eV	θ_0/°
O---C---O	1.69	120.0

Buckingham Potential $Aexp\left(-\frac{r}{\rho}\right)-\frac{C}{r^6}$			
Ion Pair	A/eV	ρ/Å	C/eV Å^6
Ca---O	1550.0	0.29700	0.0
Mg---O	1092.2	0.27926	0.0
O---O	16372.0	0.21300	3.47

Potential parameters used for Water

Ion	Symbol	Charge/au
Oxygen	O_w	-0.834
Hydrogen	H	0.417

Lennard-Jones Potential $\left(\frac{A}{r^{12}}\right)-\left(\frac{B}{r^6}\right)$		
Ion pair	A/eV Å^{12}	B/ eV Å^6
O_w --- O_w	25234.47	25.7934

Cross terms used for Dolomite/Water interaction

Buckingham Potential $Aexp\left(-\frac{r}{\rho}\right)-\frac{C}{r^6}$			
Ion Pair	A/eV	ρ/Å	C/eV Å^6
Ca---O_w	1186.6	0.29700	0.0
Mg---O_w	2290.0	0.22000	0.0
C---O_w	435	0.34000	0.0

Lennard-Jones Potential $4\varepsilon\ [\left(\frac{\sigma}{r}\right)^{12} - (\frac{\sigma}{r})^{6}]$		
Ion pair	ε/eV Å^{12}	σ/ eV Å^{6}
O_w---O_w	0.0066	3.1507

Cross terms used for Dolomite/Sugar interaction

Buckingham Potential $Aexp\left(-\frac{r}{\rho}\right) - \frac{C}{r^6}$			
Ion Pair	A/eV	ρ/Å	C/eV Å^{6}
Ca---G_Oh	1000.0	0.29700	0.0
Mg---G_Oh	650.0	0.22000	0.0
Ca---G_Os	720.0	0.22000	0.0
Mg---G_Os	470.0	0.22000	0.0

Lennard-Jones Potential $\left(\frac{A}{r^{12}}\right) - (\frac{B}{r^{6}})$		
Ion pair	A/eV Å^{12}	B/ eV Å^{6}
O---G_Oh	15357.080	11.571
O---G_Cg	19942.854	11.198
C---G_Oh	34339.488	30.068
C---G_Cg	45251.855	29.310

Cross terms used for Water/Sugar interaction

Lennard-Jones Potential $\left(\frac{A}{r^{12}}\right) - (\frac{B}{r^{6}})$		
Ion pair	A/eV Å^{12}	B/ eV Å^{6}
O_w---G_Oh	25259.440	27.99135
O_w ---G_Ho	9.907453	0.3406527
O_w ---G_Cg	34078.550	27.60867
O_w ---H2	1401.643	3.446229
O_w ---H1	2062.903	4.180853
O_w ---G_Os	19957.91	23.58958

2. The DFT calculation details of the mannose adsorption on the dolomite (104) surface

We use DFT as implemented in the Vienna *ab initio* simulation package (VASP).[8] The general gradient approximation (GGA) with the Perdew, Burke, and Ernzerhof (PBE) parameters is employed.[6] The projector-augmented wave (PAW) method with the energy cutoff of 600 eV has been used. A 3×3×1 k-points was utilized. We used a four-layer slab of dolomite with two (104) surfaces. A vacuum layer of ~18 Å was added to separate the top and bottom surfaces. The atoms in the bottom three layers of dolomite were fixed while the atoms in the top layer were allowed to relax to interaction with the mannose molecule. The initial relative positions of mannose atoms to the surface atoms were taken from the output of MD simulations.

Chapter 6. Modeling the Effect of Hydrogen Sulfide in Dolomite Growth

6.1 Introduction

Dolomite ($CaMg(CO_3)_2$), which used to be ubiquitous in the geological past, is rarely found in Holocene sediments.[1] Its rare occurrence in the modern sediments defies the geological notion that the present is the key to the past. This contradiction is at the heart of the famous “dolomite problem”. Attempts to synthesize dolomite inorganically under ambient environment (low temperature, <50˚C) have been largely unsuccessful[2], although a recent study[3] indicates that natural dolomitization could happen at as low as 40˚C. It is now generally accepted that the dolomite problem lies in the high kinetic barrier caused by the magnesium hydration at low temperature that hinders dolomite formation.[4-5]

Based on the observations that modern dolomite formations are usually associated with environments where anaerobic microorganisms, including sulfate-reducing bacteria, are active[6-12], microorganisms are believed to help overcome the kinetic barrier and to promote dolomite formation. It was proposed that sulfate reducing bacteria are related to dolomite crystallization in nature[7], and high-Mg calcite and Ca-rich disordered dolomite have been synthesized at low temperature under laboratory conditions with sulfate reducing bacteria[7,9]. In addition, a recent work showed that dissolved hydrogen sulfide, as a product of bacterial sulfate reduction, is an eligible catalyst for dolomite crystallization[13,14]. The amount of $MgCO_3$ in the precipitating Ca-Mg-carbonate increases as concentration of the dissolved sulfide increases.[14] The dissolved hydrogen sulfide may take the role of a catalyst for enhancing Mg incorporation into the structure and crystallization of dolomite.

Despite these advances, the mechanism of how dissolved hydrogen sulfide, or catalysts in general help overcome the kinetic barrier is uncertain. The dolomite growth involves two important steps: First, hydrated Mg^{2+} ions from the solution are adsorbed onto the dolomite surface and then the surface hydrated Mg^{2+} ions attract CO_3^{2-} ions from the solution (Figure 6.2.1). The positive role of catalysts in the first step has been supported by the evidence that disordered dolomite has been synthesized at low temperature by using carboxymethyl cellulous (CMC) with carboxyl functional groups[15], which can dewater and complex with Mg ions forming a $[Mg(H_2O)_5(R\text{-}COO)^+]$ complex.[16,17] It was proposed that the Mg-carboxyl complex may the change coordination environment of Mg[16] and requires much lower energy (56.9 kJ/mol) for carbonation than $Mg(H_2O)_6^{2+}$.[18] However, HS^- has been shown to neither have much effect on lowering the Mg^{2+} dehydration barrier in the aqueous Mg^{2+}-water complex nor interact with the remaining five water molecules in the first solvation shell of Mg^{2+}.[19] The adsorption of magnesium onto a growing calcite crystal from the solution is energetically favorable according to a previous simulation study.[20] Lippmann also argues that there is no significant energy barrier for Mg^{2+} to be adsorbed onto the surface, and there is no need for Mg^{2+} to be entirely dehydrated in order for it to be adsorbed.[4] The author further points out that the second step in the dolomite growth is rate controlling, which means that the retained water molecules adhered to surface Mg^{2+} block the CO_3^{2-} ions in the solution from being sufficiently attracted by surface Mg^{2+} ions.[4] Therefore, the key role of dissolved sulfide in promoting dolomite formation is very likely to lie in the dehydration of Mg^{2+} ions at the (proto)dolomite or other precursor surface. However, the effect of hydrogen sulfide on this process has never been explored. A hint may come from a related work on calcite. Specifically, atomic force microscopy (AFM) work and molecular dynamic (MD) simulations have shown that ethanol and polysaccharides can be more strongly bound to the calcite surface than water, thus repelling the water molecules from the surface and forming a hydrophobic layer.[21-23] Meanwhile, ethanol and polysaccharides have been proven to enhance Mg^{2+} incorporation into precipitating Ca-Mg carbonate.[15,24] For the dolomite case, one explanation is that the surface water molecules can be removed by adsorbed hydrogen sulfides on the dolomite surface. In order to study the thermodynamics of the adsorption processes, we performed quantum-mechanical calculations based on the density functional theory (DFT).

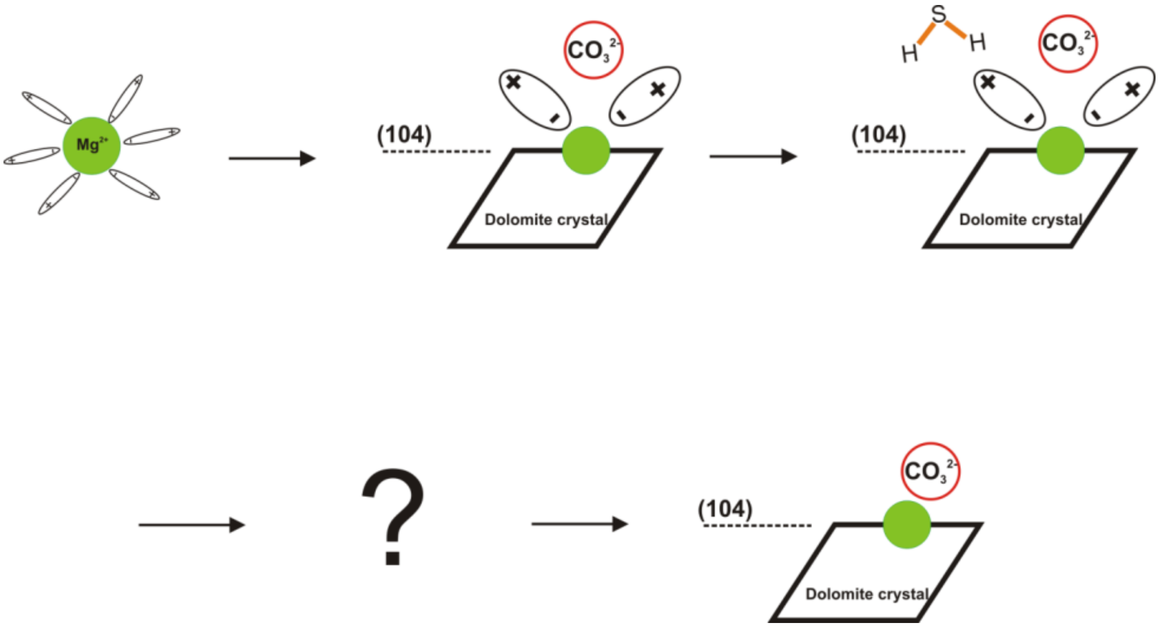

Figure 6.2.1 The proposed processes for the growth of dolomite crystal catalyzed by dissolved hydrogen sulfide. First, partially dehydrated Mg^{2+} ions are adsorbed onto the dolomite surface. The remaining water bonds to surface Mg^{2+} ions and blocks the approach of carbonate group to the Mg^{2+} ions which is enabled by the presence of H_2S.

6.2. Methods

6.2.1 Computational details

We use DFT as implemented in the Vienna *ab initio* simulation package (VASP).[25] The general gradient approximation (GGA) with the Perdew, Burke, and Ernzerhof (PBE) parameters is employed.[26] The projector-augmented wave (PAW) method with the energy cutoff of 600 eV has been used. All structures are relaxed using both the static energy minimization scheme and *ab initio* molecular dynamics simulations at 10K. First, we determine energies of adsorption of a monolayer of either water or H_2S onto the dolomite {104} surface, which is the main cleavage and growth plane of dolomite. Both vacuum and solution are considered as reference states for adsorption calculations. The pH of modern seawater and pore water in modern dolomite sediments is usually 7~8.2[8, 27-29] with some exceptions in modern lacustrine environments where pH of lake water and pore water are higher than 9 [29]. There are two major species of dissolved sulfide: HS^- and H_2S. When pH is between 7 and 8, aqueous H_2S accounts for 10~50% of total dissolved sulfides.[30] When pH is greater than 8, the surface charge of dolomite is negative at $pCO_2 = 10^{-3.5}$ atm.[31] As a result, it is most likely that it is H_2S that is concentrated on the dolomite surface at this pH condition, although HS^- is the dominant solution species. To consider the two pH ranges, calculations were performed for H_2S instead of HS^-. Dolomite {104} surfaces have been simulated using 4 layer slabs of a triclinic unit cell (Figure 6.2.1) that has the following parameters: a=9.085Å; b=4.812Å; c=4.812Å;

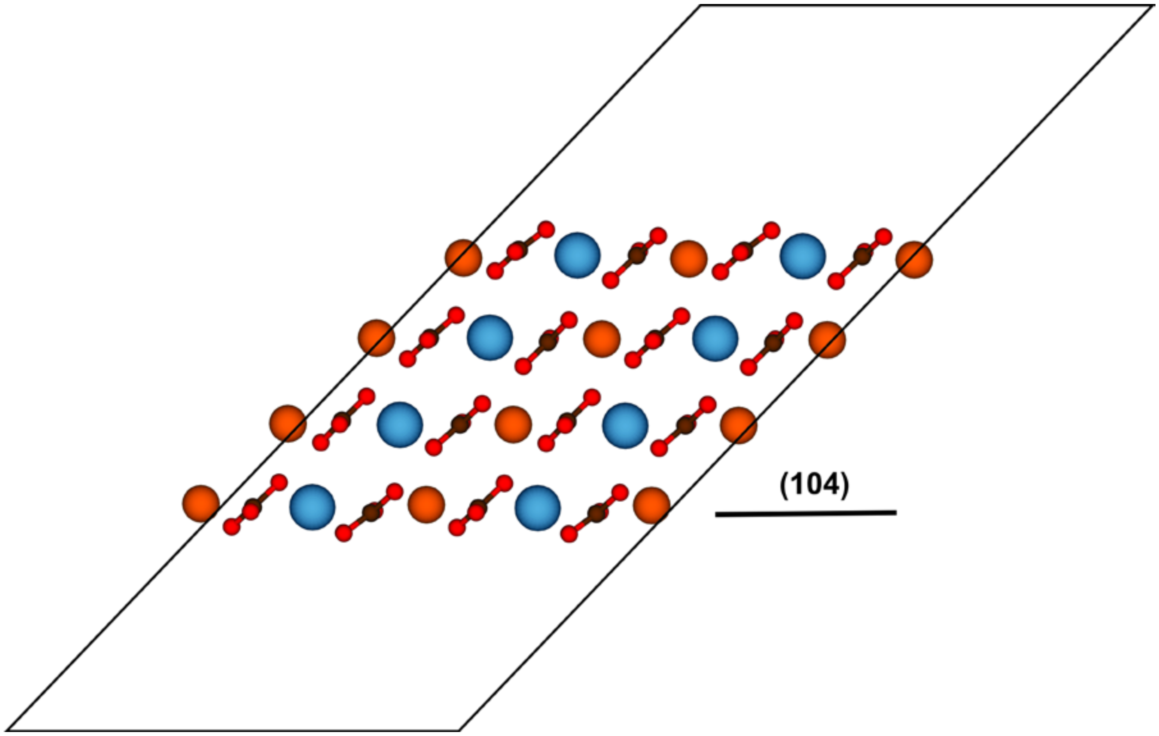

Figure 6.2.1. A four-layer slab model of dolomite with (104) surfaces were used in this study (view of 2×2×1 supercell). The O, Mg, Ca and C atoms are displayed as red, orange, cyan, and brown, respectively.

α=120.00˚; β=37.40˚; γ=120.00˚. The top and the bottom free surfaces have identical structures and periodic boundary conditions are used in all spatial directions. For a monolayer of either water or H_2S adsorption on the surface, a vacuum of ~14-Å thickness has been inserted above one of the surfaces in order to prevent the interactions between the bottom surface and the water or H_2S molecules adsorbed to the top surface. The bottom layer of the dolomite surface (10 atoms) is fixed for the calculations of adsorption in vacuum. Calculations for cases where both surfaces have an adsorbed monolayer were also performed and the adsorption energies per surface unit cell are the same as one surface adsorption case. To simulate the adsorption in a solution environment, a bulk water space of 14Å with density of ~1 g/cm^3 was inserted above the surface with an adsorbed monolayer. All layers of the dolomite slab are allowed to relax in solution calculations. To ensure a minimum energy configuration of the water surrounding the dolomite, we took multiple samples of water structures generated from classical MD simulations using the code LAMMPS[32] and TIP4P potential[33]. Two small volumes of water corresponding to 20 water molecules were taken from the previous structures. We ensured the densities of the two water structures and relaxed them again in DFT. In order to account for the weak van der Waals interactions in the adsorptions systems, for adsorptions in solution we performed calculations using the DFT-D2 method of Grimme[34]. We tested k-point convergence with a criterion of 1 meV/atom and a mesh of 3×3×1 was used for both vacuum and solution systems.

6.2.2 Thermodynamic model

To test whether aqueous H_2S molecules are more strongly adsorbed to the dolomite {104} surface than water we compare the energies of the initial and final steps in the following reaction. Initially, a monolayer of water molecules with 100% coverage (one water molecule above each cation) is adsorbed on the dolomite {104} surface with the H_2S molecules far away from the surface in the solution. To present the end of the reaction, a monolayer of H_2S molecules with 100% coverage was put on the surface replacing the surface water molecules. The free energy of this reaction at room temperature can be expressed as

$$\Delta G_{ads} = \left[\Delta G_{dol+H_2S}(T) - \Delta G_{dol+H_2O}(T)\right] - [\mu_{H_2S}(T) - \mu_{H_2O}(T)], \tag{1}$$

where $\Delta G_{dol+H_2S}(T)$ and $\Delta G_{dol+H_2O}(T)$, respectively, are the Helmholtz free energy of H_2S and H_2O monolayers adsorbed to dolomite at room temperature (either in vacuum or in solution as described in the previous section); $\mu_{H_2S}(T)$ and $\mu_{H_2O}(T)$ are chemical potentials of an aqueous H_2S molecule and a liquid water molecule at room temperature, respectively. If $\Delta G_{ads} < 0$, then adsorption of H_2S is more energetically favorable than adsorption of water and vice versa. The energy of adsorption system at room temperature for any of our systems is composed of three parts: the DFT energy calculated at 0K, the zero point energy (ZPE), and the thermal energy of vibration. For ZPE, only the vibrational energies of the surface adsorbed atoms are relevant for our study. Our tests show that the major contributions to the vibrational energy are from the molecules of the first four layers above the surface. The free energy of each adsorption system can be expressed as:

$$\Delta G_{dol+H_2S}(T) = E_{dol+adsb,vasp} + \sum_i \frac{1}{2} h\nu_i + RT \sum_i \ln(1 - e^{-h\nu_i/k_B T}) \qquad (2)$$

The first two terms on the right hand side of Eq (1) can be approximated as:

$$\Delta G_{dol+H_2S} - \Delta G_{dol+H_2O} = E_{dol+H_2S,vasp} - E_{dol+H_2O,vasp} + (G^{vib}_{surf+H_2S} - G^{vib}_{surf+H_2O}) \quad (3)$$

Chemical potentials of a liquid water molecule and an aqueous H_2S at room temperature can be calculated as

$$\begin{aligned}\mu^{liquid}_{H_2O}(T) &= E^{molecule}_{H_2O} + \Delta G^{exciations}_{H_2O}(T) - \Delta G^{vaporization}_{H_2O}(T) \\ &= E^{molecule}_{H_2O} - 1.06\ kJ/mol \qquad (4)\end{aligned}$$

$$\begin{aligned}\mu^{aq}_{H_2S}(T) &= E^{molecule}_{H_2S} + \Delta G^{exciations}_{H_2S}(T) - \Delta G^{solvation}_{H_2S}(T) \\ &= E^{molecule}_{H_2S} - 5.76\ kJ/mol \qquad (5)\end{aligned}$$

The general equation for excitation energy is as below[34-35]:

$$\Delta G^{excitations}(T) = -RT \ln\left\{\left[\frac{2\pi(\sum_i m_i)k_B T}{h^2}\right]^{\frac{3}{2}} \frac{V_e}{N}\right\} - RT \ln\left[\frac{\pi^{\frac{1}{2}}}{\sigma}\left(\frac{T^3}{\theta_A\theta_B\theta_C}\right)^{\frac{1}{2}}\right] + RT \sum_i^3 \left[\frac{h\nu_i}{2k_B T} + \ln\left(1 - e^{-h\nu_i/k_B T}\right)\right]$$

(6)

where σ is symmetry number (=2 for water and H_2S molecules), θ is rotational temperature and v_i is vibrational frequency with the *i*th normal mode. The three terms at the right hand side describe the translational, rotational and vibrational contributions to excitation energy respectively. ZPE is included in the third term. The parameters for a water molecule have been described by McQuarrie et al. and Pinney et al.[35,36], and the parameters for H_2S in Senekowitsch and co-workers[37] and Hoffman and co-workers[38]. The vaporization energy and solvation energy are taken from the difference of free energy between gaseous water and liquid water and between gaseous H_2S and aqueous H_2S at 298.15K, 1 atm, standard states.[39] The energy of a single H_2O and a H_2S molecule at 0 K were calculated in VASP in a 10×10×10 Å supercell and a 15×15×15 Å supercell, respectively. By combining Eqs. (1) to (4), we obtain

$$\Delta G_{ads} = \{(E_{dol+H_2S,vasp} - E_{dol+H_2O,vasp)} + \left(G_{surf+H_2S} - G_{surf+H_2O}\right)\} - \{\left(E_{H_2S}^{molecule} - E_{H_2O}^{molecule}\right) + \left(\Delta G_{H_2S}^{exciations} - \Delta G_{H_2O}^{exciations}\right) + (\Delta G_{H_2S}^{solvation} - \Delta G_{H_2O}^{vaporization})\} \qquad (7)$$

The adsorption energy of a mixed layer of H_2O and H_2S from solution can expressed as

$$\Delta G = E_b^{H_2S} \bullet n_{H_2S} + E_b^{H_2O} \bullet n_{H_2O} - TS_{config}\left(n_{H_2S}, n_{H_2O}\right) \qquad (8)$$

where $E_b^{H_2S}$ and $E_b^{H_2O}$ are adsorption energies of a H_2O and a H_2S molecule, respectively, and the two adsorbed species are not interacting. n_{H_2S} and n_{H_2O} are the numbers of adsorbed molecules of H_2S and H_2O, respectively. These adsorption energies can in turn be written as

$$E_b^{H_2O} = U_{dol-H_2O} - \mu_{bw} n_{bw} - E_{dol} \qquad (9)$$

and

$$E_b^{H_2S} = U_{dol-H_2S} - \mu_{H_2S} n'_{H_2S} - \mu_{bw} n'_{bw} - E_{dol} - E_b^{H_2O} \tag{10}$$

where μ_{bw} is the chemical potential of bulk water, and E_{dol} is the energy of the dolomite slab. In the above expression,

$$\mu_{H_2S} = E_{H_2S}^{VASP} - 5.76 \frac{\mathrm{kJ}}{\mathrm{mol}} + \mathrm{RTln}(\mathrm{X}_{\mathrm{H_2S}}^{\mathrm{Sol}}) \tag{11}$$

where $\mathrm{X}_{\mathrm{H_2S}}^{\mathrm{Sol}}$ is the concentration of H_2S in solution. The configurational entropy in Eq. (8) can be calculated as

$$S_{config} = -R \left[n_{H_2S} \ln\left(X_{H_2S}\right) + n_{H_2O} \ln\left(X_{H_2O}\right) \right] \tag{12}$$

In order to minimize the energy, the first order derivatives of ΔG are equated to zero as follows

$$\frac{\partial \Delta G}{\partial n_{H_2S}} = \frac{\partial}{\partial n_{H_2S}} \left(n_{H_2S} E_b^{H_2S} + (n_T - n_{H_2S}) E_b^{H_2O} - T S_{config} \right)$$

$$= E_b^{H_2S} - E_b^{H_2O} + RT \ln\left(n_{H_2S} / \left(n_{H_2O} \bullet \mathrm{X}_{\mathrm{H_2S}}^{\mathrm{Sol}} \right) \right) = 0 \tag{13}$$

where n_T is the total number of adsorption sites, respectively. n_T is estimated to be 14 μmol/m^2 for 100% coverage[31], which corresponds to one water molecule above each cation.

6.3 Results

6.3.1 Adsorption in vacuum

Six configurations with different H_2O orientations were first explored by *ab initio* MD simulations and then optimized by static relaxations. In each configuration, a water molecule lying parallel to the dolomite (104) surface was initially placed above each cation of the surface (total of 2 water molecules per surface unit cell). The initial distance between the O atom of water and the surface cation was chosen to be 2.4Å, which is comparable to the Ca-O$_w$ (O of water) distance for calcite[40,41]. In the lowest energy configuration, orientations of water molecules are different above surface Mg^{2+} and Ca^{2+} ions. Specifically, the water molecule above Mg relaxes so that the Mg-O$_w$ distance is 2.17Å, one hydrogen binds to an O atom of the surface carbonate group by hydrogen bond (with H-O$_{carb}$ distance of 1.83Å) and another H points away from the surface (Figure 6.3.1). Above Ca, the water molecule assumes a position such that the Ca-O$_w$ distance is 2.41Å and both hydrogen atoms bind to surface O$_{carb}$ (one is strong with H-O$_{carb}$ distance of 1.75Å and another one weak with H- O$_{carb}$ distance of 2.11Å). Compared to an earlier classical MD simulation result, which showed the average Mg-O$_w$ distance of 3.02Å and the average Ca-O$_w$ distance of 2.45Å[42], our *ab initio* results not only show stronger surface cation-water binding (manifested in shorter bonds), but also reverse the previous conclusion that Ca^{2+} ions are more strongly bound to water than Mg^{2+} ions. Six similar initial configurations where H_2O was replaced by H_2S were also considered in our calculations. In the lowest energy configuration, the H_2S molecules display similar trends in bond lengths above Mg^{2+} and Ca^{2+} ions to the one found for H_2O (see Table 6.3.1). The main difference between H_2S and H_2O is that in the case of H_2S, only one hydrogen is bound to the surface O$_{carb}$ with H- O$_{carb}$ distances of 2.02Å and 1.86Å for Mg^{2+} and Ca^{2+} sites, respectively (Figure 6.3.1). The adsorption energy of a water molecule on

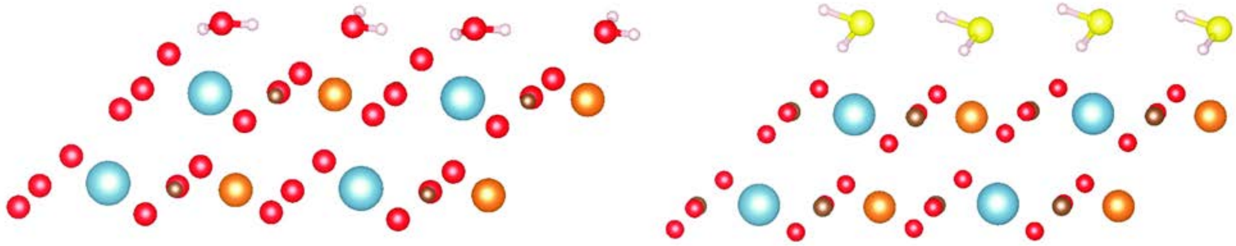

Figure 6.3.1. Left: 1 monolayer of water molecules adsorbed on dolomite (104) surface. Right: 1 monolayer of H_2S molecules adsorbed on dolomite (104) surface. Red: O, yellow: S, orange: Mg, cyan: Ca, brown: C, and white: H.

dolomite surface has shown to be 68.07 kJ/mol in a recent DFT calculation.[43] By using the same equation as $E_{ads} = E^{surf+adsorbate} – E^{surf} – E^{adsorbate}$, we obtain a similar result: 71.16 kJ/mol. The adsorption energy of a water molecule on dolomite (104) surface at 0K is 34.5kJ/mol lower than H_2S (Table 6.3.2). The energy difference narrows to 13.6 kJ/mol with ZPE and entropy corrections, but it does not change the trend that water is more stable on the dolomite surface.

Adsorbate	H_2O		H_2S	Mixture	
Configuration	Energy (eV)	Mg-O (Å)	Energy (eV)	Energy (eV)	Mg-O (Å)
1	-301.436	2.184	-297.934	-299.862	2.237
2	-301.436	2.176	-297.925	-299.861	2.231
3	-301.435	2.176	-297.926	-299.862	2.224
4	-301.436	2.185	-297.931	-299.859	2.227
5	-301.432	2.174	-297.923	-299.863	2.229

Table 6.3.1. Energies and distances between surface Mg and O of adsorbed water for adsorption of a) 1 mono-layer (ML) of H_2O in solution; b) 1 ML of H_2S in solution; and c) a mixed H_2O and H_2S layer in solution.

	In vacuum		**In solution**	
$\Delta H_{abinitio}$	331.1	331.1	338.5	338.5
ΔG_{vib}		-25.6		-33.8
$\Delta E_{H2O-H2S}$	-296.6	-296.6	-296.6	-296.6
$\Delta G_{excitation}$		19.0		19.0
$\Delta G_{solv-vapor}$		-14.3		-14.3
Net energy	34.5	13.6	41.9	12.8

Table 6.3.2. Energy difference between the adsorption of H_2S and H_2O on dolomite (104) surface. The energies shown in this table are in kJ/mol.

6.3.2 Adsorption in solution

The bulk water was initially placed in various positions above the monolayer of water molecules adsorbed on dolomite (104) surface in such a way that the average distance between the oxygen atoms in the bottom layer of bulk water and the highest oxygen atoms in surface carbonate groups ranged from 0.7Å to 3.7Å in increments of 0.5 Å. Each step was calculated by both *ab initio* MD and static relaxation and the lowest energy configuration from this test was found to have the bulk water-surface distance of 3.18Å. In order to further explore the effect of surface water density, we performed additional *ab initio* MD calculations with one extra water molecule inserted between the bulk water and the adsorbed first layer. Five lowest energy configurations from the *ab initio* MD calculations were then optimized in static relaxation. The energies of the five optimized configurations are very similar (Table 6.3.1, the difference is less than 1 meV/atom) and are lower than that of the configuration with lower water density. The energies reported in the table 6.3.2 are the average value of the 5 configurations. A series of similar calculations have been carried out on the H_2S adsorption system. The configurations with the lowest energies (table 6.3.1) were also obtained by inserting an extra water molecule. In further analysis and discussion, we focus on the structures with a higher water density, since they were shown above to have lower energies. With the presence of bulk water, the adsorption energy difference between a H_2O and a H_2S molecule is 41.9 kJ/mol (at 0K) and 12.8 kJ/mol (at room temperature) (Table 6.3.2). ZPE is the major contribution to the corrections. Based on the geometry of surface molecules (Figure 6.3.2) and a series ZPE calculations of different surface layers (the

ΔZPE ($= ZPE^{surf}_{H_2S} - ZPE^{surf}_{H_2O}$) of the atoms in the first 5 layers is only 0.1 kJ/mol higher than those in the first 4 layers), the ZPEs of the adsorbed layer and the first three bulk water layers (6 water molecules) are included in our result. The calculation including bulk water still shows the favorable adsorption of water over H_2S.

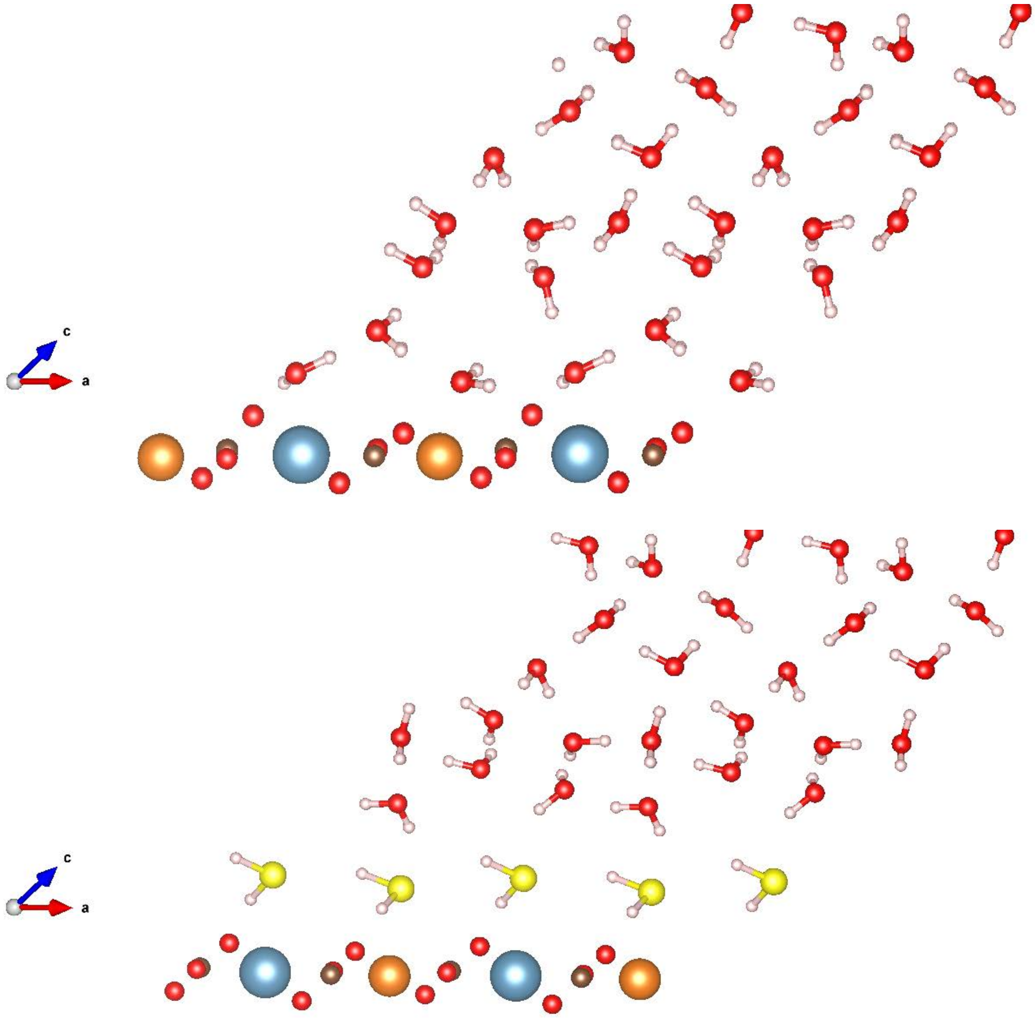

Figure 6.3.2. Top: 1 monolayer of water molecules in solution adsorbed on dolomite (104) surface. Below: 1 monolayer of H_2S molecules adsorbed in solution on dolomite (104) surface. Red: O, yellow: S, orange: Mg, cyan: Ca, brown: C, and white: H. Only atoms of the first layer of the surface are shown.

6.3.3 The adsorption of a mixed layer

Although water is more energetically stable on the dolomite surface than aqueous hydrogen sulfide, our two-phase adsorption model predicts a small amount of H_2S adsorbed on the surface, depending on the adsorption energy difference and pH of solution (effects the concentration of aqueous H_2S). At pH of 7.0 - 8.2 where the modern dolomite is precipitating, 6%~50% of dissolved sulfide are in aqueous H_2S phase. Usually more than 5mM dissolved sulfide was measured in pore water from some modern dolomite sites.[44] According to equation 13, the density of aqueous H_2S on the surface can be up to ~2000 molecules/μm^2 at this pH condition and 5 mM dissolved sulfide concentration (the energy difference of 12.8 kJ/mol was used). In order to test the effect of the surface H_2S on the Mg^{2+}-water complex, a mixed layer of 50% H_2S and 50% H_2O molecules was placed above the dolomite surface in the presence of bulk water. We tested multiple configurations by using the same method as described in previous section and the lowest energy structure was obtained by inserting an extra water molecule between the bulk water and the adsorbed first layer. In the adsorbed mixed layer, the Mg^{2+}-O_w distance increases from ~2.18 Å to ~2.23 Å compared to the respective case of pure layers (Table 6.3.1).

6.4 Discussion

Our calculations show that in vacuum, water is more stable than aqueous H_2S on the dolomite (104) surface at room temperature with the difference in adsorption energy of -13.6 kJ/mol per adsorbed molecule. The added bulk water does not change the trend that it is thermodynamically favorable for water adsorption with the energy gain of -12.8 kJ/mol per adsorbed molecule. In both cases, ZPE and other corrections narrow the energy difference between water and H_2S adsorptions but do not change the conclusion. In summary, calculations under both vacuum and solution conditions do not support the explanation that aqueous H_2S molecules, preferentially adsorbed over H_2O, form a hydrophobic layer on dolomite surface.

The multiphase adsorption model predicts that ~0.002 molecule/nm^2 of aqueous H_2S can be adsorbed at pH condition (7~8.2) and dissolved sulfide concentration (~5 mM) close to some modern environments. This concentration corresponds to a little less than 0.1 % of surface sites, At some local environments where dolomite and high magnesium calcite precipitate, the concentration of dissolved sulfide can be even much higher[45-48] (up to 20mM). Thus, the effect of adsorbed H_2S on the surface magnesium hydration bond is also important to the understanding of the role of dissolved hydrogen sulfide. Generally for heterogeneous catalysis, a good catalyst needs to bind to the reactant strongly enough but not too strongly. Similarly, the strong surface Mg^{2+}-water bond inhibits the dolomite growth, while the relatively weaker surface-H_2S interaction likely increases the competence of CO_3^{2-} to bond to the Mg^{2+}.

On the other hand, according to our study, the adsorbed aqueous H_2S on the surface can affect the Mg^{2+}-H_2O bond distance. Because of the relatively larger size of a H_2S molecule, the H_2S molecules need extra space on the surface, which creates a local environment for relieving surface water molecules from being constrained by the surrounding bulk. When the constraint is released to a certain degree by the local environment created by large H_2S molecules, the surface water molecules relax close to the positions they have without constraint. Therefore, another possibility for H_2S facilitating the carbonation is that, similarly to the H_2S effect on Mg^{2+}-H_2O bond distance, there is room for direct interaction between Mg^{2+} and CO_3^{2-} due to the geometry and the large size of H_2S and larger space between H_2O/H_2S and dolomite surface. Detailed mechanisms for CO_3^{2-} adsorption in the presence of H_2S will be explored in our future studies.

References

(1) Warren, J. Dolomite: Occurrence, Evolution and Economically Important Associations. *Earth-Sci. Rev.* **2000**, *52*, 1–81.

(2) Land, L. S. Failure to Precipitate Dolomite at 25°C from Dilute Solution Despite 1000-fold Oversaturation after 32 Years. *Aquat. Geochem.* **1998**, 361–368.

(3) Ferry, J. M.; Passey, B. H.; Vasconcelos, C.; Eiler, J. M. Formation of Dolomite at 40-80°C in the Latemar Carbonate Buildup, Dolomites, Italy, from Clumped Isotope Thermometry. *Geology* **2011**, *39*, 571–574.

(4) Lippmann, F. *Sedimentary Carbonate Minerals*; Springer, New York, 1973.

(5) Lippmann, F. Stable and Metastable Solubility Diagrams for the System CaCO3–$MgCO_3$–H_2O at Ordinary Temperature. *Bull. Mineral.* **1982**, *105*, 273–279.

(6) Hardie, L. A. Dolomitization; a Critical View of Some Current Views. *J.Sediment.Res.* **1987**, *57*, 166–183.

(7) Vasconcelos, C.; McKenzie, J. Microbial Mediation of Modern Dolomite Precipitation and Diagenesis Under Anoxic Conditions (Lagoa Vermelha, Rio de Janeiro, Brazil). *J. Sediment. Res.* **1997**, *67*, 378–390.

(8) Mazzullo, S. Organogenic Dolomitization in Peritidal to Deep-sea Sediments. *J.Sediment. Res.* **2000**, *70*, 10-23

(9) van Lith, Y.; Warthmann, R.; Vasconcelos, C.; Mckenzie, J. A. Sulphate-reducing Bacteria Induce Low-temperature Ca-dolomite and High Mg-calcite Formation. *Geobiology* **2003**, *1*, 71–79.

(10) Roberts, J. A.; Bennett, P. C.; González, L. A.; Macpherson, G. L.; Milliken, K. L. Microbial Precipitation of Dolomite in Methanogenic Groundwater. *Geology* **2004**, *32*, 277-280.

(11) Wright, D. T.; Wacey, D. Precipitation of Dolomite Using Sulphate-reducing Bacteria from the Coorong Region, South Australia: Significance and Implications. *Sedimentology* **2005**, *52*, 987–1008.

(12) Kenward, P. A.; Goldstein, R. H.; González, L. A.; Roberts, J. A. Precipitation of Low-temperature Dolomite from an Anaerobic Microbial Consortium: the Role of Methanogenic Archaea. *Geobiology* **2009**, *7*, 556–65.

(13) Zhang, F.; Yan, C.; Teng, H. H. In Situ AFM Observations of Ca–Mg Carbonate Crystallization Catalyzed by Dissolved Sulfide: Implications for Sedimentary Dolomite Formation. *Geochim. Cosmochim. Acta.* **2012**, *105*, 44-55.

(14) Zhang, F.; Xu, H.; Konishi, H.; Kemp, J. M.; Roden, E. E.; Shen, Z. Dissolved Sulfide-catalyzed Precipitation of Disordered Dolomite: Implications for the Formation Mechanism of Sedimentary Dolomite. *Geochim. Cosmochim. Acta.* **2012**, *97*, 148–165.

(15) Zhang, F.; Xu, H.; Konishi, H.; Shelobolina, E. S.; Roden, E. E. Polysaccharide-catalyzed Nucleation and Growth of Disordered Dolomite: a Potential Precursor of Sedimentary Dolomite. *Am. Mineral.* **2012**, *97*, 556–567.

(16) Kluge, S.; Weston, J. Can a Hydroxide Ligand Trigger a Change in the Coordination Number of Magnesium Ions in Biological Systems? *Biochemistry* **2005**, *44*, 4877–85.

(17) Roberts, J. A.; Kenward, P. A.; Fowle, D. A.; Goldstein, R. H.; González, L. A.; Moore, D. S. Surface Chemistry Allows for Abiotic Precipitation of Dolomite at Low Temperature. *Proceedings of the National Academy of Sciences of the United States of America* **2013**, *110*, 14540–14545.

(18) Katz, A.; Glusker, J. Deprotonation of Water in the Presence of Carboxylate and Magnesium Ions. *J. Phys. Chem. B.* **1998**, *5647*, 6342–6350.

(19) Yang, Y.; Sahai, N.; Romanek, C. S.; Chakraborty, S. A Computational Study of Mg^{2+} Dehydration in Aqueous Solution in the Presence of HS^{-} and Other Monovalent Anions – Insights to Dolomite Formation. *Geochim. Cosmochim. Acta.* **2012**, *88*, 77–87.

(20) de Leeuw, N. H.; Parker, S. C. Surface–water Interactions in the Dolomite Problem. *Phys. Chem. Chem. Phys.* **2001**, *3*, 3217–3221.

(21) Yang, M.; Stipp, S. L. S.; Harding, J. Biological Control on Calcite Crystallization by Polysaccharides. *Cryst. Growth Des.* **2008**, *8*, 4066–4074.

(22) Cooke, D. J.; Gray, R. J.; Sand, K. K.; Stipp, S. L. S.; Elliott, J. A. Interaction of Ethanol and Water with the {1014} Surface of Calcite. *Langmuir* **2010**, *26*, 14520–9.

(23) Sand, K. K.; Yang, M.; Makovicky, E.; Cooke, D. J.; Hassenkam, T.; Bechgaard, K.; Stipp, S. L. S. Binding of Ethanol on Calcite: the Role of the OH Bond and Its Relevance to Biomineralization. *Langmuir* **2010**, *26*, 15239–47.

(24) Falini, G.; Gazzano, M.; Ripamonti, A. Magnesium Calcite Crystallization from Water–alcohol Mixtures. *Chem. Commun.* **1996**, 1037–1038.

(25) Kresse, G.; Furthmüller, J. Efficient Iterative Schemes for Ab Initio Total-energy Calculations Using a Plane-wave Basis Set. *Phys. Rev. B: Condens. Matter Mater. Phys.* **1996**, *54*, 11169–11186.

(26) Perdew, J.; Burke, K.; Ernzerhof, M. Generalized Gradient Approximation Made Simple. *Phys. Rev. Lett.* **1996**, *77*, 3865–3868.

(27) Gieskes J. M. Interstitial Water Studies, Leg 15 – Alkalinity, pH, Mg, Ca, Si, PO_4, and NH_4. *Init. Rep. Deep Sea Drilling Proj.* **1973**, *15*, 813–830.

(28) Kastner, M.; Elderfield, H. Diagenesis and Interstitial-water Chemistry at the Peruvian Continental Margin—Major Constituents and Strontium Isotopes. *Proceedings of the Ocean Drilling Program, Scientific Results* **1990**, *112*, 413–440.

(29) Last, W. Lacustrine Dolomite—an Overview of Modern, Holocene, and Pleistocene Occurrences. *Earth-Sci. Rev.* **1990**, *27*, 221–263.

(30) Stumm, W; Morgan, J. J. *Aquatic Chemistry*; Genium Publishing Corporation: Schenectady, NY, 1996; pp. 398–404.

(31) Pokrovsky, O.; Schott, J.; Thomas, F. Dolomite Surface Speciation and Reactivity in Aquatic Systems. *Geochim. Cosmochim. Acta.* **1999**, *63*, 3133–3143.

(32) Plimpton, S. Fast Parallel Algorithms for Short-range Molecular Dynamics. *J.Computat. Phys.* **1995**, *117*, 1–42.

(33) Jorgensen, W. L.; Chandrasekhar, J.; Madura, J. D.; Impey, R. W.; Klein, M. L. Comparison of Simple Potential Functions for Simulating Liquid Water. *J. Phys. Chem.* **1983**, *79*, 926.

(34) Grimme, S. Semiempirical GGA-Type Density Functional Constructed with a Long-range Dispersion Correction. *J. Comput.Chem.* **2006**, *27*, 1787–1799.

(35) McQuarrie, D.A.; Simon, J. D. *Molecular Thermodynamics*; University Science Books, Sausalito,CA, 1999; p. 656.

(36) Pinney, N.; Kubicki, J. D.; Middlemiss, D. S.; Grey, C. P.; Morgan, D. Density Functional Theory Study of Ferrihydrite and Related Fe-Oxyhydroxides. *Chem. Mater.* **2009**, *21*, 5727–5742.

(37) Senekowitsch, J.; Carter, S.; Zilch, A. Theoretical Rotational–vibrational Spectrum of H_2S. *J. Chem. Phys.* **1989**, *90*, 783-794.

(38) Hoffman, B. C.; Sherrill, C. D.; Schaeffer III, H. F. Comparison Between Molecular Geometry and Harmonic Vibrational Frequency Predictions from CISD and CISDTQ Wave Functions for Hydrogen Sulfide. *J. Chem. Phys.* **1997**, *107*, 10616–10619.

(39) Wagman, D. D. *Selected Values of Chemical Thermodynamic Properties: Tables for the First Thirty-Four Elements in the Standard Order of Arrangement*; US National Bureau of Standards, 1968.

(40) de Leeuw, N.; Parker, S. Atomistic Simulation of the Effect of Molecular Adsorption of Water on the Surface Structure and Energies of Calcite Surfaces. *J. Chem. Soc., Faraday Trans.* **1997**, *93*, 467–475.

(41) Lardge, J.; Duffy, D.M.; Gillian, M.J.; Watkins, M. Ab Initio Simulations of the Interaction Between Water and Defects on the Calcite ($10\bar{1}4$) Surface. *J. Phys. Chem. C.* **2010**, *114*, 2664–2668.

(42) Wright, K.; Cygan, R.; Slater, B. Structure of the ($10\bar{1}4$) Surfaces of Calcite, Dolomite and Magnesite Under Wet and Dry Conditions. *Phys. Chem. Chem. Phys.* **2001**, *3*, 839–844.

(43) Escamilla-Roa, E.; Sainz-Díaz, C. I.; Huertas, F. J.; Hernández-Laguna, A. Adsorption of Molecules onto ($10\bar{1}4$) Dolomite Surface: an Application of Computational Studies for Microcalorimetry. *J. Phys. Chem. C.* **2013**, *117*, 17583–17590.

(44) Wortmann, U.; Bernasconi, S.; Böttcher, M. Hypersulfidic Deep Biosphere Indicates Extreme Sulfur Isotope Fractionation During Single-step Microbial Sulfate Reduction. *Geology* **2001**, *29*, 647-650.

(45) Mossmann J. R.; Aplin A. C.; Curtis C. D.; Coleman M. L. Geochemistry of Inorganic and Organic Sulphur in Organic-rich Sediments from the Peru Margin. *Geochim. Cosmochim. Acta.* **1991**, *55*, 3581–3595.

(46) Barry J. P.; Kochevar R. E.; Baxter C. H. The Influence of Pore-water Chemistry and Physiology on the Distribution of Vesicomyid Clams at Cold Seeps in Monterey Bay: Implications for Patterns of Chemosynthetic Community Organization. Limnol. Oceanogr. **1997**, *42*, 318–328.

(47) Niewöhner C.; Hensen C.; Kasten S.; Zabel M.; Schulz H. D. Deep Sulfate Reduction Completely Mediated by Anaerobic Methane Oxidation in Sediments of the Upwelling Area off Namibia. *Geochim. Cosmochim. Acta.* **1998**, *62*, 455–464.

(48) Fossing H.; Ferdelman T. G.; Berg P. Sulfate Reduction and Methane Oxidation in Continental Margin Sediments Influenced by Irrigation (South-East Atlantic off Namibia). *Geochim. Cosmochim. Acta*. **2000**, *64*, 897–910.

Chapter appendix

(1) The expression for the water chemical potential at finite temperature (Pinney et al., 2009)

$\Delta\mu_{H_2O}^{liquid}\ (T) = E_{H_2O}^{molecule} + \Delta G_{H_2O}^{exciations}(T) - \Delta G_{H_2O}^{vaporization}(T)$

T=298.15K

$$\Delta G_{H_2O}^{exciations}(T) = -RT\ln\left\{\left[\frac{2\pi(\sum_i m_i)k_BT}{h^2}\right]^{\frac{3}{2}}\frac{V_e}{N}\right\} - RT\ln\left[\frac{\pi^{\frac{1}{2}}}{\sigma}\left(\frac{T^3}{\theta_A\theta_B\theta_C}\right)^{\frac{1}{2}}\right] + RT\sum_i^3\left[\frac{h\nu_i}{2k_BT} + \ln\left(1 - e^{-h\nu_i/k_BT}\right)\right]$$

Θ_{rot} = 40.1, 20.9, 13.4 K, σ =2 (symmetry number)

$\Theta_{vib,i}$ = 5360, 5160, 2290 K

G_{trans} = -37.00 kJ/mol

G_{rot} = -9.33 kJ/mol

G_{vib} = 53.88 kJ/mol

$\Delta G_{H_2O}^{exciations}(298.15K) = 7.55\ kJ/mol$

$\Delta G_{H_2O}^{vaporization}(298.15K) = -8.61\ kJ/mol$

So,

$\Delta H_{H_2O}^{liquid}\ (T) = E_{H_{2O}}^{molecule} - 1.06\ kJ/mol$

(2) For aqueous H_2S chemical potential at finite temperature

Similarly,

$\Delta\mu_{H_2S}^{aq}\ (T) = E_{H_2S}^{molecule} + \Delta G_{H_2S}^{exciations}(T) - \Delta G_{H_2S}^{solvation}(T)$

$\theta_{D,j} = h\nu/k_B$

The vibrational frequencies (cm^{-1}) of a H_2S molecule (Hoffmann et al., 1997):

ν1= 2721.05 symmetry stretching
ν2= 1214.0 bend
ν3= 2729.3 asymmetry stretching

Θ_{rot} = 14.9, 12.93, 6.93 K (Senekowitsch et al., 1988)

G_{trans} = -39.35 kJ/mol

G_{rot} = -11.95 kJ/mol

G_{vib} = 39.85 kJ/mol

$\Delta G_{H_2S}^{exciations}(298.15K) = -11.45 kJ/mol$

At 298.15K, 1 atm, standard states (Wagman et al., 1968):

H_2S (g): $\Delta G_f^0 = -33.56\ kJ/mol$

H_2S (aq): $\Delta G_f^0 = -27.87\ kJ/mol$

$\Delta G_{H_2O}^{solvation}(298.15K) = 5.69\ kJ/mol$

In sum,

$\Delta\mu_{H_2S}^{aq}\ (T) = E_{H_2S}^{molecule} - 5.76\ kJ/mol$

This Chapter was previously published (*Journal of Physical Chemistry C*, 118 (2014), 15716-15722) with the following coauthors:

Zhizhang Shen[1], Yun Liu[2,3], Philip, E. Brown[1], Izabela Szlufarska[2,3], and Huifang Xu[1,3]

[1]Department of Geoscience, University of Wisconsin-Madison, 1215 W. Dayton Street, Madison, WI53706, USA

[2] Department of Materials Science and Engineering, University of Wisconsin-Madison, 1509 University Avenue, Madison, WI53706, USA

[3] Materials science program, University of Wisconsin-Madison, 1509 University Avenue, Madison, WI53706, USA

Chapter 7. The Role of Polysaccharides in the Dolomite Growth

7.1 Introduction

The prevalent opinion[1] about the dolomite problem is that the key factor accounting for the sluggish kinetics of forming dolomite at room temperature is the Mg hydration. As mentioned in section 6.1, it is most likely that catalysts play an active role in dehydration of surface Mg^{2+}. One hypothesis for the dehydration of surface Mg^{2+} is that catalysts can be strongly adsorbed to crystal surfaces replacing the surface water molecules[2,3]. We tested this hypothesis in chapter 6. Our previous work suggests that water is more favorably adsorbed on the surface than the hydrogen sulfide[4]. The other hypothesis is that catalysts can lower the dehydration barrier of surface Mg^{2+} so that carbonate can approach and be adsorbed onto the surface. The goal of this chapter is to test this hypothesis.

Polysaccharides were chosen for our study because this class of molecules is shown to promote the dolomite growth at room temperature[3]. It is also because polysaccharides are the major component of extracellular polymeric substances (EPS), which is a universal catalyst no matter what the bacteria species is. Instead of studying the long-chained polysaccharides that contain thousands of atoms, we tested α-D-mannose (one of the major monomers making up the polysaccharides used in experiments[3,5]) and oligo-mannose (three units of mannose). Therefore, our simulations have only considered the local small blocks of the long chained polysaccharides. The effects of mannose and oligo-mannose in the dehydration barrier of surface Mg^{2+} were investigated by using classical molecular dynamics (MD) simulations and potential of mean force (PMF) method.

7.2 Simulation Details

The force fields used in this study are described in section 5.2. The dolomite slab has approximate dimensions of 23.12×24.06×19.10 Å^3. The slab has two (top and bottom) free surfaces with (104) orientation. The slab contains 105 calcium, 105 magnesium, 210 carbon and 630 oxygen atoms and it has seven atomic layers with atoms in the middle three layers of the slab being fixed in space while the top two and the bottom two layers are allowed to relax during simulations. A water box is added above the top surface and because periodic boundary conditions are applied in all three spatial dimensions, this water box is also in contact with the bottom dolomite surface. The total height of the water box is 52 Å, it has 880 water molecules, which corresponds to density of ~ 0.9 g/cm^3. The systems of water adsorption, mannose and tri-mannose adsorptions on dolomite (104) surface were relaxed by using classical MD simulations at room temperature and 1 atmosphere. The code DL_POLY_class[6] was used and each system was simulated in the NVE (constant number of particles, volumes, and energy) ensemble. Equations of motion were integrated using the Verlet-Leapfrog algorithm using a timestep of 1 fs. The long-range Coulomb interactions were calculated using the smooth particle mesh Ewald sum (SPME) with a real space cut-off of 10.1 Å. Multiple configurations of mannose and tri-mannose were explored and the details about the configurations can be found in the results section.

The potential of mean force (PMF) for water molecules binding/unbinding to surface Mg at dolomite (104) surface with and without the presence of sugar were calculated. The reaction coordinate is the distance between the oxygen atom of a water molecule and a surface Mg atom along the z direction. The PMF calculations were conducted in NVT (constant number of particles, volumes, and temperature) ensemble by using the Nosé-Hoover thermostat with a relaxation time of 0.5 ps. The PLUMED package[7] interfaced to DL_POLY Classic was employed to run Umbrella Sampling[8,9]. The weighted histogram analysis method (WHAM[10]) was used to analyze the results of umbrella sampling and to calculate the unbiased free energy along the reaction pathway. In each window sampling, we ran simulations for 6 ns, which was sufficient to reach the convergence of unbiased free energy within 0.1 kcal/mol. Multiple simulations were conducted in each case, as explained in the subsequent sections.

7.3 Results

In order to determine the effects of sugar on dehydration of surface Mg, we first studied water adsorption on the dolomite (104) surface in the absence of sugar and we used it as a reference for later calculations that involve sugar. Classical MD simulation of the system was performed for 2 ns at room temperature and 1 atmosphere to examine the water configurations on the dolomite surface. Radial distribution functions (RDF) of Ca-Owater, Mg-Owater and Ocarbonate-Hwater found peaks at 2.38 Å, 1.9 Å and 1.65 Å, respectively (Figure 7.3.1). A snapshot of the MD simulation of the water-dolomite (104) surface is shown in Figure 7.3.2a. Based on our analysis of water density profile along the *z* direction (Figure 7.3.2b), we can see that there are two hydration layers above the dolomite surface: one is at ~2.0 Å above the average height of the surface cations, and another one at 3.06 Å. The first and second peaks at 1.88 Å and 2.23 Å in the density profile correspond to the interactions between surface Mg and O atoms in water molecules and between Ca and water O atoms, respectively. The peak at 3.06 Å represents interactions between water hydrogen and oxygen of surface. The presence of such two-layer hydration is also supported by an x-ray reflectivity work of the water-dolomite (104) interface that has found a first hydration layer at a height of 2.31 Å above the surface cation[11]. The two-layer hydration is also similar to that found at the water-calcite (104) interface, which has been studied more extensively than the water/dolomite interface. Discrepancies in the height of the two-hydration layers between simulations and experiments are not uncommon in calcite-water interface studies. For example, the height of the first hydration layer was determined from experiments to be at 2.0 Å[12] or 2.14 Å[13] while the simulations show a range from 2.0 to 2.4 Å[14–16]. The discrepancies found for dolomite/water interface between our simulation and the scarce previous experimental studies are of the similar order of magnitude as for the calcite/water interface. In our

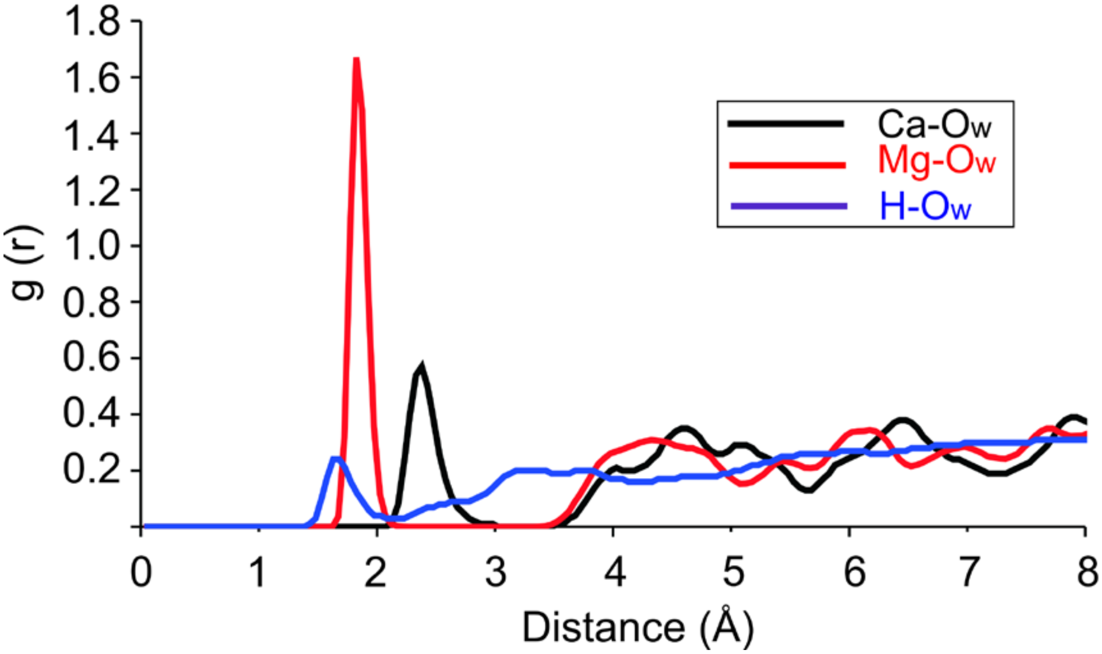

Figure 7.3.1. Radial distribution functions for Ca-Ow (water oxygen) pair (dark gray line), Mg-Ow pair (gray line) and H-O (carbonate oxygen) pair (black line).

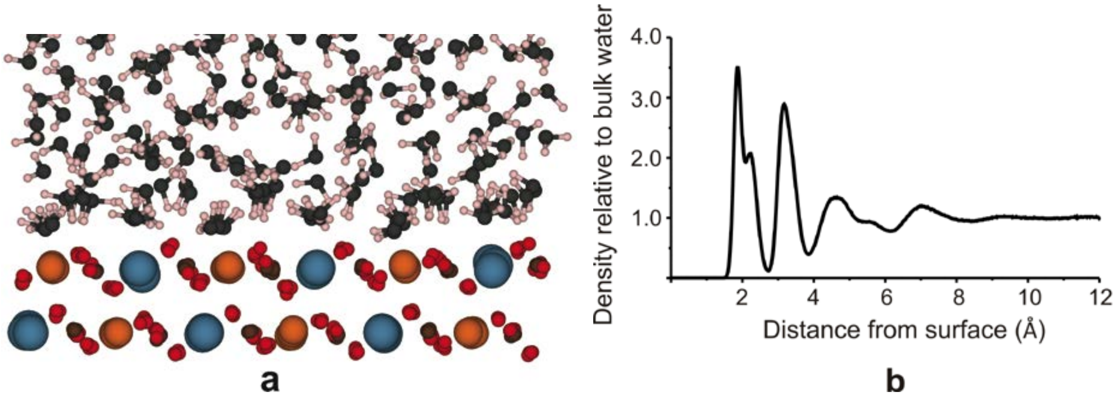

Figure 7.3.2. (a) Snapshot of MD simulation showing the interface between dolomite (104) surface and water molecules. The atoms Ca, Mg, C, O, Ow and H are in blue, range, brown, black and white colors. (b) The density profile along the perpendicular distance from the surface.

simulations we identified two types of metastable water configurations above surface Mg. In the first configuration one of the hydrogen atoms of water is pointing towards the nearby carbonate due to a hydrogen bond between the hydrogen atom and the oxygen atom in the carbonate ion (Figure 7.3.3a). In the second configuration (Figure 7.3.3b) both hydrogen atoms point upwards (away from the surface) and they are not bonded to the surface carbonate. Four water molecules (two with configuration 1 and two with configuration 2) were chosen for the subsequent calculations of free energies. Specifically, using the methods described in the previous sections we calculated PMF of a water molecule being desorbed from the surface through the first two hydration layers into the bulk. In Figures 7.3.3c and 7.3.3d, we can see that there are two energy wells at ~1.9 Å and ~3.2 Å, which are corresponding to the two hydration layers, respectively. The free energies of the adsorption of the first layer water to the surface Mg^{2+} varies from -6.67 to -7.32 kcal/mol. Here, we find that the energy barrier for dissociation of a water molecule from the surface Mg atoms (equivalent to the energy barrier to move water molecule away from the surface past the first hydration layer) ranges from 9.40 to 9.69 kcal/mol.

This range is close to energies calculated for a water molecule leaving the first hydration shell of Mg^{2+} in solution, which are 9.0 kcal/mol[17] or ~10.5 kcal/mol[18].

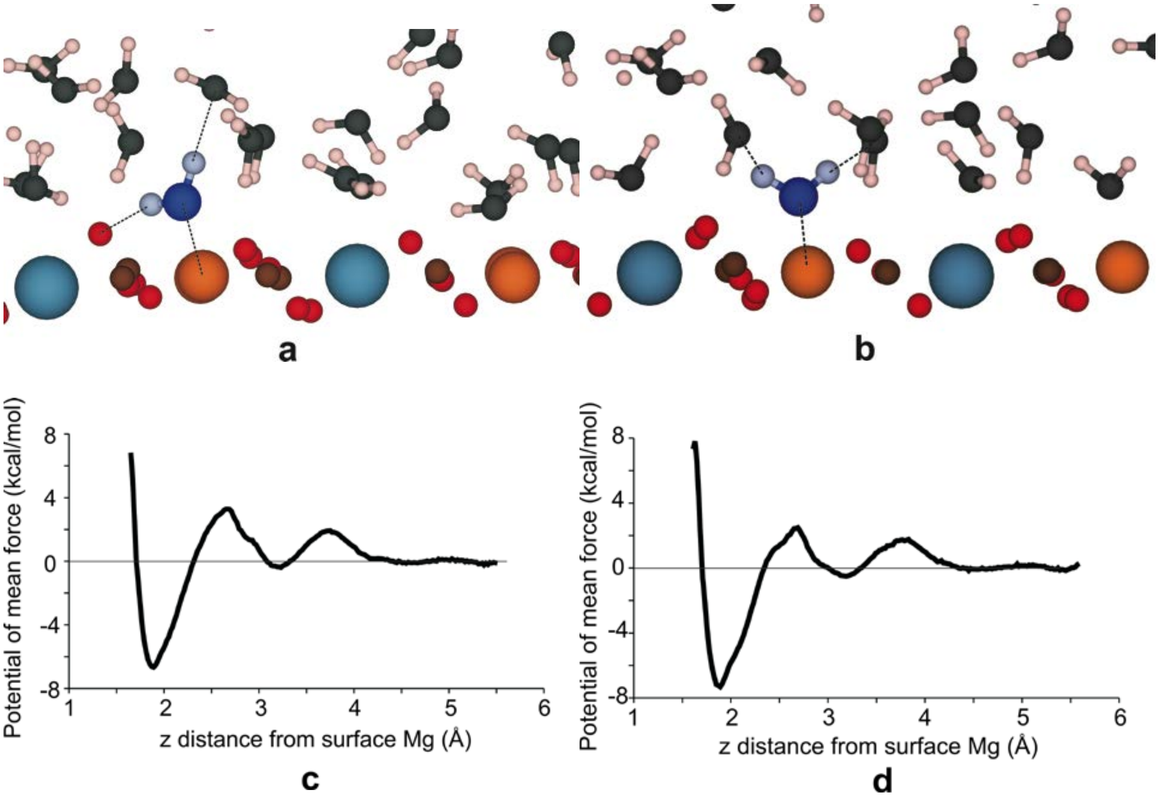

Figure 7.3.3. (a) The configuration of type 1 water molecules adsorbed onto surface Mg^{2+}. (b) The configuration of type 2 water molecules adsorbed onto surface Mg^{2+}. (c) Potential of mean force curve for water molecule I leaving the first two hydration layers. (d) Potential of mean force curve for water molecule II leaving the first two hydration layers.

To examine whether polysaccharides could decrease the hydration barrier of surface water, we first tested the effect of monosaccharide (here mannose), which is the basic unit of carbohydrate and contains both the hydrophilic –OH group and the non-polar C–H bonds. Four different mannose configurations on the dolomite surface were simulated and two of the relaxed structures were chosen for PMF calculations based on the fact that they have the lowest energy configurations among the four initial configurations. The two lowest energy configurations represent two distinct orientations of mannose on the surface: one lies flat on the surface (Figure 7.3.4a and 7.3.4b) and the other one stands vertically above the surface (Figure 7.3.4c). In the system with mannose lying flat on the surface, two sets of PMF calculations were performed for the two water molecules that are adjacent to the mannose and that are bonded to the surface Mg (Figure 7.3.4a and 7.3.4b). The energy barriers for the first layer hydration are shown to be 9.83 and 9.53 kcal/mol (Figure 7.3.4d and 7.3.4e), which means that there is no obvious effect of mannose with flat configuration on the dehydration of surface Mg. However, in one of the PMF profiles (Figure 7.3.4d), the peak at ~3.7 Å (~10.5 kcal/mol) is much higher than the remaining PMF profile, indicating the increase of dehydration barrier for the second hydration layer. This increase is caused by the interactions between hydroxyl group of the mannose and the desorbing water molecule as it is trying to leave the second hydration layer. Qualitatively similar results are found in the system with a vertical mannose, where the energy barrier for the water molecule leaving the surface Mg (~9.67 kcal/mol) (Figure 7.3.4f) is not significantly different from the case without mannose.

Although the monomer of mannose was found to have a negligible effect on the dehydration of surface Mg-H_2O complex, it is possible that the polymerization of monomers plays a role in the process. In this study, we use oligo-saccharide (or tri-

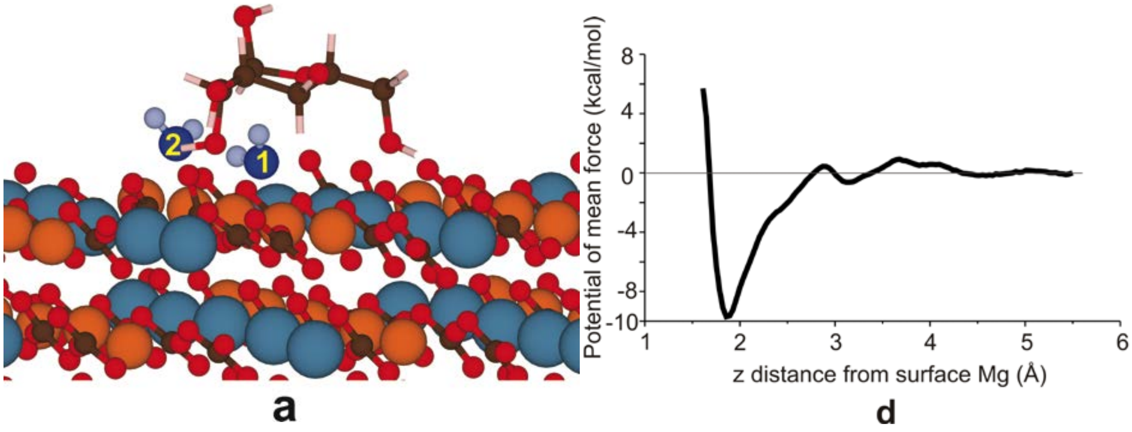

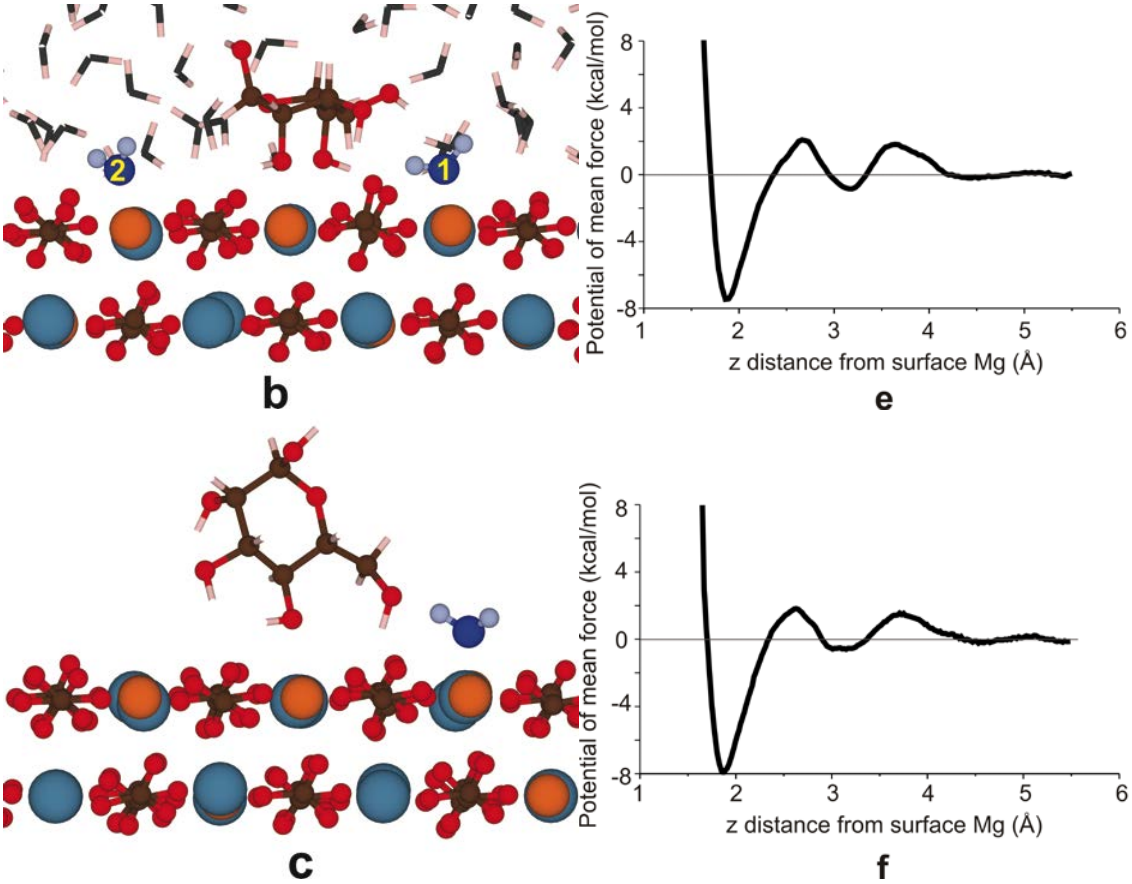

Figure 7.3.4. (a) The flat configuration of mannose adsorbed on the surface. Water molecules are included in the simulations but not shown in this figure. (b) Side view of the mannose on the surface. (c) The vertical configuration of mannose adsorbed onto the surface. Water molecules are included in the simulations but not drawn in this figure. (d) Potential of mean force curve for water molecule #1 leaving the first two hydration layers in the presence of a flat mannose as shown in (a) and (b). (e) Potential of mean force curve for water molecule #2 leaving the first two hydration layers. (e) Potential of mean force curve for water molecule leaving the first two hydration layers in the presence of vertical mannose as shown in (c).

saccharide, three units of α-D-monosaccharide joined by 1-4 linkage) as a model polysaccharide. We explored seven different tri-mannose configurations above dolomite (104) surface by performing MD simulations for 3 ns at room temperature and 1 atmosphere (see appendix for the details and energies of the seven configurations). In the lowest energy system (configuration 1), one unit of the three six-member rings is bound to the surface via the interactions between its –OH group and the surface ($O_{mannose}$-Mg and $H_{mannose}$-O_c) while the other two units are away from the surface. The configuration of the unit that bonds to the surface and the solvation environment around this unit are very similar to the system of a vertical mannose adsorbed on the surface. No obvious effect of this configuration of tri-mannose is expected for weakening the surface Mg-water interactions. The energies of the other configurations of tri-mannose systems are comparable. In configurations 2, two units of the tri-mannose bond to the dolomite surface and the third unit is away from the surface. The other configurations (3,4, 5, 6 and 7), with about 1~2 eV higher energy for the whole simulation box (containing more than 3000 atoms) than the ground state configuration 1, display a bridge shape but overall lie flat on the surface (Figure 7.3.5a and 7.3.5b), which create a low water density space just beneath the bridge near the hydrophobic –CH groups. The effect of this bridge shape and the space of low water density under the bridge cannot be tested in the case of monomers. Thus, we performed PMF calculations of desorption of two surface water molecules for configurations 3 and 5 (four PMF calculations in total). In one case, the water molecule lies beneath the bridge and the low water density space is above Mg ions. In another case the desorbing water molecule lies outside the bridge but is adjacent to the low water density space. In the PMF profiles (Figure 7.3.5c) for water molecules under the bridge, a decreased energy barrier is shown for the dehydration of the first hydration layer (~8.67 kcal/mol in configure 3 and ~8.59 kcal/mol in configuration 5, in other words, the barrier is about 0.73-1.10 kcal/mol lower than that in pure water adsorption system). The PMF profile for the water molecule just outside the bridge (Figure 7.3.5d) has shown a similar amount of decrease in the hydration barrier (~8.66 kcal/mol).

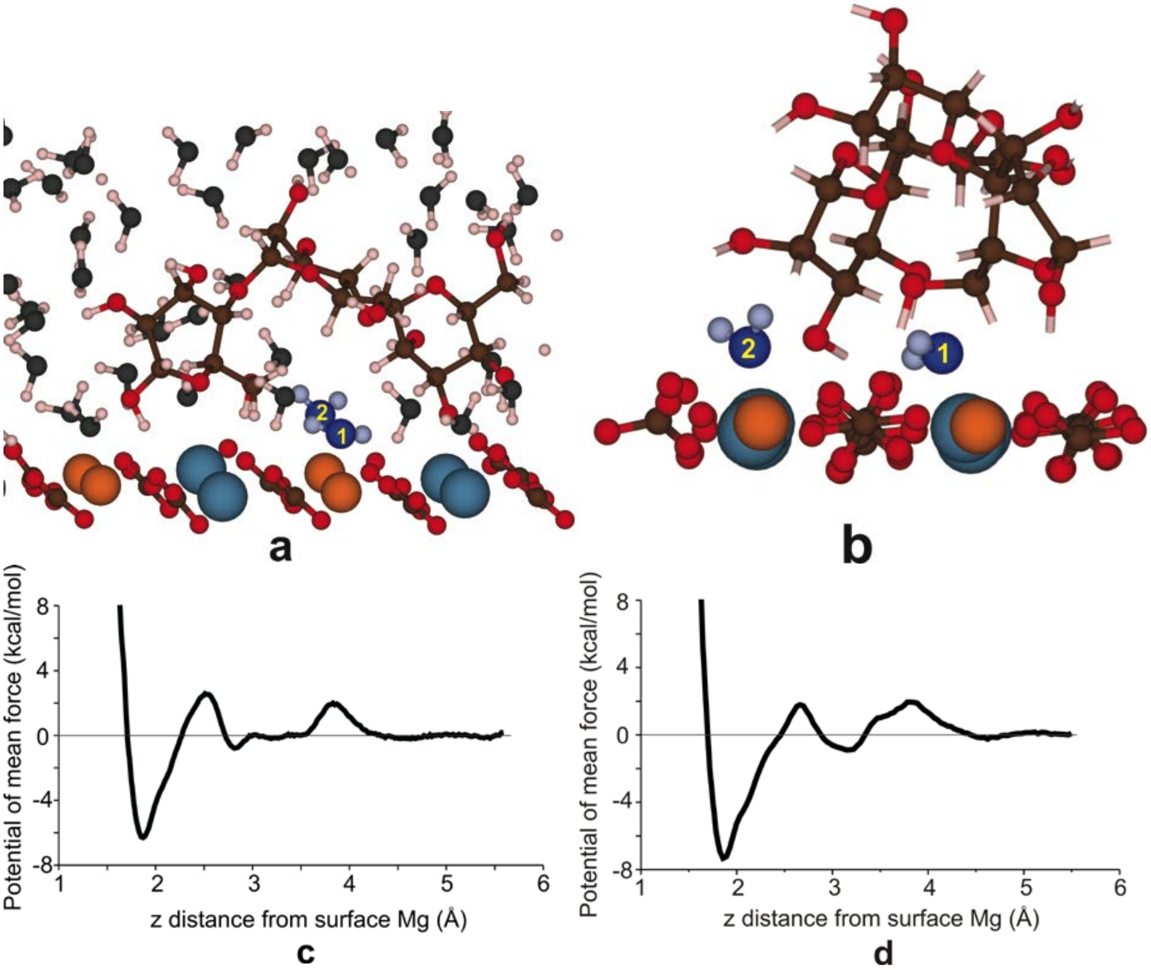

Figure 7.3.5. (a) The bridge shape configuration of tri-mannose lying flat on the dolomite surface. (b) Side view of the tri-mannose on the surface. Water molecules are included in the simulations but not shown in this figure. (c) Potential of mean force curve for water molecule #1 inside the bridge leaving the first two hydration layers. (d) Potential of mean force curve for water molecule #2 outside the bridge leaving the first two hydration layers.

7.4 Discussion

Our PMF calculations show that the monosaccharide (mannose) does not have the ability to promote the dehydration of surface magnesium. Although the calculations were carried out with the presence of one monosaccharide, the concentration of monosaccharide is not expected to be a major factor. According to our complementary experiments at low temperatures (see chapter appendix), it shows that the increase of monosaccharide used in the synthesis does not foster the incorporation of Mg into the carbonate structure.

We considered the two major metastable configurations of tri-mannose on the dolomite (104) surface (stand vertically and lying flat). The bridge-shaped configurations of oligosaccharide lying flat on the dolomite surface are shown to be able to decrease the dehydration barrier for surface magnesium. Hydrophobic space with low water density created by this bridge shape is also observed in our MD simulations of solvation of other tri-saccharides (tri-glucose, tri-galactose and tri-xylose). This phenomenon is common in the helix of polysaccharides that the interior of the helix is hydrophobic while the outer shell is hydrophilic[19]. The bridge-shaped configurations are not the lowest energy configurations that we explored in our study but the energy difference is small considering the number of atoms in the simulation box. On the other hand, let us consider the following scenario. In EPS, the polysaccharides usually contain substituents of low molecular weight, such as negative charged carboxylate groups and sulfates[20]. In aqueous environment, the carboxylate groups can replace the water molecules bonded to Mg^{2+} and Ca^{2+} ions[21]. For example, the Log K values for the following two reactions at zero ionic strength are both 1.43:

$$[Mg(H_2O)_6]^{2+} + HCOO^- =[Mg(H_2O)_5HCOO]^+ + H_2O$$

$$[Ca(H_2O)_x]^{2+} + HCOO^- = [Ca(H_2O)_{x-1}HCOO]^+ + H_2O$$

Because of the strong attractions between Ca/Mg and carboxylate/sulfate, it is possible that the flat configuration of the EPS polysaccharides is stable on the dolomite surface.

Most of the previous studies on the role of polysaccharides or carboxyl groups in dolomite growth are focused on the desolvation of $[Mg(H_2O)_6]^{2+}$ in the solution and the adsorption of Mg to the surface. One mechanism that proposed by some recent works is that the surface carboxyl functional groups could dewater and adsorb Mg^{2+} and form a thin dolomite template for further precipitation under supersaturated conditions[22,23]. Although the energy barrier for the dehydration of one water molecule from the $[Mg(H_2O)_6]^{2+}$ is about 9.0~10.5 kcal/mol[17,18], the energy barrier for the adsorption of hydrated Mg^{2+} ions onto the calcite surface is only 3.06 kcal/mol and is very similar to the adsorption of calcium[17]. Therefore, the adsorption of hydrated Mg from solution to the surface is not a critical step for the dolomite growth. And a thin dolomite template does not necessarily facilitate the further growth of dolomite. This is because previous X-ray reflectivity works have shown that only 1 layer[24] or 2-layer[11] thick film could form on the dolomite substrate during reaction with the supersaturated solution. Furthermore, careful examination of their published results indicates that their XRD data are too noisy to be able to be distinguished as dolomite peaks[25].

Our work has focused on the dehydration of surface Mg and has shown that the polysaccharide is able to decrease the dehydration barrier for the surface Mg by its hydrophobic –CH groups, which is the possible major effect of polysaccharide on the dolomite growth at low temperatures.

7.5 Implication for dolomite growth at low temperature

Most of the modern dolomites are precipitated in shallow and saline environments, such as sabkhas tidal flats, Coorong region and several playas in North America, where the metabolism of bacteria is active and biomass of living organisms or recently living organism is widely available. However, the formation of dolomite does not require living microorganisms or metabolic activity. A recent work has shown that bound-EPS of non-metabolizing biolmass can catalyze the growth of dolomite[5]. Our theoretical work, along with previous experiments[3], indicates that polysaccharides (the major component of EPS) and even segments of polysaccharides can overcome the kinetic barrier of dolomite growth at low temperatures. It is both the hydrophilic and hydrophobic groups of polysaccharides or other organic macromolecules that make the dehydration of surface Mg easier. Although carbohydrates are usually degraded quickly in water column, it is estimated that the carbohydrates can be preserved in marine sediments (100-200 m below the sea floor) for 10^5 to 10^6 years[25]. Sulfurized carbohydrates can be even preserved in Jurassic sediments[26]. At the same time, the duration of dolomitization of Latemar buildup is estimated to be 60-120 years[27]. Considering the intervals between the episodes of dolomitization, the total duration of the dolomitization process could be much longer than 100 years. Nevertheless, the relative long residence time of carbohydrates in certain marine environments, together with elevated Mg/Ca ratio, could facilitate the formation of early burial dolomite.

7.6 Future work

In our current work, we assumed that when the surface Mg-water interactions are weakened, it is easy for carbonate ions to be adsorbed onto the surface Mg. In other words, we assumed that the dehydration process is more important than the swap of carbonate ions and surface water. Therefore, the pathway for carbonate ions to supplant the surface water molecules with the presence of polysaccharide needs to be further studied in detail. And this further study would include the PMF calculations of carbonate ions adsorption onto the surface cations with and without polysaccharides. By calculating the adsorption barriers for carbonate, we would be able to clarify the following two questions. The first one is whether the adsorption barrier for the adsorption of carbonate to the surface Mg is significantly higher than that to the surface Ca. The answer to this question can help confirm that the hydration layers above surface Mg result in the kinetic slowness of the dolomite growth at low temperatures. The second question is whether the polysaccharides have any effects on the adsorption process(es).

As hydrogen sulfides do not have the same hydrophobic groups as polysaccharides, it is reasonable to believe that the exact role of hydrogen sulfides in the dolomite growth is different from that of polysaccharides. We proposed two possible catalytic mechanisms of adsorbed hydrogen sulfide on the Ca-Mg carbonate crystallization at low temperatures in chapter 6. In the future, we could also apply the PMF methods and classical MD simulations to determine whether the adsorbed hydrogen sulfides (aqueous H_2S and HS^-) could decrease the adsorption barrier for carbonate ions.

References

(1) Lippmann, F.; Lippmann, F. *Sedimentary Carbonate Minerals*; Springer, 1973; Vol. 228.

(2) Zhang, F.; Xu, H.; Konishi, H.; Kemp, J. M.; Roden, E. E.; Shen, Z. Dissolved Sulfide-Catalyzed Precipitation of Disordered Dolomite: Implications for the Formation Mechanism of Sedimentary Dolomite. *Geochim. Cosmochim. Acta* **2012**, *97*, 148–165.

(3) Zhang, F.; Xu, H.; Konishi, H.; Shelobolina, E. S.; Roden, E. E. Polysaccharide-Catalyzed Nucleation and Growth of Disordered Dolomite: A Potential Precursor of Sedimentary Dolomite. *Am. Mineral.* **2012**, *97*, 556–567.

(4) Shen, Z.; Liu, Y.; Brown, P. E.; Szlufarska, I.; Xu, H. Modeling the Effect of Dissolved Hydrogen Sulfide on Mg 2+ − Water Complex on Dolomite {104} Surfaces. *J. Phys. Chem. c* **2014**, *118*, 15716–15722.

(5) Zhang, F.; Xu, H.; Shelobolina, E. S.; Konishi, H.; Converse, B.; Shen, Z.; Roden, E. E. The Catalytic Effect of Bound Extracellular Polymeric Substances Excreted by Anaerobic Microorganisms on Ca-Mg Carbonate Precipitation : Implications for the " Dolomite Problem ." *Am. Mineral.* **2015**, *100*, 483–494.

(6) Smith, W.; Forester, T. R. DL_POLY_2.0: A General-Purpose Parallel Molecular Dynamics Simulation Package. *J. Mol. Graph.* **1996**, *14*, 136–141.

(7) Bonomi, M.; Branduardi, D.; Bussi, G.; Camilloni, C.; Provasi, D.; Raiteri, P.; Donadio, D.; Marinelli, F.; Pietrucci, F.; Broglia, R. a.; et al. PLUMED: A Portable Plugin for Free-Energy Calculations with Molecular Dynamics. *Comput. Phys. Commun.* **2009**, *180*, 1961–1972.

(8) Kirkwood, J. G. Statistical Mechanics of Fluid Mixtures. *J. Chem. Phys.* **1935**, *3*, 300.

(9) Torrie, G. M.; Valleau, J. P. Monte Carlo Free Energy Estimates Using Non-Boltzmann Sampling: Application to the Sub-Critical Lennard-Jones Fluid. *Chem. Phys. Lett.* **1974**, *28*, 578–581.

(10) Kumar, S.; Bouzida, D.; Swedsen, R. H.; Kollman, P. A.; Rosenbergl, J. M. The Weighted Histogram Analysis Method for Free-Energy Calculations on Biomolecules. I. The Method. *J. Comput. Chem.* **1992**, *13*, 1011–1021.

(11) Fenter, P.; Zhang, Z.; Park, C.; Sturchio, N. C.; Hu, X. M.; Higgins, S. R. Structure and Reactivity of the Dolomite (104)-Water Interface: New Insights into the Dolomite Problem. *Geochim. Cosmochim. Acta* **2007**, *71*, 566–579.

(12) Fenter, P.; Lee, S. S. Hydration Layer Structure at Solid – Water Interfaces. *MRS Bull.* **2014**, *39*, 1056–1061.

(13) Fenter, P.; Sturchio, N. C. Calcite (104)-Water Interface Structure, Revisited. *Geochim. Cosmochim. Acta* **2012**, *97*, 58–69.

(14) Kerisit, S.; Parker, S. C.; Harding, J. H. Atomistic Simulation of the Dissociative Adsorption of Water on Calcite Surfaces. *J. Phys. Chem. B* **2003**, *107*, 7676–7682.

(15) Cooke, D. J.; Gray, R. J.; Sand, K. K.; Stipp, S. L. S.; Elliott, J. a. Interaction of Ethanol and Water with the {1014} Surface of Calcite. *Langmuir* **2010**, *26*, 14520–14529.

(16) Raiteri, P.; Gale, J. D.; Quigley, D.; Rodger, P. M. Derivation of an Accurate Force-Field for Simulating the Growth of Calcium Carbonate from Aqueous Solution: A New Model for the Calcite?water Interface. *J. Phys. Chem. C* **2010**, *114*, 5997–6010.

(17) Kerisit, S.; Parker, S. C. Free Energy of Adsorption of Water and Metal Ions on the [10 1 4] Calcite Surface. *J. Am. Chem. Soc.* **2004**, 10152–10161.

(18) Yang, Y.; Sahai, N.; Romanek, C. S.; Chakraborty, S. A Computational Study of Mg2+ Dehydration in Aqueous Solution in the Presence of HS− and Other Monovalent Anions – Insights to Dolomite Formation. *Geochim. Cosmochim. Acta* **2012**, *88*, 77–87.

(19) Foster, J. F. Physical Properties of Amylose and Amylopectin in Solution. *Starch Chem. Technol.* **1965**, *1*, 349–392.

(20) Wingender, J.; Neu, T. R.; Flemming, H. C. What Are Bacterial Extracellular Polymeric Substances? In *Microbial Extracellular Polymeric Substances*; Springer Berlin Heidelberg, 1999; pp. 1–19.

(21) Martell, A. E.; Smith, R. M. *Critical Stability Constants*; Springer, 1974; Vol. 1.

(22) Kenward, P. A.; Goldstein, R. H.; González, L. A.; Roberts, J. A. Precipitation of Low-Temperature Dolomite from an Anaerobic Microbial Consortium: The Role of Methanogenic Archaea. *Geobiology* **2009**, *7*, 556–565.

(23) Roberts, J. A.; Kenward, P. A.; Fowle, D. A.; Goldstein, R. H.; González, L. A.; Moore, D. S. Surface Chemistry Allows for Abiotic Precipitation of Dolomite at Low Temperature. *Proc. Natl. Acad. Sci. U. S. A.* **2013**, 6–11.

(24) Higgins, S. R.; Hu, X. Self-Limiting Growth on Dolomite: Experimental Observations with in Situ Atomic Force Microscopy. *Geochim. Cosmochim. Acta* **2005**, *69*, 2085–2094.

(25) Whelan, J. K.; Emeis, K.-C. Sedimentation and Preservation of Amino Compounds and Carbohydrates in Marine Sediments. In *Organic Matter: Productivity, Accumulation, and Preservation in Recent and Ancient Sediments*; Columbia University Press New York, NY, 1992; pp. 176–200.

(26) Sinninghe Damsté, J. S.; Kok, M. D.; Köster, J.; Schouten, S. Sulfurized Carbohydrates: An Important Sedimentary Sink for Organic Carbon? *Earth Planet. Sci. Lett.* **1998**, *164*, 7–13.

(27) Carmichael, S. K.; Ferry, J. M. Formation of Replacement Dolomite in the Latemar Carbonate Buildup, Dolomites, Northern Italy: Part 2. Origin of the Dolomitizing Fluid and the Amount and Duration of Fluid Flow. *Am. J. Sci.* **2008**, *308*, 885–904.

Chapter appendix

1. Seven different tri-mannose configurations explored in our study and the energies of them. Water molecules are present in the simulations but are not drawn in the figures.

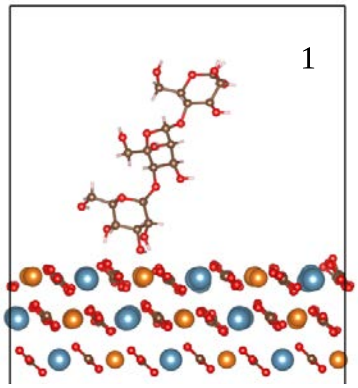

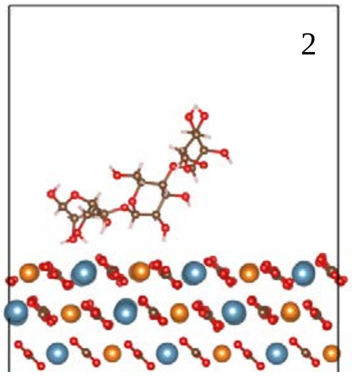

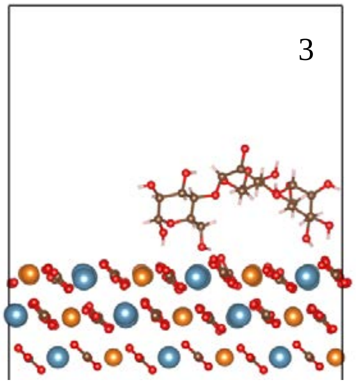

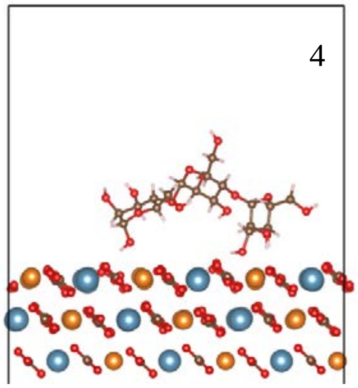

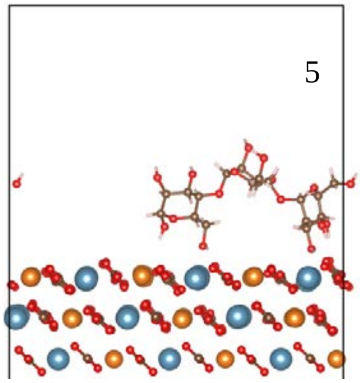

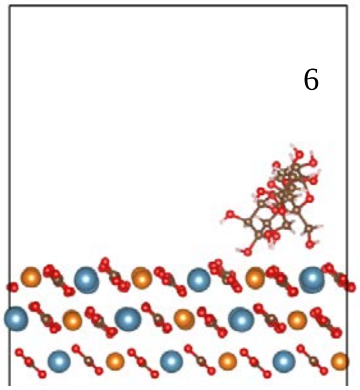

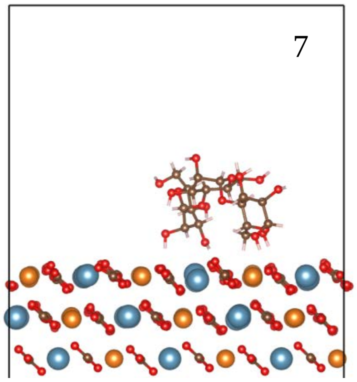

Configurations	Energy (eV) for 3756 atoms
1	-7651.95
2	-7648.44
3	-7648.72
4	-7648.77
5	-7649.95
6	-7650.67
7	-7650.97

2. Synthesis of dolomite using monosaccharides at room temperature

All synthesis experiments were carried out at room temperature in a desiccation cabinet (dimensions: 36×36×41cm^3) for 2 weeks. Petri dishes were used as reaction containers. Monosaccharide's concentration was varied from 0g/L to 4.0g/L. The initial concentration of $CaCl_2$ was fixed at 5mM, and Mg/Ca ratio was fixed at 3:1, 4:1, 5:1, 8:1, respectively. The formation of synthesized calcite seeds was verified by X-ray diffraction and optical microscope before these seeds were added to the solutions for dolomite growth experiments (calcite seeds concentration: 0.2g/L). For every 100mL of experimental solutions, 1g of ammonium bicarbonate powders were added in a separated petri dish in the desiccation cabinet. These ammonium bicarbonate powders decomposed into NH_3 and CO_2 within a week (the rate of decomposition is depending on the humidity) inside of the cabinet. The produced NH_3 will raise the pH, which will trigger the carbonate precipitation.

Figures:

The *y* axis of the following chart is the concentration of mannose used in the experiments. The *x* axis is the $MgCO_3$ content in the $(Ca,Mg)CO_3$. The black dots are from the experiments using a Mg:Ca ratio of 8:1. The red dots represents the experiments using a Mg:Ca ratio of 5:1.